Nonequilibrium Dynamics of DNA Unfolding

Von der Fakultät für Mathematik und Physik der Universität Stuttgart zur Erlangung der Würde eines Doktors der Naturwissenschaften (Dr. rer. nat.) genehmigte Abhandlung

Vorgelegt von

Eckhard Dieterich

aus Berlin-Zehlendorf

Hauptberichter:	Prof. Dr. Udo Seifert
Mitberichter:	Prof. Dr. Jörg Main

Tag der mündlichen Prüfung: 20. Juli 2015

II. Institut für Theoretische Physik der Universität Stuttgart

2015

Contents

List of Figures

Abbreviations and Symbols

Abbreviation	Definition
FDC	Force-Distance Curve
FDT	Fluctuation-Dissipation Theorem
NESS	Nonequilibrium Steady State

Symbol	Definition
a	uniform random number or fit parameter
α	scaled force amplitude or Eq. 5.11
B	strength of the thermal force
(B) B^{eq}	(non)equilibrium conjugate variable
$C^{(\prime)}$	(shifted) correlation function
$\chi^{(\mathrm{eq})}$	integrated (equilibrium) response
D	diffusion coefficient
δf	force perturbation
Δf	force amplitude
$\delta\lambda$	perturbation of the trap position
$\Delta\lambda$	amplitude of the trap position or trap adjustment
f	force
f_c, f_{di}	mean force, dichotomous force
$(\overline{f}_\infty)$ f_∞	(mean) limit force
$f_T^{(\pm)}$	(higher/lower) target force
F	total external force, Eq. 3.6
$(UF)F^{\pm}$	(un)folded state of the short hairpin at the force $f_c \pm \Delta f$, Fig. 4.3A and B
γ	friction coefficient
G, G_s, G_{DNA}	free energy of the hairpin, ssDNA, sequence
$G, G_0, G_\pm, G_{\max}$	feedback gains
h	perturbation
j	probability current

Symbol	Definition
k	stiffness of the trap
k_B	Boltzmann constant
k_{eff}	effective rigidity of the feedback
k_{nm}	rate for the transition from state n to state m
k_0	attempt frequency
L^0	time evolution operator
λ	control parameter, distance between the trap and the pipette
$\lambda^{(i)}$	eigenvalue of L^0
m	mass of the bead
μ	mobility of the bead
n	number of open base pairs
ω	frequency of the coupled oscillator
ω_{nm}	base pair (un)folding rate
ω^*	$\equiv \omega_{UF}^{+} = \omega_{F}^{-}$
$\omega_{(UF)F}^{\pm}$	hairpin (un)folding rate at the force $f_c \pm \Delta f$, Fig. 4.3A and B
$p(x,t), p_n$	probability distribution
$p^{s/\text{eq}}(x), p_n^{s/\text{eq}}$	$\hookrightarrow$ in the stationary state/in equilibrium
$R^{(\text{eq})}$	(equilibrium) response function
t	time
T	room temperature
T_{eff}	effective temperature
$\tilde{T}_{\text{eff}}$	oscillator temperature
τ_e	force switching time
τ_F	feedback operation time
$\tau^{(i)}$	system relaxation time, $\tau^{(i)} \equiv -1/\lambda^{(i)}$
τ_r	relaxation time of the mean force
τ_s	(largest) system relaxation time
V	potential
x	position of the bead or molecular extension
x_b	displacement of the bead from the center of the optical trap
x_h	molecular extension of the handle
x_{UF}	molecular extension of the unfolded hairpin
ξ, ζ	thermal force, noise

Kurzfassung

In dieser Doktorarbeit wurde die Entfaltung von DNA als Paradigma für die Betrachtung von zwei Themen in dem Feld der Nichtgleichgewichtsthermodynamik von kleinen Systemen benutzt. In dem ersten Projekt wurde eine Vielfalt von Systemen in einen stationären Nichtgleichgewichtszustand (NESS) getrieben, um zu untersuchen, ob diese Systeme mit einer effektiven Temperatur equilibrieren (siehe Kapitel 4). Dabei reichen die betrachteten Systeme von einem kolloidalen Teilchen in einer optischen Falle hin zu DNA-Hairpins mit zwei oder vielen Zuständen. Für alle Systeme sind sowohl experimentelle als auch theoretische Ergebnisse verfügbar. Das zweite Projekt betrachtet den Feedback-Mechanismus für die angewendete Kraft in dem DNA-Entfaltungssetup (siehe Kapitel 5). Mit Hilfe von experimentellen Daten und Simulationen wird hier die Feedback-kontrollierte Dynamik untersucht und damit die Feedback-Parameter, für die die Kontrolle der Kraft optimiert ist, bestimmt.

In **Kapitel 1** wird eine kurze Einführung in kleine Systeme im Allgemeinen und Experimente mit einzelnen Molekülen im Besonderen gegeben. Dabei wird die wichtige Rolle, die die Entfaltung von DNA in den letzten Jahren für die Entwicklung der Nichtgleichgewichtsthermodynamik von kleinen Systemen eingenommen hat, hervorgehoben. Anschließend wird das Konzept eingeführt, eine effektive Temperatur über das Fluktuations-Dissipations-Theorem für in das Nichtgleichgewichtsregime getriebene Systeme zu identifizieren. Es wird dann der in dieser Arbeit betrachtete stochastisch getriebene NESS beschrieben und am Beispiel des kolloidalen Teilchens in der optischen Falle illustriert. In der Folge wird ein kurzer Überblick über die experimentellen Systeme, für die die effektive Temperatur identifiziert wurde, und ihre zugehörigen theoretischen Modelle gegeben. Im Anschluss wird das Projekt zum Kraft-Feedback in der DNA-Entfaltung eingeführt, indem zunächst auf aktuelle Fortschritte in dem zugehörigen Forschungsgebiet verwiesen und dann das Feedback für die lange Hairpin beispielhaft dargestellt wird. Die Einleitung wird durch eine Skizze der experimentellen und theoretischen Grundlagen, die in den Kapiteln 2 und 3 gegeben werden, abgeschlossen.

Das **Kapitel 2** beschreibt das experimentelle DNA-Entfaltungssetup. In diesem Setup wird ein kolloidales Teilchen, das an einer DNA-Hairpin befestigt ist, mit einer optischen Falle eingefangen. Das anschließende Bewegen der Falle entfaltet die DNA. Die beiden experimentell zugänglichen Größen sind die Position der optischen Falle und die Kraft, die auf das gefangene Teilchen wirkt. Damit kann während des Entfaltungsprozesses eine Kraft-Abstandskurve (FDC) aufgenommen werden. Diese FDC spiegelt die Freie-Energie-Landschaft der Entfaltung der Hairpin wider: Je mehr ein Zustand der Hairpin energetisch bevorzugt ist, desto größer ist die Kraft, die benötigt wird, um den nächsten, weiter entfalteten Zustand zu erreichen. Die konkrete Form der FDC wird für die kurze und für die lange Hairpin diskutiert. Im Anschluss wird skizziert, wie mit Hilfe von elastischen Modellen für die verschiedenen Teile des Setups die Freie-Energie-Landschaft der Hairpin aus der FDC gewonnen werden kann. Diese Prozedur wird mit dem Beispiel der langen Hairpin illustriert.

Kapitel 3 behandelt die stochastische Dynamik, die zur Beschreibung sowohl der Bewegung des kolloidalen Teilchens als auch der Entfaltung von DNA verwendet wird. Insbesondere werden die Langevin- und die Fokker-Planck-Gleichung als Beschreibungen der stochastischen Dynamik von Systemen mit kontinuierlichen Freiheitsgraden eingeführt. Der letzte Teil dieses Kapitels widmet sich der Master-Gleichung, die die stochastische Dynamik von diskreten Systemen wie den DNA-Hairpins bestimmt.

Kapitel 4 präsentiert die Identifizierung der effektiven Temperatur für einzelne Moleküle, die stochastisch in einen NESS getrieben wurden. Dieses Kapitel beginnt mit dem FDT, welches aussagt, dass im Gleichgewicht die Antwortfunktion χ eines Systems auf eine externe Störung gleich der Korrelationsfunktion C geteilt durch die Badtemperatur T (und die Boltzmann-Konstante k_B) ist. Einem früheren, für glasartige Systeme vorgebrachten Vorschlag folgend wird dann das FDT in das Nichtgleichgewichtsregime erweitert, indem T durch die effektive Temperatur T_{eff} ersetzt wird. Des Weiteren wird das externe Protokoll, mit dem der NESS erzeugt wird, definiert. Mit diesem Protokoll wird die Kraft zufällig auf einer Zeitskala τ_e zwischen zwei Werten, die durch das Zweifache der Kraftamplitude Δf getrennt sind, hin- und hergeschaltet.

Als erstes von drei Systemen wird dann das Auftreten der effektiven Temperatur für ein kolloidales Teilchen in einer optischen Falle untersucht. Für dieses System wird beobachtet, dass die experimentelle Antwortfunktion χ exponentiell auf einer einzelnen Zeitskala τ_s relaxiert, die durch die Mobilität des Teilchens und die Rigidität der Falle bestimmt ist. Falls die Kraftänderungszeit τ_e des externen Treibens kleiner als diese Systemrelaxationszeit τ_s ist, zeigen die

Experimente, dass die effektive Temperatur für lange Zeiten identifiziert werden kann. Diese experimentellen Ergebnisse stimmen mit theoretischen Vorhersagen überein, die aus der Modellierung des gefangenen Kolloids als einem einer überdämpften Langevin-Dynamik gehorchenden Teilchen in einer harmonischen Falle folgen. Das Modell legt darüber hinaus nahe, dass es eine Übergangszeit τ_c in das Langzeitregime gibt, in dem die effektive Temperatur beobachtet wird. Für Kraftänderungszeiten τ_e, die sehr viel kleiner als τ_s sind, ist τ_c sehr klein, so dass nur für sehr kurze Zeiten keine effektive Temperatur existiert. Dieses Resultat gibt wieder, dass sich die externen zufälligen Kräfte in diesem Limes $\tau_e \ll \tau_s$ wie ein zusätzliches thermisches Rauschen verhalten. Die Betrachtung des gefangenen Kolloids wird durch die Analyse des entgegengesetzten Limes von Kraftänderungszeiten τ_e, die sehr viel größer als τ_s sind, abgeschlossen. In diesem Limes gibt es keine effektive Temperatur bei großen Zeiten, allerdings ist das Gleichgewichts-FDT für kleine Zeiten wiederhergestellt. Dieses Resultat demonstriert, dass das Kolloid für jede angewendete Kraft equilibrieren kann, falls $\tau_e \gg \tau_s$.

Im Anschluss wird der stochastisch getriebene NESS einer kurzen DNA-Hairpin mit zwei Zuständen betrachtet. Die Experimente mit zwei verschiedenen kurzen Hairpins zeigen, dass die Antwortfunktion χ eine einzelne Relaxationszeit τ_s hat, so wie es auch für das gefangene kolloidale Teilchen beobachtet wurde. Des Weiteren kann eine effektive Temperatur für die kurzen Hairpins für große Zeiten identifiziert werden, falls die externe Kraftänderungszeit τ_e kleiner als τ_s ist. Diese Resultate werden bestätigt, wenn die zufällig getriebene kurze Hairpin als Markovsches Vier-Zustands-System modelliert wird. Zusätzlich hebt das theoretische Modell hervor, dass für die kurze Hairpin erstens die Relaxationszeit τ_s das Inverse der Entfaltungsrate bei der größeren der beiden angewendeten Kräfte ist und zweitens der Wert der effektiven Temperatur, die man für $\tau_e < \tau_s$ identifiziert, unabhängig von der Wahl der Observablen ist. Das Modell sagt darüber hinaus aus, dass sowohl die Existenz als auch der Wert der effektiven Temperatur durch das Verhältnis τ_e/τ_s bestimmt sind. Insbesondere sagt das Modell in Übereinstimmung mit der naiven Erwartung vorher, dass die effektive Temperatur kleiner für schwächeres Treiben, also kleineres τ_e/τ_s, wird. Für beide der vorgenannten Vorhersagen wird gezeigt, dass sie durch eine Serie von Messungen mit einem dritten Hairpin-Typ experimentell bestätigt sind.

Das letzte, komplexeste System ist eine lange DNA-Hairpin mit sehr vielen teilweise entfalteten Zwischenzuständen. Die größere Anzahl an Zuständen ist mit einer gewachsenen Anzahl an Systemrelaxationszeiten verbunden, die, falls sie nicht gut separiert sind, komplexe Formen der Antwortfunktion χ und der Korrelationsfunktion C verursachen können, die nicht durch einen einzelnen

zeitunabhängigen Faktor wie die effektive Temperatur verbunden sind. Die Experimente zeigen jedoch, dass die Antwortfunktion χ der langen Hairpin eine gut separierte Zeitskala τ_s hat, was die Identifikation einer effektiven Temperatur erlaubt, falls die Kraftänderungszeit τ_e kleiner als τ_s ist. Obwohl dieses Resultat einen Spezialfall repräsentiert, kann dennoch erwartet werden, dass es typisch für Systeme ist, die wie die lange Hairpin große, nicht degenerierte Barrieren besitzen, da in solchen Systemen die mit der Überwindung der größten Barriere verbundene Zeitskala exponentiell größer ist. Das experimentelle Ergebnis, dass es eine effektive Temperatur für die lange Hairpin gibt, falls $\tau_e < \tau_s$, wird durch Simulationen bestätigt, die ein detailliertes Modell der langen Hairpin verwenden, welches sowohl ihre elastischen Eigenschaften als auch ihre Basenpaarsequenz berücksichtigt. Als Abschluss dieses Kapitels folgen eine Zusammenfassung der zentralen Resultate, ein Ausblick auf zukünftige Arbeit und eine Diskussion eines früheren Vorschlags, die effektive Temperatur durch einen an das stochastisch getriebene System gekoppelten Oszillator zu messen.

In **Kapitel 5** wird der Feedback-Mechanismus für die Kraft in dem DNA-Entfaltungssetup diskutiert. Das Kapitel zeigt zunächst, dass das Feedback durch seine Betriebszeit τ_F und seinen Stellfaktor G bestimmt ist. Dieser Stellfaktor legt die Reaktion des Feedbacks auf ein gegebenes Messergebnis der Kraft fest. Der Feedback-Mechanismus wird anschließend am Beispiel der stochastisch getriebenen langen Hairpin illustriert, um zu zeigen, wie die Feedback-kontrollierte Kraft dem externen Protokoll folgt. Dieses Beispiel führt darüber hinaus eine Erweiterung der basenpaarweisen Simulation der Dynamik der langen Hairpin ein, die den Feedback-Mechanismus explizit einbezieht.

Als Toy-Model für das Kraft-Feedback in der DNA-Entfaltung wird im Anschluss ein Feedback-kontrolliertes Teilchen in einem harmonischen Oszillator betrachtet. Für dieses System wird die Trajektorie der mittleren Kraft nach einem Wechsel der Zielkraft als Größe eingeführt, die Zugang zu der Reaktion des Feedbacks auf Änderungen des externen Protokolls bietet. Diese Größe zeigt, dass es einen optimalen Wert G_0 des Stellfaktors gibt, für den die Kraft am schnellsten auf einen neuen Wert eingestellt wird. Darüber hinaus wird beobachtet, dass das Erhöhen des Stellfaktors über einen Schwellwert $G_{\max} > G_0$ die Reaktion des Feedbacks so sehr verstärkt, dass die mittlere Kraft mit fortlaufender Zeit anwachsende Oszillationen zeigt, die das System destabilisieren. Zuletzt legt die Trajektorie der mittleren Kraft in Übereinstimmung mit der naiven Erwartung nahe, dass sich die Feedback-Kontrolle für kleinere Betriebszeiten τ_F verbessert.

Für die lange DNA-Hairpin wird beobachtet, dass die Trajektorie der mittleren Kraft sowohl im Experiment als auch in der Theorie eine bedeutend

komplexere Form annimmt, die die verschiedenen in den Entfaltungsprozess involvierten Zeitskalen widerspiegelt. Im Regime kurzer Zeiten verhält sich die mittlere Kraft jedoch wie im Fall des harmonischen Oszillators: Die Kraft wird am schnellsten neu eingestellt, falls das Feedback einen optimalen Stellfaktor G_0 benutzt; sie wächst allerdings für Stellfaktoren, die über einer Schwelle $G_{\max} > G_0$ liegen, in der Zeit an. Darüber hinaus belegt die Trajektorie der mittleren Kraft, dass die Feedback-Kontrolle für kleinere Betriebszeiten τ_F verbessert ist. Die Diskussion des Kraft-Feedbacks in der DNA-Entfaltung wird im Anschluss erweitert, indem zusätzlich das Krafthistogramm in einem gegebenen Zustand der Hairpin betrachtet wird. Diese Größe demonstriert sowohl im Experiment als auch in der Theorie, dass das Feedback das System aus dem Gleichgewicht heraus treibt, während es versucht das durch das externe Protokoll diktierte stochastische Treiben zu realisieren. Insbesondere wird das System für größere Stellfaktoren G und kleinere Betriebszeiten τ_F stärker in das Nichtgleichgewichtsregime verschoben. Das Krafthistogramm zeigt auch, dass es einen optimalen Wert von G gibt, für den die Übereinstimmung der Kraft mit ihrem Zielwert maximiert ist. Dieser optimale Wert liegt nahe an der entsprechenden Abschätzung, die durch die Trajektorie der mittleren Kraft verfügbar ist.

Abstract

In this thesis, the unfolding of DNA is used as a paradigm to address two topics in the field of the nonequilibrium thermodynamics of small systems. In the first project, a variety of systems is driven into a nonequilibrium steady state (NESS) to investigate whether these systems equilibrate with an effective temperature (see Chapter 4). The systems considered range from a colloidal particle in an optical trap to two-state and multiple-state DNA hairpins. For all systems, both experimental and theoretical results are available. The second project focuses on the feedback mechanism for the applied force in the DNA unfolding setup (see Chapter 5). Both experimental data and simulations are used to study the feedback-controlled dynamics, thus determining the set of feedback parameters for which the control of the force is optimized.

In **Chapter 1**, a brief introduction is given to small systems in general and to single-molecule experiments in particular, highlighting the important role which the unfolding of DNA has played for the development of the nonequilibrium thermodynamics of small systems in recent years. The concept of identifying an effective temperature through the fluctuation-dissipation theorem (FDT) for systems driven into the nonequilibrium regime is then introduced. Subsequently, the stochastically driven NESS considered in this thesis is described and illustrated with the example of a colloidal particle in an optical trap. A brief overview over the experimental systems for which the effective temperature has been identified and their corresponding theoretical models then follows. Afterwards, the project on the force feedback in DNA unfolding is introduced by first recollecting several recent advances in the field and then exemplifying the feedback for the long hairpin. The introduction is concluded by a sketch of the experimental and theoretical foundations given in Chapter 2 and 3.

Chapter 2 describes the experimental DNA unfolding setup. This setup uses an optical trap to capture a colloidal particle attached to the DNA hairpin. Moving the trap subsequently unzips the DNA. The two experimentally accessible quantities are the position of the optical trap and the force acting on the trapped particle, allowing for the collection of a force-distance curve

(FDC) during the unfolding process. This FDC reflects the unfolding free energy profile of the hairpin. Indeed, the more energetically favored a state of the hairpin is, the larger the force needed to reach the next, more unfolded state. The specific shape of the FDC is discussed for both the short and the long hairpin. Afterwards, an outline is given of how by setting up elastic models for each part of the setup, the FDC can be used to calculate the free energy profile of the hairpin, a procedure which is briefly exemplified for the long hairpin.

In **Chapter 3**, the stochastic dynamics framework used to model both the motion of the colloidal particle and the unfolding of DNA is described. Specifically, the Langevin and the Fokker-Planck equation are introduced as descriptions of the stochastic dynamics of systems with continuous degrees of freedom. The final part of this chapter is dedicated to discussing the master equation which governs the stochastic dynamics of discrete systems such as the DNA hairpins.

Chapter 4 presents the single-molecule identification of the effective temperature for systems stochastically driven into a NESS. The chapter begins with the FDT which states that in equilibrium, the response χ of a system to an external perturbation is equal to the correlation function C divided by the bath temperature T (and the Boltzmann constant k_B). Following an earlier proposal brought forward for glassy systems, the FDT is then extended to the nonequilibrium regime by replacing T by the effective temperature T_{eff}. Furthermore, the external force protocol used to generate the NESS is defined. With this protocol, the force is randomly switched on the time scale τ_e between two values separated by twice the force amplitude Δf.

As the first of three systems, the emergence of the effective temperature is then investigated for a colloidal particle in an optical trap. For this system, the experimental response χ is observed to relax exponentially on a single time scale τ_s determined by the mobility of the particle and the stiffness of the trap. If the force switching time τ_e of the external driving is smaller than this system relaxation time τ_s, the experiments show that the effective temperature can be identified for large times. These experimental results are confirmed by theoretical predictions which are obtained by modeling the optically trapped colloid as a particle in a harmonic oscillator obeying an overdamped Langevin equation. The model moreover suggests that there is a crossover time τ_c into the large-time regime where the effective temperature is observed. For force switching times τ_e much smaller than τ_s, τ_c is very small so that there is an effective temperature for all but very short times. This result reflects that in this limit $\tau_e \ll \tau_s$, the external random forces behave as additional thermal

noise. The discussion of the trapped colloid is concluded by considering in both theory and experiment the opposite limit of force switching times τ_e much larger than τ_s. In this limit, there is no effective temperature at large times but the original equilibrium FDT is restored for small times. This result demonstrates that the colloid can equilibrate for each applied force if $\tau_e \gg \tau_s$.

Subsequently, the stochastically driven NESS of a short DNA hairpin which unfolds in a two-state manner is considered. The experiments with two different short hairpins show that the response χ has a single relaxation time τ_s, as in the case of the trapped colloid. Furthermore, an effective temperature can be identified for the short hairpins for large times if the external force switching time τ_e is smaller than τ_s. These results are reproduced when modeling the randomly driven short hairpin as a four-state Markov system. Additionally, the theoretical model highlights that for the short hairpin, i) the relaxation time τ_s is the inverse of the unfolding rate at the larger of the two applied forces and ii) the value of the effective temperature one identifies for $\tau_e < \tau_s$ is independent of the choice of the observable. The model furthermore states that both the existence and the value of the effective temperature are determined by the ratio τ_e/τ_s. Specifically, the model predicts that the effective temperature gets smaller for weaker forcing, i.e., for smaller τ_e/τ_s, in agreement with the naive expectation. Both these predictions are shown to be confirmed experimentally by a series of measurements with a third hairpin type.

The final, most complex system is a long DNA hairpin which has numerous partially unfolded intermediate states. The larger number of states comes with an increased number of system relaxation times which, if not well-separated, can cause the response χ and the correlation function C to take different complex forms not related by a single time-independent factor such as the effective temperature. However, the experiments show that the response χ of the long hairpin does have a well-separated time scale τ_s, allowing for the identification of an effective temperature if the force switching time τ_e is smaller than τ_s. Although representing a special case, this result can nevertheless be expected to be typical for a system with large non-degenerate barriers such as the long hairpin where the time scale connected to surpassing the biggest barrier is exponentially larger. The experimental result that there is an effective temperature for the long hairpin if $\tau_e < \tau_s$ is reproduced by simulations using a detailed model of the long hairpin which includes both its elastic properties and its base-pair sequence. The chapter is concluded by a summary of the main results, a brief outlook on future work and a discussion of an earlier suggestion to measure the effective temperature by coupling a harmonic oscillator to the stochastically driven system.

In **Chapter 5**, the feedback mechanism for the force in the DNA unfolding setup is discussed. The chapter begins by showing that the feedback is determined by its operation time scale τ_F and by its gain G. This gain dictates the feedback reaction to a given measurement of the force. The feedback mechanism is afterwards exemplified for the stochastically driven long hairpin to illustrate how the feedback-controlled force follows the external protocol. This example moreover introduces an extension of the base-pairwise simulation of the long hairpin dynamics which explicitly incorporates the feedback mechanism.

As a toy model for the force feedback in DNA unfolding, a feedback-controlled particle in a harmonic oscillator is then considered. For this system, the mean force trajectory after a change of the target force is introduced. This quantity provides access to the feedback reaction to changes of the external protocol. The mean force trajectory shows that there is an optimal value G_0 of the feedback gain for which the force is most quickly adjusted to a new value. Moreover, increasing the feedback gain above some threshold $G_{\max} > G_0$ is observed to strengthen the feedback reaction to the point that the mean force shows oscillations which grow over time, thus destabilizing the system. Finally, the mean force trajectory suggests that the feedback control improves if its operation time τ_F is smaller, as is naively expected.

For the long DNA hairpin, the mean force trajectory is observed in both theory and experiment to take a noticeably more complex form, reflecting the various time scales involved in the unfolding process. However, in the short-time regime, the mean force behaves as in case of the harmonic oscillator: The force is most quickly adjusted if the feedback uses an optimal gain G_0 but grows over time for gains larger than some threshold $G_{\max} > G_0$. Furthermore, the mean force trajectory states that the feedback control is enhanced for smaller operation times τ_F. The discussion of the force feedback in DNA unfolding is then extended by additionally considering the force population in a given state of the hairpin. In both theory and experiment, this quantity demonstrates that the feedback drives the system away from equilibrium while trying to realize the stochastic driving dictated by the external protocol. In particular, the feedback pushes the system more into the nonequilibrium regime for larger gains G and smaller operation times τ_F. The force population also shows that there is an optimal value of G for which the agreement of the force with its target value is maximized. This optimal value is close to the corresponding estimate provided by the mean force trajectory.

1. Introduction

The mechanical unfolding of DNA is a paradigm among the class of nonequilibrium processes of small systems. These systems are small in the sense that the fluctuations they show as a result of thermal excitations are relevant. This description applies to many molecular biological systems. The better understanding of small systems can thus provide important insights in the physics of life at the molecular level. Over the past two decades, there has been significant advance in this field (see [1–5] for reviews), both due to theoretical progress and because of the development of new experimental techniques which, in particular, allow one to follow the dynamics of single molecules for the first time. Among the first to perform one of these so-called single molecule experiments were Bustamante *et al.* who measured the elastic response of single DNA molecules by applying forces in the piconewton range [6, 7]. Further early examples of single molecule experiments used optical tweezers [8, 9] and atomic force microscopy [10, 11] to investigate the unfolding process of single titin and RNA/DNA molecules.

The experimental progress in the manipulation of small systems was accompanied by a breakthrough in the theoretical description of these systems when Jarzynski derived a theorem relating nonequilibrium work fluctuations to an equilibrium free energy difference [12]. This Jarzynski relation is one of many so-called fluctuation theorems [13–15] which give information about the distributions of fluctuating thermodynamic quantities and which can be derived from a single master fluctuation theorem [16]. The first experimental tests of fluctuations theorems were performed by unfolding RNA with a setup similar to the one used in this thesis [17–20]. In these experiments, the fluctuations of the work needed to irreversibly unfold RNA are connected to the equilibrium free energy difference between the folded and unfolded state of the molecule.

The unfolding of DNA (or RNA) has thus indeed served as a paradigm in the field of the nonequilibrium thermodynamics of small systems in recent years. In this thesis, the paradigmatic role of the DNA unfolding system has been exploited by using it to investigate whether small systems driven into the nonequilibrium regime can equilibrate with an effective temperature. Following an earlier suggestion raised in the context of glassy systems [21, 22], this effective temperature is identified via the fluctuation-dissipation theorem (FDT).

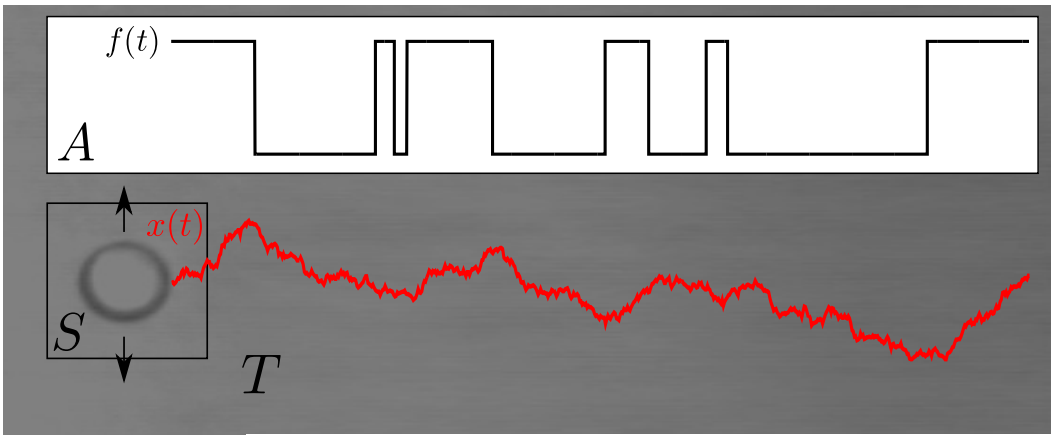

FIGURE 1.1.: Scheme of the stochastic driving. An external agent A drives a system S embedded in a heat bath with temperature T into a NESS by applying a random force $f(t)$. As an example for such a system, the experimental video image of a colloidal particle in an optical trap immersed in aqueous solution is shown (the image is from an experiment performed by the research group of Felix Ritort at the Universitat de Barcelona). In this case, the external agent is the mini-tweezers apparatus driving the particle with position $x(t)$ by changing the position of the optical trap. Chapter 4 demonstrates that under some conditions, the stochastic driving effectively increases the temperature of the system. Chapter 5 discusses the feedback mechanism needed to apply this stochastic driving to single DNA hairpins. Figure reprinted from [23].

In equilibrium, the FDT states that the response of the system to an external perturbation is proportional to a correlation function, the proportionality factor being the inverse of the bath temperature (aside from the Boltzmann constant k_B). The physical observation behind this theorem is that in equilibrium, the system reacts to an external perturbation as it would react to a spontaneous thermal excitation. This thesis examines whether the FDT can be restored for small systems outside of equilibrium if the bath temperature is replaced by a so-called effective temperature.

The emergence of an effective temperature has been tested for the specific class of small systems driven into a nonequilibrium steady state (NESS) by random external forces. As illustration, Fig. 1.1 exemplifies this stochastic external driving for a small colloidal particle which is trapped in a harmonic potential and immersed in an aqueous environment: The particle is driven into

a NESS by applying a force randomly changing over time between two values. As a result, the particle fluctuates more strongly, as if, loosely speaking, the temperature of the bath had been increased to some effective temperature. The external random forcing is thus intended to mimic an additional thermal noise raising the temperature of the system. However, since the external forces have a finite correlation time, they are not exactly thermal. Therefore, one can expect that there are conditions which must be met to observe an effective temperature.

In **Chapter 4**, these conditions are determined by testing whether the FDT is restored with an effective temperature in the stochastically driven NESS. The stochastic driving is applied to three different small systems of growing complexity. First, the colloidal particle in the harmonic trap as shown in Fig. 1.1 is considered. Subsequently, a short and a long DNA hairpin is studied. While the short DNA molecule unfolds in a two-state manner when subject to an external force, the long one has numerous partially unfolded intermediate states (see Fig. 1.2A). The long hairpin thus exhibits a significantly more complex stationary dynamics.

For all three systems considered, the response and the correlation function in the FDT have been both measured experimentally and calculated (or simulated) theoretically. The theoretical predictions have been obtained by setting up a dedicated model for each experimental system. In particular, the colloidal particle in the optical trap has been modeled as an overdamped particle in a harmonic oscillator whose dynamics is governed by a Langevin equation. Furthermore, the stochastically driven short hairpin has been described as a four-state system with a Markov dynamics. Finally, a detailed Markov model of the base-pairwise dynamics of the long hairpin taking into account both its elastic properties and its base pair sequence has been set up. These theoretical models not only provide a test of the experimental data. They also produce a variety of analytical results illustrating the behavior of the system in general and the conditions for the emergence of the effective temperature in particular. This chapter is concluded by a summary of the main results and a short outlook on future work.

The external protocol used to generate the NESS with the effective temperature requires control of the applied force. In the DNA unfolding setup, the force is controlled by a feedback mechanism. Feedback in nonequilibrium systems has attracted significant interest in recent years. In particular, systems with feedback have been shown to obey generalized fluctuation theorems [24–26] which allow one to extract work from a single heat bath [27, 28]. However, it comes at the cost of storing information that later on needs to be erased [29–31]. These results demonstrate the importance of feedback mechanisms such as the

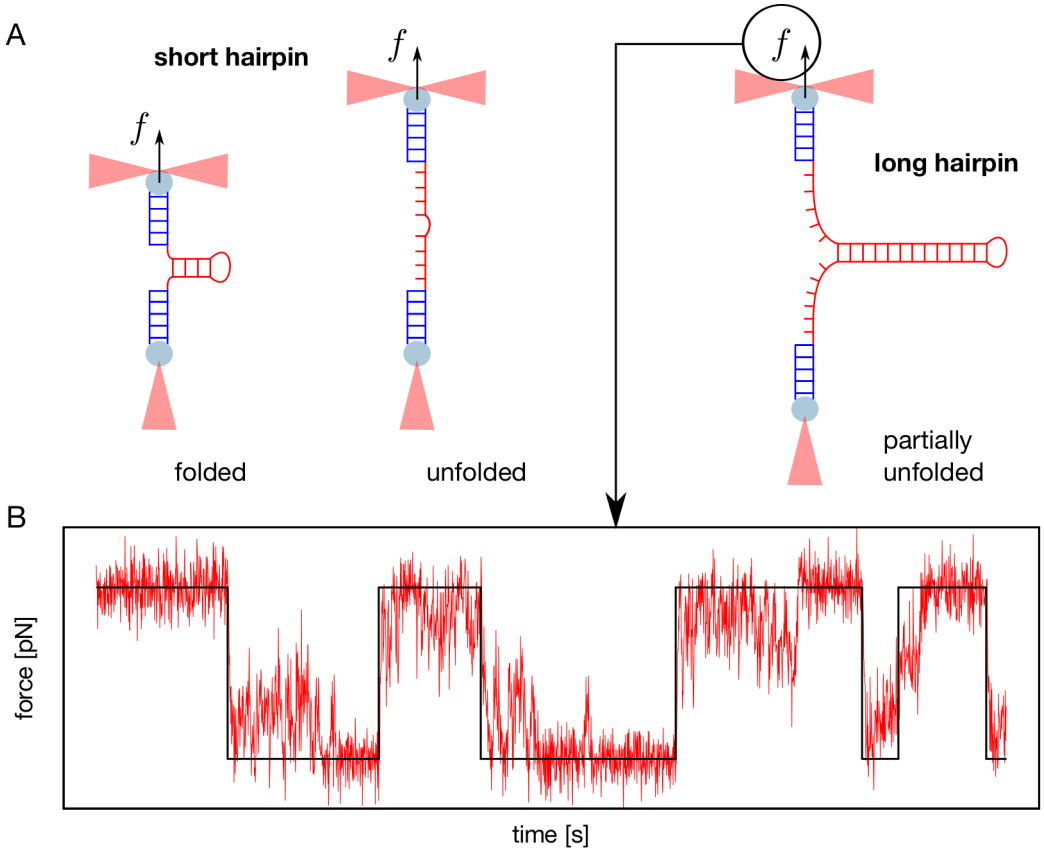

FIGURE 1.2.: DNA hairpins and force feedback. - (**A**) Single DNA hairpins are unfolded by applying an external force f. The short hairpin jumps to the unfolded state directly, while the long hairpin passes through numerous partially unfolded intermediate states. Details of the experimental unfolding setup introduced here are given in Chapter 2. - (**B**) The applied force is experimentally controlled by a feedback mechanism. This feedback attempts to adjust the measured force (red) to the random switching dictated by the external protocol (black).

force feedback in DNA unfolding considered here.

In **Chapter 5**, a detailed discussion of this force feedback is given. As a first illustration, Fig. 1.2B shows how the experimental force matches the external protocol for the randomly driven long hairpin. One can observe that the experimental feedback control is good enough to let the force follow the external protocol closely but that the force nevertheless shows noticeable fluctuations. The size of these fluctuations and the general quality of the control

of the force depends on how the feedback is set up, i.e., on which feedback parameters are chosen. For the force feedback used, these parameters are the time the feedback needs to measure the force and then respond to this input and the so-called feedback gain which determines this response. In this thesis, an extensive discussion of the feedback-controlled dynamics as a function of these feedback parameters is presented. This discussion is started by considering, as a toy model for the DNA unfolding system, an analytically solvable model for a force feedback in an harmonic oscillator.

In the introductory **Chapters 2 and 3**, a brief account of the experimental and theoretical foundations of this thesis is given. Specifically, Chapter 2 describes the DNA unfolding setup and introduces the force-distance curve (FDC) as the natural result of an unfolding experiment. The FDC reflects the consecutive unzipping of the DNA hairpin and can be used to infer the free energies of the DNA base pairs. With these free energies, one can construct unfolding free energy profiles, as is demonstrated for the long hairpin in Chapter 2.

With the free energy profile then introduced, the following Chapter 3 is dedicated to defining the dynamics of the hairpin within this profile. While the unfolding of DNA is a discrete process involving the breaking and closing of single base pairs, the dynamics of a system with a continuous degree of freedom is nevertheless discussed first. This discussion allows one to derive a model for the optically trapped colloidal particle which is considered in Chapter 4. The dynamics of this particle and of the DNA hairpin is stochastic since both systems are embedded into an aqueous solution where water molecules permanently exert random kicks. Chapter 3 demonstrates that the stochastic dynamics of a system can be described on different, yet equivalent levels. For systems with a continuous degree of freedom, the Langevin equation is shown to govern the dynamics of a single realization of the stochastic process while the Fokker-Planck equation is observed to dictate the time evolution of the full statistical ensemble. The master equation is then introduced as the analogue of the Fokker-Planck equation for discrete systems such as the DNA unfolding setup. This chapter is concluded by briefly outlining a numerical solution of the master equation which is needed to simulate the dynamics of the long hairpin in the main Chapters 4 and 5.

2. Unfolding DNA

2.1. DNA Unfolding Setup

The DNA unfolding experiments presented and discussed in this thesis were performed by Joan Camunas-Soler and Marco Ribezzi-Crivellari from the group of Felix Ritort at the Universitat de Barcelona, using an optical tweezers instrument originally designed by Smith *et al.* [32–35]. In this setup, a small transparent sphere (the *bead*) is attached to each strand of a DNA hairpin immersed in aqueous solution via a 29 base pairs fragment of double-stranded DNA (the *handle* [36]). While one of these beads is kept immobilized by a pipette, the other one is captured by a harmonic optical trap whose position is controlled and monitored with a resolution of 1 nm and at a rate of 1 kHz (see Fig. 2.1A)[1]. At the same rate and with a precision of 0.1 pN, the optical tweezers additionally collects the force acting upon the trapped bead [32, 39]. The tweezers instrument therefore allows one to unfold the DNA hairpin by moving the optical trap away from the pipette while simultaneously measuring the force the hairpin exerts on the captured bead.

The unfolding process breaks the base pairs of the hairpin and thus releases single stranded DNA (ssDNA). Referring to the extension of the released ssDNA by x, the distance λ of the center of the optical trap to the tip of the pipette therefore takes the form

$$\lambda = x_b + 2x_h + x, \tag{2.1}$$

where x_b is the displacement of the bead from the center of the optical trap and x_h the molecular extension of the handle (see Fig. 2.1A). Modeling the optical trap as a harmonic oscillator with stiffness k, the displacement of the bead is given by

$$x_b(f) = \frac{f}{k} \tag{2.2}$$

[1] In a related setup, both beads are trapped optically [37]. This alternative *dual-trap* setup has been used to perform partial work measurements from which free energies can be inferred via fluctuation theorems [38].

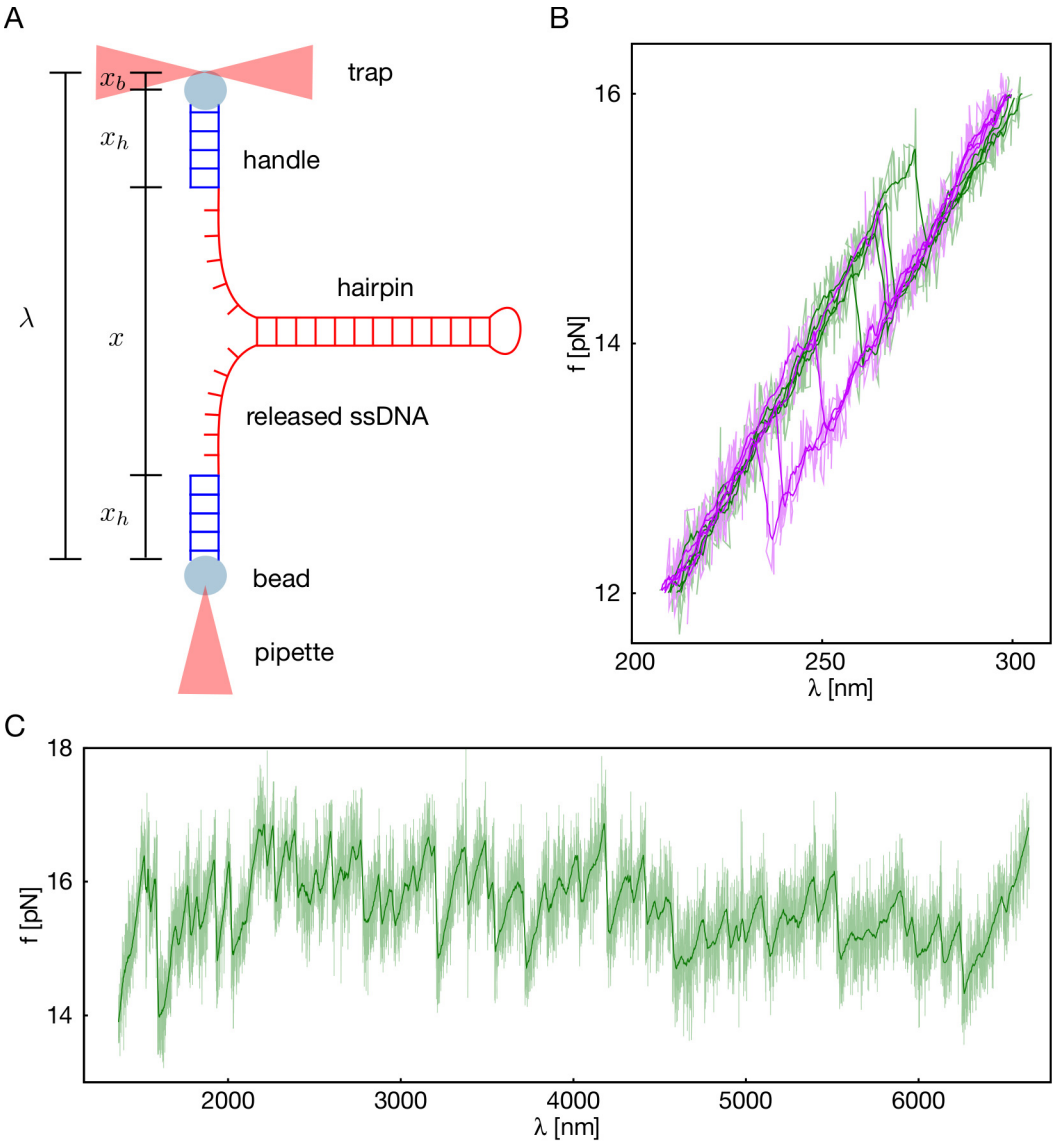

FIGURE 2.1.: DNA unfolding setup. - (**A**) Moving the trap up and down, i.e., changing the distance λ of the center of the trap to the pipette, unfolds and refolds the DNA hairpin. The distance λ gets contributions from all parts of the setup through $\lambda = x_b + 2x_h + x$, where x_b is the displacement of the bead from the center of optical trap and where $2x_h$ and x are the molecular extensions of the handles and the released ssDNA, respectively. - (**B**) In violet (green), FDC of a short 20 base pairs hairpin (un)folding in a two-state manner. - (**C**) Unfolding FDC of a long 6838 base pairs hairpin with multiple intermediate states. Figure in part reprinted from [23].

if the force f is applied. Furthermore, one can model the handles as a worm-like chain with the elastic response [40]

$$f(x_h) = \frac{k_B T}{4 l_p} \left(\left(1 - \frac{x_h}{L_0} \right)^{-2} - 1 + 4 \frac{x_h}{L_0} \right), \tag{2.3}$$

with the temperature T, the Boltzmann constant k_B, the persistence length $l_p = 50\,\mathrm{nm}$ and the contour length $L_0 = 9.86\,\mathrm{nm}$ of the handle. Finally, the released ssDNA can be described by the freely-jointed chain model for which [7, 41]

$$x(f, n) = d_s n \left(\coth\left(\frac{bf}{k_B T} \right) - \frac{k_B T}{bf} \right), \tag{2.4}$$

where $d_s = 0.59\,\mathrm{nm}$ is the distance between consecutive base pairs in the hairpin if no force is applied, n the number of open base pairs and $b = 1.15\,\mathrm{nm}$ the Kuhn length. With these elastic models, a number n of open base pairs can be related to each experimental data point (λ, f), allowing one to directly follow the breaking and closing of DNA base pairs along the experimental trajectory.

The discussion of the DNA unfolding setup is concluded by pointing out that this setup has found many applications in recent years, where examples are the verification of fluctuation theorems already referred to in the introduction [17, 19], a measurement of the free energies of kinetic states [42] and studies on how peptides bind to DNA [43, 44].

2.2. Force-Distance Curve and Free Energy Profile

The above discussed setup allows one to unfold the DNA hairpin by increasing the distance λ between the trap and the pipette linearly over time while monitoring the force f on the captured bead. This experiment generates a force-distance curve (FDC) that displays both the elastic properties of the setup and, in particular, the strength of the base pair interactions within the DNA hairpin. The FDC has a sawtooth pattern which is characteristic for the hairpin sequence which has been unfolded. For the example of a short hairpin that unzips in a two-state manner, the FDC shows a distinct drop of the force once the hairpin unfolds (see Fig. 2.1B), corresponding to a sudden release of the trapped bead from the tension applied by the hairpin. Before and after

the transition of the hairpin, increasing the distance just probes the elastic response of the setup, leading to a steady growth of the measured force. Since the unzipping of the hairpin releases single strands of DNA which decrease the stiffness of the setup, the elastic response is weaker in the unfolded state. This effect becomes more pronounced the longer the hairpin is.

A remarkable property of the DNA unfolding setup used here is that the unzipping leaves the hairpin unharmed: Reversing the protocol for the distance by decreasing λ linearly over time brings the hairpin back to its folded state (see Fig. 2.1B). The force at which the hairpin folds back depends on the pulling speed. If the trap is moved infinitely slowly (quasistatically) in both directions, the system is always in equilibrium and therefore, the average unfolding and folding force are the same. In contrast, the FDC shows hysteresis for nonvanishing pulling speeds (see Fig. 2.1B), equivalent to dissipation of heat into the medium and thus a signature of a nonequilibrium process. The larger the pulling speed, the more the system is driven into nonequilibrium and the more heat is dissipated. The unfolding of DNA (or RNA) hence represents a well controllable process which can be used to test nonequilibrium relations.

If one unfolds long hairpins with several intermediate states instead of the above short two-state hairpin, the FDC obtains a complex structure that reflects the successive unzipping of the hairpin (see Fig. 2.1C). Increasing the distance λ then does not unfold the whole hairpin at once but rather breaks several base pairs [45] until the next intermediate state is reached. In the FDC, this process corresponds to a drop of the force followed by the elastic response of the intermediate state. The more stable this state is, the more one has to increase the distance, i.e., raise the force, before unfolding into the next intermediate takes place. The shape of the FDC is thus a direct reflection of the free energy profile of the hairpin. If the hairpin sequence is known, the FDC can therefore be used to access the (nearest neighbor) free energies of single base pairs [46].

By adding these free energies along any given hairpin sequence, the free energy $G_{\mathrm{DNA}}(n)$ of this hairpin when n base pairs are open and no external force is applied can be calculated. Adding an external force then contributes the free energy

$$G_s(f,n) = -\int_0^f x(f',n)\,\mathrm{d}f' \tag{2.5}$$

representing the stretching of the ssDNA released in the unfolding process. The total free energy $G(f,n)$ of a DNA hairpin with n open base pairs and subject to the external force f thus follows as

$$G(f,n) = G_s(f,n) + G_{\mathrm{DNA}}(n). \tag{2.6}$$

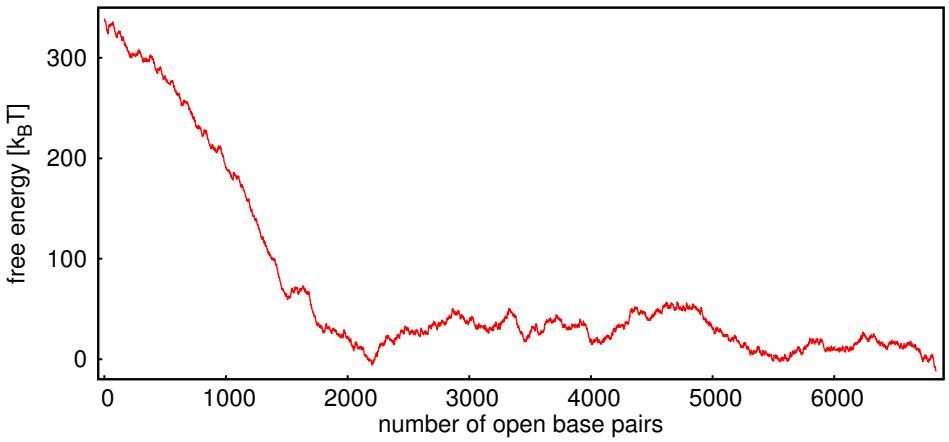

FIGURE 2.2.: Free energy profile $G(f, n)$ of a long 6838 base pairs DNA hairpin with numerous intermediate states for the applied force $f = 17.1\,\mathrm{pN}$.

As illustration, the free energy profile of the long hairpin is shown in Fig. 2.2 for a force for which the hairpin has several coexisting intermediate states. At larger forces, the more unfolded states become energetically favored, while decreasing the force tends to fold the DNA. Changing the force randomly over time thus drives the DNA stochastically across its free energy profile, similarly to if one had increased the temperature of the heat bath. This analogy will be further explored in Chapter 4.

3. Stochastic Dynamics

In this chapter, the unfolding dynamics of the DNA hairpin introduced in Chapter 2 will be discussed. This dynamics gets a stochastic contribution through the water molecules the hairpin is surrounded by. At finite temperatures, these molecules are in perpetual motion and thus permanently kick against the hairpin. Since the water molecules move much faster than the DNA, these kicks appear as random and hence force the hairpin on a stochastic trajectory.

The first experimental observation of this kind of stochastic motion is attributed to Robert Brown, a botanist who in 1827 investigated small pollen immersed in water with a microscope [47]. At the beginning of the 20th century, works by Einstein [48], Smoluchowski [49] and Langevin [50] gave a theoretical explanation for this phenomenon. Their framework has soon afterwards been confirmed in various experiments, including the Nobel-prize winning work by Perrin [51] who verified Einstein's diffusion law and thus gave first experimental evidence for the existence of atoms. Nowadays, the stochastic dynamics of mesoscopic objects in aqueous solution is well-established and reviewed in many textbooks [52–54]. In particular, the stochastic dynamics has been formally derived from the underlying microscopic dynamics which explicitly incorporates the dynamics of the heat bath [55–57].

A system with a stochastic dynamics can be described on different, yet equivalent levels. On the lowest level, one considers single realizations of the stochastic process, i.e., single trajectories of the system for specific sequences of random kicks by the water molecules. Another option is to look at the time evolution of the probability distribution of the full statistical ensemble to directly have information about the average system behavior. The Langevin equation is the fundamental equation of motion on the trajectory level for systems with a continuous degree of freedom such as the optically trapped bead. On the ensemble level, the time evolution of such systems is dictated by the Fokker-Planck equation. In the following, both the Langevin and the Fokker-Planck equation will be discussed in more detail (see Sec. 3.1 and Sec. 3.2). Furthermore, the master equation will be introduced as the analogue of the Fokker-Planck equation for discrete systems to be able to model the opening and closing of single base pairs in a DNA hairpin (see Sec. 3.3).

3.1. Langevin Equation

The *Langevin equation* describes the motion of a colloidal particle with mass m immersed in aqueous solution and subjected to an external force $F(x, \lambda)$ depending on both the position x of the particle and an external (possibly time-dependent) control parameter λ. In one dimension, the Langevin equation reads

$$m\ddot{x} + \gamma\dot{x} = F(x, \lambda) + \xi(t), \tag{3.1}$$

where γ is the friction coefficient and $\xi(t)$ the thermal force arising from the collisions of the particle with the water molecules. This force creates the irregular Brownian motion of the particle but has no systematic effect on it. Its statistical mean is therefore zero, i.e.,

$$\langle \xi \rangle = 0, \tag{3.2}$$

where here and in the following, $\langle \dots \rangle$ denotes the average over the statistical ensemble. Since the thermal force changes quickly with respect to the relaxation times of the colloidal particle, it can be assumed to be delta-correlated with

$$\langle \xi(t_2)\xi(t_1) \rangle = 2B\delta(t_2 - t_1). \tag{3.3}$$

The strength B of the thermal force is connected to the friction coefficient γ and the temperature T of the medium through the Einstein relation

$$B = \gamma k_B T, \tag{3.4}$$

where k_B is the Boltzmann constant, so that

$$\langle \xi(t_2)\xi(t_1) \rangle = 2\gamma k_B T\delta(t_2 - t_1). \tag{3.5}$$

The systematic external force $F(x, \lambda)$ on the colloidal particle in general in part stems from a potential $V(x, \lambda)$ and has a nonconservative contribution $f(x, \lambda)$, i.e.,

$$F(x, \lambda) = -\partial_x V(x, \lambda) + f(x, \lambda) \tag{3.6}$$

which inserted in Eq. 3.1 gives

$$m\ddot{x} + \gamma\dot{x} = -\partial_x V(x, \lambda) + f(x, \lambda) + \xi(t). \tag{3.7}$$

The first term $m\ddot{x}$ in this equation represents the inertia of the particle. This term acts on the time scale $\tau \equiv m/\gamma$ which for typical friction coefficients γ is

small compared to the other system relaxation times[1]. On these time scales, the inertia term can thus be neglected, leading to the *overdamped* Langevin equation

$$\dot{x} = \mu(-\partial_x V(x,\lambda) + f(x,\lambda)) + \zeta(t), \tag{3.8}$$

where the mobility $\mu \equiv 1/\gamma$ and the thermal noise $\zeta(t) \equiv \mu\xi(t)$ have been introduced.

3.2. Fokker-Planck Equation and Nonequilibrium Steady States

The ensemble level description of the stochastic dynamics considers the time evolution of the probability $p(x,t)$ for the system to be in position x at time t. Assuming that this probability is known, the Kramers-Moyal expansion [61,62] states that at a later time $t+\tau$, it has changed to

$$p(x,t+\tau) = \sum_{n=0}^{\infty} \frac{(-1)^n}{n!} \partial_x^n (M^n(x,t+\tau,t)p(x,t)), \tag{3.9}$$

with the moments

$$M^n(x,t+\tau,t) \equiv \langle (x(t+\tau) - x(t))^n \rangle \qquad n = 0,1,2,\ldots. \tag{3.10}$$

These moments can be calculated with the Langevin equation Eq. 3.8, leading to the *Fokker-Planck equation*

$$\begin{aligned} \partial_t p(x,t) &= \lim_{\tau\to 0} \frac{p(x,t+\tau) - p(x,t)}{\tau} \\ &= -\mu\partial_x(F(x,\lambda)p(x,t)) + D\partial_x^2 p(x,t) \end{aligned} \tag{3.11}$$

which governs the system dynamics on the ensemble level.
The Fokker-Planck equation can be written in the form of a continuity equation as

$$\partial_t p(x,t) = -\partial_x j(x,t), \tag{3.12}$$

introducing the probability current

$$j(x,t) \equiv \mu F(x,\lambda)p(x,t) - D\partial_x p(x,t). \tag{3.13}$$

[1] In recent years, experiments have accessed the short-time ballistic regime where the inertia is relevant [58–60].

If

$$\partial_t p(x,t) = 0, \tag{3.14}$$

the system is in a stationary state with probability distribution $p(x,t) = p^s(x)$. In particular, the system is in equilibrium with the Boltzmann distribution

$$p^{\mathrm{eq}}(x) = \frac{\exp(-V(x)/k_B T)}{\int_{-\infty}^{\infty} \exp(-V(x)/k_B T)\,\mathrm{d}x} \tag{3.15}$$

if the probability current Eq. 3.13 is zero. For time-independent non-zero currents $j(x) = j_s \neq 0$ on the other hand, the system is in a so-called *nonequilibrium steady state* (NESS) which is characterized by permanent heat dissipation and therefore needs external driving to be maintained.

3.3. Master Equation and Detailed Balance

The unfolding of DNA is a discrete process since it involves the breaking of single base pairs. A model for the unfolding dynamics can thus be reached by considering, in general terms, a discrete system which performs stochastic transitions within a set of states $\{n\}$, where $n = 1, 2, \ldots, N$. Referring to the rate for the transition from state n into m by k_{nm}, the probability for the system to be in state n at time t is governed by the *master equation*

$$\begin{aligned} \partial_t p_n &= \sum_{m=1}^{N} k_{mn} p_m - k_{nm} p_n \\ &= \sum_{m=1}^{N} L^0_{nm} p_m, \end{aligned} \tag{3.16}$$

with the time evolution operator

$$L^0_{nm} \equiv k_{mn} - \delta_{nm} \sum_l k_{nl}. \tag{3.17}$$

In analogy to Eq. 3.13, the master equation suggests that one identifies the probability current

$$j_{nm}(t) \equiv p_m k_{mn} - p_n k_{nm} \tag{3.18}$$

between the states n and m. If

$$\partial_t p_n = 0, \tag{3.19}$$

the system is in a stationary state [63] with distribution $p_n(t) = p_n^s$. As in the continuous case, this stationary state is either a NESS if the currents Eq. 3.18 are nonvanishing or corresponds to equilibrium if the currents are all zero. The equilibrium state with probability distribution p_n^{eq} thus satisfies the so-called *detailed balance* condition $j_{nm} = 0$, i.e.,

$$p_n^{\mathrm{eq}} k_{nm} = p_m^{\mathrm{eq}} k_{mn} \tag{3.20}$$

(see Eq. 3.18). The equilibrium distribution p_n^{eq} is the Boltzmann distribution, in analogy to Eq. 3.15.
In many cases, the discrete Markov dynamics described by the master equation cannot be solved analytically. Then, one can fall back on the numerical solution offered by the Gillespie algorithm (also known as BKL or kinetic Monte Carlo algorithm) which randomly generates both the transitions of the system and the times the system needs to jump [64, 65]. Suppose that the system is in state n after the last jump, then in each iteration, the algorithm first calculates the time increment according to

$$\Delta t = -\frac{\ln a}{\sum_{m=1}^{N} k_{nm}}, \tag{3.21}$$

where a is a random number uniformly distributed over the interval $(0, 1]$. In the next step, the algorithm lets the system perform a transition into the state j which satisfies

$$\sum_{m=1}^{j-1} k_{nm} < b \sum_{m=1}^{N} k_{nm} \leq \sum_{m=1}^{j} k_{nm}, \tag{3.22}$$

with b a uniform random number in $(0, 1]$ like a.

4. Effective Temperature in DNA Unfolding

The projects presented in the following two chapters have been developed in close collaboration with the experimental research group led by Felix Ritort at the Universitat de Barcelona. We stress that this chapter 4 is to a large extent based on the manuscript "Single molecule measurement of the effective temperature in nonequilibrium steady states" which will be published in Nature Physics [23].

4.1. Introduction

In equilibrium, the fluctuation-dissipation theorem (FDT) [66–68]

$$k_B T R^{\mathrm{eq}}(t_2, t_1) = \partial_{t_1} \langle x(t_2) B^{\mathrm{eq}}(t_1) \rangle, \tag{4.1}$$

connects the response

$$R^{\mathrm{eq}}(t_2, t_1) \equiv \left. \frac{\delta \langle x(t_2) \rangle}{\delta h(t_1)} \right|_{h=0} \tag{4.2}$$

of the observable x to an external perturbation h with a correlation function involving the (equilibrium) conjugate variable

$$B^{\mathrm{eq}} = -\partial_h E, \tag{4.3}$$

where E is the internal energy of the system. In this thesis, we have considered a perturbation of the force f for which $B^{\mathrm{eq}} = x$. Since the integrated response (or susceptibility) χ is experimentally available rather than the response R^{eq} itself, we consider the time-integrated version of the FDT

$$k_B T \chi(t) = C(t), \tag{4.4}$$

where

$$\chi(t) \equiv \langle x(t) - x(0) \rangle / \delta f, \tag{4.5}$$

with the size of the perturbation δf, and

$$C(t) \equiv \langle (x(0) - x(t))x(0) \rangle. \tag{4.6}$$

It has been shown that the equilibrium FDT Eq. 4.4 can be restored for a variety of nonequilibrium systems if one replaces the room temperature T by an effective temperature T_{eff} [22]. The resulting, so-called quasi-FDT then reads

$$k_B T_{\text{eff}} \chi(t) = C(t). \tag{4.7}$$

Examples where this effective temperature has been identified include glassy systems in the aging regime [21,69–73], jammed granular media [74] and driven and active matter [75–77] (see [78, 79] for reviews on granular media, glassy systems and active matter).
We rewrite the quasi-FDT Eq. 4.7 in the different, yet equivalent form

$$\frac{1}{k_{\text{B}} T_{\text{eff}}} = \frac{\partial \chi(C)}{\partial C}\Big|_{C=C(t)}, \tag{4.8}$$

to stress that one usually considers the so-called parametric plot $\chi(C)$, i.e., response χ over correlation function C, to identify an effective temperature. In fact, if this parametric plot is linear in some regime, χ is proportional to C with a single time-independent factor which (aside from a k_B) is the inverse of the effective temperature. We note that the quasi-FDT Eq. 4.8 should be distinguished from formally exact expressions for an FDT in a NESS that involve quantities that look physically less transparent and are harder to measure experimentally [80–85].
Here, we show for different systems spanning a wide range of complexity that the quasi-FDT Eq. 4.8 can be restored with an effective temperature T_{eff} if these systems are driven into a NESS by a random external force [86–89]. This external force $f(t) = f_c + f_{\text{di}}(t)$ has a mean value f_c and a contribution f_{di} which stochastically changes at rate $1/\tau_e$ between the two values $\pm\Delta f$, where τ_e is the external force switching time and Δf the force amplitude. The mean of this stochastic contribution is zero, i.e., $\langle f_{\text{di}}(t) \rangle = 0$, while its correlations obey

$$\langle f_{\text{di}}(0) f_{\text{di}}(t) \rangle = (\Delta f)^2 \exp(-2t/\tau_e). \tag{4.9}$$

The stochastic driving has been applied to three systems of increasing complexity, from a bead in an optical trap (Sec. 4.2) and a short (20 base pairs) hairpin which unfolds in a two-state manner when subject to an external force (see Sec. 4.3) to a long (6800 base pairs) hairpin with numerous intermediate states (see Sec. 4.4).

4.2. The Bead in the Optical Trap

The bead in the optical trap [30,60,90–94] serves as an illustration to the general theme as it can be analytically treated in the framework of an overdamped Langevin equation for its motion $x(t)$ as

$$\dot{x} = \mu(-\partial_x V(x) + f(t)) + \zeta(t) \tag{4.10}$$

(see Sec. 3.1). Here, we model the optical trap as a harmonic potential $V(x) = kx^2/2$ with stiffness k, μ is the mobility and $\zeta(t)$ is the thermal noise. This noise obeys $\langle\zeta(t)\rangle = 0$ and $\langle\zeta(t_2)\zeta(t_1)\rangle = 2\mu k_\mathrm{B}T\delta(t_2 - t_1)$, where $k_\mathrm{B}T$ is the thermal energy. We search for an effective temperature by looking at the parametric plot $\chi(C)$ where C is a correlation function of the bead position x and χ is the response of this quantity to a stepwise perturbation in the force f. If this parametric plot is linear in some regime, we can identify a quasi-FDT there. For the harmonic oscillator, the application of a force corresponds to shifting the potential, and therefore, one can experimentally implement the stochastic driving of this system by randomly switching the position of the trap in a dichotomous fashion (Fig. 4.1A and D). Along this NESS, the correlation function C and the response function χ were measured for three different values of the force switching time τ_e (Fig. 4.1B). We find that χ relaxes exponentially on the time scale $\tau_s = 1/(\mu k)$ which is the relaxation time of the bead in a harmonic trap. For all experiments where $\tau_e < \tau_s$, the parametric plots $\chi(C)$ clearly show a linear regime at large times and thus demonstrate the existence of an effective temperature in this driven harmonic oscillator system (right hand side of Fig. 4.1B). In Appendix A, we show that if the experiment is performed without applying external forces, i.e., without moving the trap, the usual equilibrium FDT Eq. 4.1 holds. We stress that the experimental results are in good agreement with the predictions we obtain by modeling the bead dynamics with the Langevin equation Eq. 4.10. This model will be discussed in the following.

Langevin model

For the Langevin dynamics of the driven harmonic oscillator described by Eq. 4.10, the response Eq. 4.5

$$\chi(t) \equiv \langle x(t) - x(0)\rangle/\delta f \tag{4.11}$$

of the bead position x to a step-like perturbation δf setting in at $t = 0$ is

$$\chi(t) = \frac{1}{k}\left(1 - \mathrm{e}^{-t/\tau_s}\right), \tag{4.12}$$

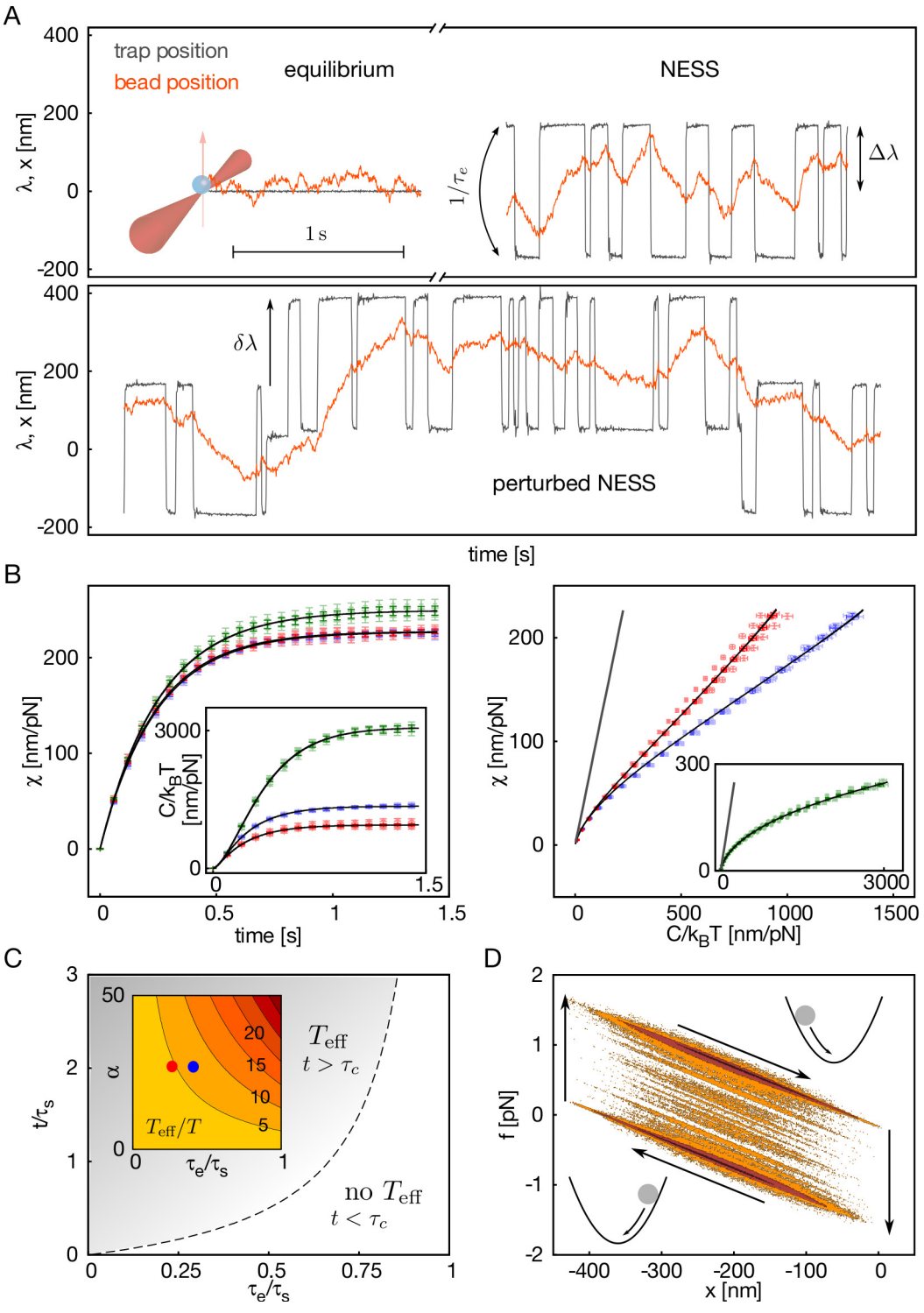
A
trap position
bead position
equilibrium
NESS
1 s
$1/\tau_e$
$\Delta\lambda$
$\delta\lambda$
perturbed NESS
λ, x [nm]
time [s]
B
χ [nm/pN]
time [s]
C/k_BT [nm/pN]
C/k_BT [nm/pN]
C
t/τ_s
τ_e/τ_s
α
$T_{\rm eff}/T$
$T_{\rm eff}$
$t > \tau_c$
no $T_{\rm eff}$
$t < \tau_c$
D
f [pN]
x [nm]

FIGURE 4.1: The bead in the optical trap.
(**A**) Sketch for the bead in a time-dependent harmonic trap and experimental traces of the position λ of the optical trap (gray) and the position x of the bead (orange). The relaxation time of the bead is $\tau_s \simeq 200 - 250\,\mathrm{ms}$ in all following experiments. The system is driven into a NESS by changing λ dichotomously at the rate $1/\tau_e$ with the amplitude $\Delta\lambda$. A perturbation is applied by shifting the position of the optical trap in a stepwise manner by $\delta\lambda$. The force amplitude and force perturbation follow as $\Delta f \equiv k\Delta\lambda$ and $\delta f = k\delta\lambda$, respectively, where k is the stiffness of the trap.
(**B**) On the left hand side, response function $\chi(t) \equiv \langle x(t) - x(0)\rangle/\delta f$ for a stepwise perturbation setting in at $t = 0$ (main plot) and correlation function $C(t) \equiv \langle (x(0) - x(t))x(0)\rangle$ measured over the unperturbed NESS (inset). The experimental parameters are $\Delta f \simeq 0.7\,\mathrm{pN}$ ($\Delta\lambda \simeq 160\,\mathrm{nm}$), $\delta f \simeq 1.0\,\mathrm{pN}$ ($\delta\lambda \simeq 220\,\mathrm{nm}$) and $\tau_e = 67\,\mathrm{ms}$ (red), $\tau_e = 100\,\mathrm{ms}$ (blue) and $\tau_e = 333\,\mathrm{ms}$ (green). Note that for χ, we can use perturbation sizes $\delta f > \Delta f$ since the driven harmonic oscillator is fully linear (Eq. 4.10, this statement is also confirmed by the experimental verification of the equilibrium FDT presented in Appendix A). We show an average over four beads in the respective darker color and results for single beads in lighter colors. Predictions from the Langevin model of the system are shown in black. On the right hand side, the corresponding parametric plots for $\tau_e = 67\,\mathrm{ms}$, $\tau_e = 100\,\mathrm{ms}$ (main plot) and $\tau_e = 333\,\mathrm{ms}$ (inset). The values $T_{\mathrm{eff}} \simeq 5\,\mathrm{T} = 1490\,\mathrm{K}$ (red) and $T_{\mathrm{eff}} \simeq 7\,\mathrm{T} = 2086\,\mathrm{K}$ (blue) indicate substantial deviation from the equilibrium FDT (gray).
(**C**) Identification of an effective temperature regime from the solvable model Eq. 4.10. We show the analytical dependence of τ_c (main plot, dashed line, Eq. 4.17) and T_{eff} (inset contour plot, Eq. 4.18) versus τ_e/τ_s and the scaled force amplitude $\alpha \equiv (\Delta f^2/k)/k_{\mathrm{B}}T$, where the dots mark the experimental conditions. A green point corresponding to $\tau_e = 333\,\mathrm{ms}$ is not shown because no T_{eff} was found in that case ($\tau_e/\tau_s > 1$).
(**D**) Contour plot of the logarithmic histogram of a stochastically driven trajectory with $\Delta f \simeq 0.7\,\mathrm{pN}$ and $\tau_e = 100\,\mathrm{ms}$. The bead (gray dot) in average tends to relax towards the minimum of the harmonic potential. As the position of this minimum is permanently changed in a dichotomous fashion (vertical arrows), the bead in average shows clockwise motion in the (x, f) plane leading to dissipation of heat. Figure reprinted from [23].

with $\tau_s = 1/\mu k$. The correlation function Eq. 4.6

$$C(t) \equiv \langle (x(0) - x(t))x(0) \rangle \tag{4.13}$$

is evaluated over the unperturbed NESS and follows as

$$\begin{aligned} C(t) =& \frac{k_\mathrm{B}T}{k} \left(1 - \mathrm{e}^{-t/\tau_s}\right) \\ &+ \frac{2(\Delta f/k)^2}{\tau_e(1-(2\tau_s/\tau_e)^2)} \left(\frac{\tau_e}{2}\left(1 - \mathrm{e}^{-2t/\tau_e}\right) - \tau_s\left(1 - \mathrm{e}^{-t/\tau_s}\right)\right). \end{aligned} \tag{4.14}$$

With these expressions, we find the parametric plot

$$C(\chi) = k_\mathrm{B}T\chi + \frac{2(\Delta f/k)^2}{\tau_e(1-(2\tau_s/\tau_e)^2)} \left(\frac{\tau_e}{2}\left(1 - (1-k\chi)^{2\tau_s/\tau_e}\right) - \tau_s k\chi\right) \tag{4.15}$$

and its curvature

$$\frac{\partial^2 C(\chi(t))}{\partial(\chi(t))^2} \sim \exp\left(-\frac{2(\tau_s/\tau_e - 1)t}{\tau_s}\right) \equiv \exp\left(-t/\tau_c\right) \tag{4.16}$$

with

$$\tau_c/\tau_s = \frac{1}{2(\tau_s/\tau_e - 1)}. \tag{4.17}$$

The approximate linearity of the parametric plot for all times $t \gtrsim \tau_c$ suggests that τ_c is the crossover time into an effective temperature regime (Fig. 4.1C). The value of the effective temperature is the slope of the parametric plot in the limit $t \gg \tau_c$ where its curvature has become negligible, leading to

$$T_\mathrm{eff}/T = \frac{1}{k_B T} \left.\frac{\partial C(\chi(t))}{\partial \chi(t)}\right|_{t \gg \tau_c} \approx 1 + \frac{2\alpha\tau_s}{\tau_e((2\tau_s/\tau_e)^2 - 1)} \tag{4.18}$$

with the scaled force amplitude $\alpha = ((\Delta f^2)/k)/k_\mathrm{B}T$.
For $\tau_e \ll \tau_s$, the crossover time is $\tau_c \approx \tau_e/2$, so that only for very short times ($t < \tau_c$), correlation and response are not related by an effective temperature which, in this limit, is

$$T_\mathrm{eff}/T \approx 1 + \frac{\alpha\tau_e}{2\tau_s}. \tag{4.19}$$

The increase of the temperature generated by the stochastic driving becomes particularly transparent in this limit $\tau_e \ll \tau_s$ since the stochastic forces then act as additional thermal noise to the system.
For larger τ_e outside the limit $\tau_e \ll \tau_s$, the effective temperature regime gets smaller (τ_c gets larger) and ultimately vanishes for $\tau_e = \tau_s$. The experimental condition $\tau_e < \tau_s$ for the existence of an effective temperature T_eff is thus naturally recovered in this model.

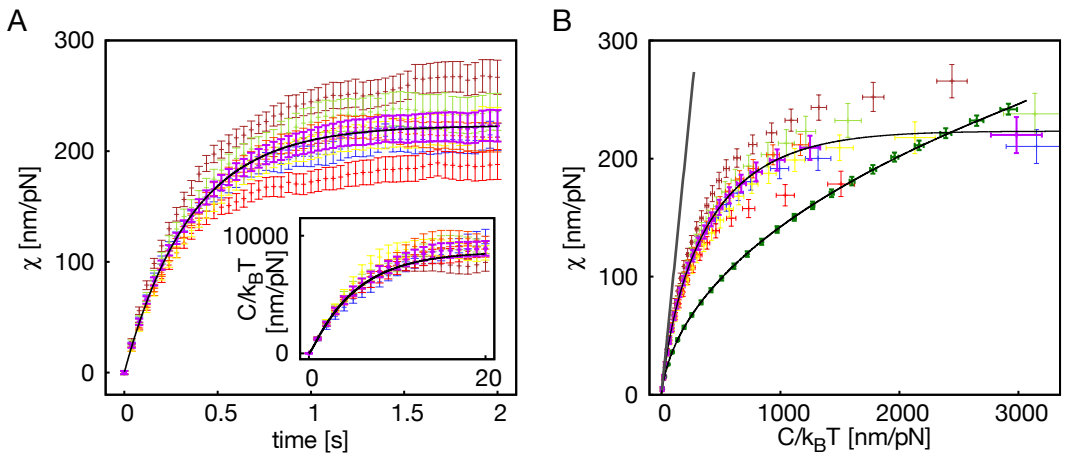

FIGURE 4.2.: The limit $\tau_e \gg \tau_s$ for the bead in the optical trap.
(**A**) Experimental (colors) and theoretical (black) response χ (main frame) and correlation function C (inset) in the limit $\tau_e \gg \tau_s$. For the experimental parameters $\Delta f \simeq 0.9\,\mathrm{pN}$, $\delta f \simeq 1.1\,\mathrm{pN}$ and $\tau_e = 10\,\mathrm{s}$, the results for six single beads (various colors) and their average (violet) are shown.
(**B**) The corresponding parametric plots where the gray line represents the equilibrium FDT. We include from Fig. 4.1B the experimental (dark green) and theoretical (black) parametric plot for $\Delta f \simeq 0.7\,\mathrm{pN}$, $\delta f \simeq 1.0\,\mathrm{pN}$ and $\tau_e = 333\,\mathrm{ms}$. Figure reprinted from [23].

The Limit $\tau_e \gg \tau_s$

For force switching times $\tau_e \gg \tau_s$, the expression for the correlation function Eq. 4.14 turns into

$$C(t) \approx \frac{k_\mathrm{B}T}{k}\left(1 - \mathrm{e}^{-t/\tau_s}\right) + (\Delta f/k)^2\left(1 - \mathrm{e}^{-2t/\tau_e}\right) \tag{4.20}$$

while the response Eq. 4.12 remains the same. In this limit, the equilibrium FDT is restored for times $t \ll \tau_e$ since

$$C(t \ll \tau_e) \approx \frac{k_\mathrm{B}T}{k}\left(1 - \mathrm{e}^{-t/\tau_s}\right) = k_B T \chi \qquad (\tau_e \gg \tau_s), \tag{4.21}$$

reflecting the equilibration of the bead for each applied force.

To further illustrate this limit, we have experimentally measured the response χ and the correlation function C for a large force switching time $\tau_e \gg \tau_s$ (see Fig. 4.2A). The corresponding parametric plot Fig. 4.2B demonstrates that in comparison to a more moderate $\tau_e \simeq \tau_s$, the system is noticeably closer to

	τ_e [ms]	$\Delta\lambda$ [nm]	k [pN/nm]	τ_s [ms]
experiment	67	163.5	$C:$ 0.00424 $\chi:$ 0.00428	$\simeq 200-250$
theory: C	55	163.5	0.00424	222
theory: χ	-	-	0.00440	235
experiment	100	162	$C:$ 0.00425 $\chi:$ 0.00429	$\simeq 200-250$
theory: C	96	162	0.00425	226
theory: χ	-	-	0.00441	240
experiment	333	162.5	$C:$ 0.00423 $\chi:$ 0.00414	$\simeq 200-250$
theory: C	346	162.5	0.00423	219
theory: χ	-	-	0.00401	254
experiment	10 s	191.5	$C:$ 0.00481 $\chi:$ 0.00473	$\simeq 300-400$
theory: C	10.56 s	191.5	0.00481	298
theory: χ	-	-	0.00448	356

TABLE 4.1.: The experimental and theoretical parameters for the bead in the optical trap. The position amplitude $\Delta\lambda$, the stiffness k and the system relaxation time τ_s is listed for experiments at four different position switching times τ_e. Among these parameters, we use τ_s and τ_e as fit parameters in Eq. 4.14 for C, and k and τ_s as fit parameters in Eq. 4.12 for χ. The experimental estimate of the system relaxation time τ_s has been obtained from repeated measurements of the equilibrium force autocorrelation function. Table reprinted from [23].

equilibrium in the short-time regime (i.e., for small χ and C). We point out that the larger variability between results for single beads is due to the large force switching time used which causes the system to relax more slowly into the stationary state. Since the trajectory cannot exceed a certain length to avoid a change of the experimental conditions over time, the statistics of χ and C thus gets worse in the limit $\tau_e \gg \tau_s$. However, the statistics is still good enough to clearly resolve that the system is closer to equilibrium in the short-time regime.

Comparing Theory and Experiment

After a discussion of the different regimes of the force switching time τ_e, we now verify the earlier statement that theory and experiment agree well for the bead in the optical trap by comparing the predictions from the Langevin model with the experimental response and correlation functions shown in Fig. 4.1B and 4.2A and B. We find that for all four values of τ_e considered, the experimental results can be reproduced well by plugging the parameters listed in Table 4.1 in the respective theoretical expression for χ and C.
The difference between these parameters and their experimental counterparts is less than five percent in most cases, with the comparatively large deviation between the experimental $\tau_e = 67\,\mathrm{ms}$ and the theoretical $\tau_e = 55\,\mathrm{ms}$ as the sole exception. This deviation can be attributed to the fact that for fast switching, i.e., for small τ_e, the optical trap struggles to accurately follow the external protocol for its position. In these conditions, the experimental τ_e can therefore be somewhat different from the externally chosen parameter.

4.3. The Two-State Short Hairpin

The harmonic oscillator has been used as a first simple example to illustrate the emergence of an effective temperature in systems subject to stochastic driving. We next consider single molecules with free energy landscapes far more complex than the harmonic potential, leading to a more complex stationary dynamics under the action of random forces. We have chosen DNA hairpins as experimental model systems to address such questions [36, 95, 96].
We start our study with short DNA hairpins (20 bp stem ended by a tetraloop) which can either be in the folded or in the unfolded state if an external force f is applied.

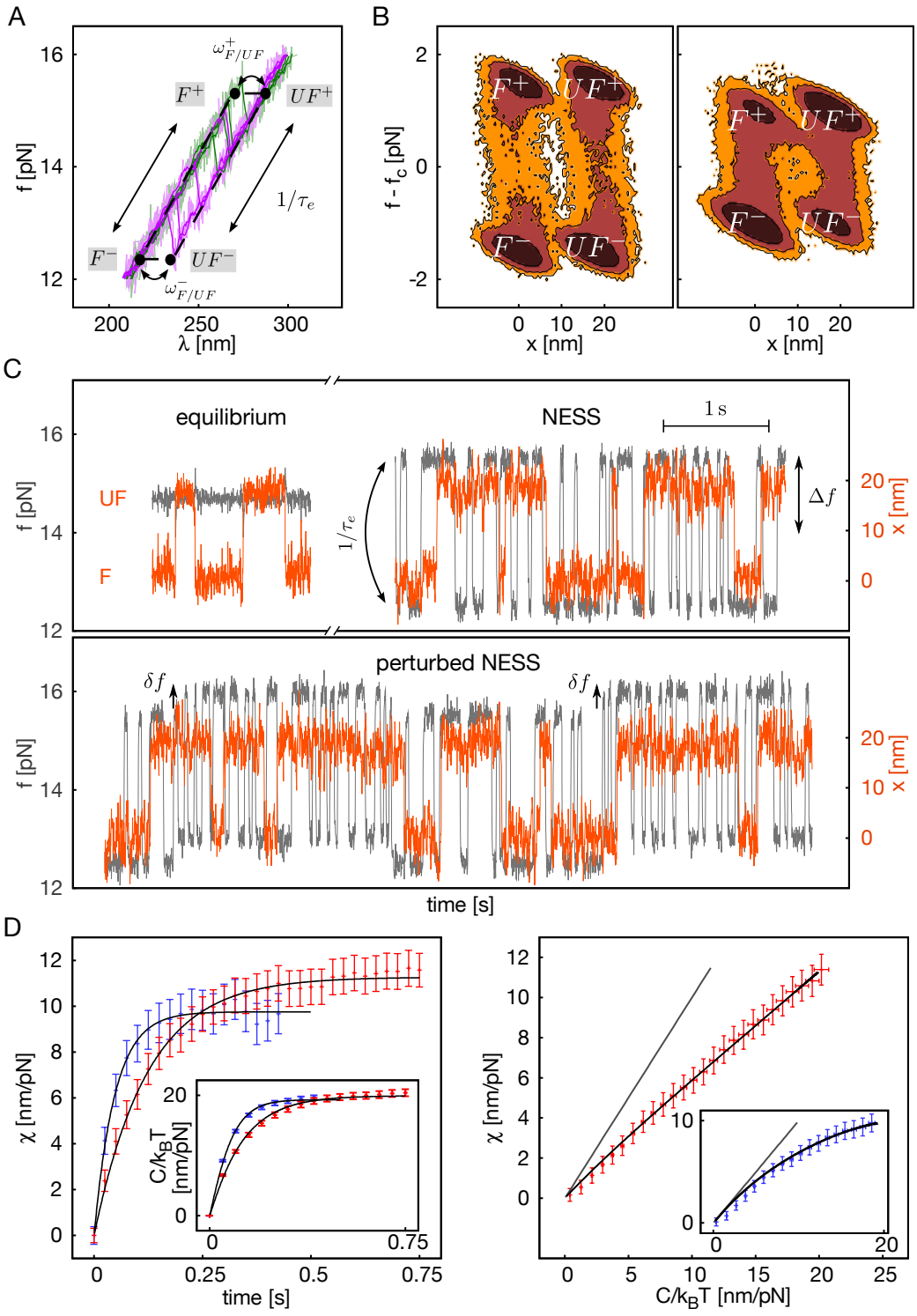
A
B
C
D
f [pN]
λ [nm]
F^+
UF^+
F^-
UF^-
$1/\tau_e$
f - f_c [pN]
x [nm]
equilibrium
NESS
1 s
UF
F
Δf
x [nm]
perturbed NESS
δf
time [s]
χ [nm/pN]
C/k_BT [nm/pN]

FIGURE 4.3: Short hairpin systems.
(**A**) Experimental force-distance curves for the short DNA hairpin. The tethered hairpin is unfolded (green) and refolded (purple) by moving the optical trap back and forth (increase/decrease λ). Data is recorded at 1 kHz (dark colors) and filtered to 20 Hz (light colors). We use feedback to change f between $\pm \equiv f_c \pm \Delta f$ at rate $1/\tau_e$. For a perfect (infinite bandwidth) feedback, the dynamics follows the black dashed line, where $UF^{\pm}/F^{\pm}$ and $\omega^{\pm}_{UF/F}$ refer to the unfolded/folded state and unfolding/folding rate at force $\pm$ in an effective four state model. The force-distance curves have already been shown in Fig. 2.1.
(**B**) Experimental contour plot of the logarithmic probability distribution of a driven hairpin with slow (top) and fast (bottom) hopping kinetics. The experimental parameters for the slow (fast) hairpin are $f_c = 14\,\mathrm{pN}$, $\Delta f = 1.5\,\mathrm{pN}$ and $\tau_e = 50\,\mathrm{ms}$ ($f_c = 15\,\mathrm{pN}$, $\Delta f = 1\,\mathrm{pN}$ and $\tau_e = 100\,\mathrm{ms}$). For the fast hairpin, the populations of the states UF^+ and F^- are enhanced since the force switching is here relatively slow compared to the conformational dynamics. The relaxation time τ_s is $\tau_s \simeq 120\,\mathrm{ms}$ ($\tau_s \simeq 50\,\mathrm{ms}$) for the slow (fast) hairpin.
(**C**) Experimental traces of the force f (gray) and the molecular extension $x \equiv \lambda - f/k - x_0$ (orange, x_0 is an offset) with δf the perturbation size.
(**D**) Response function $\chi(t) \equiv \langle x(t) - x(0)\rangle/\delta f$ for a stepwise perturbation with size $\delta f = 0.5\,\mathrm{pN}$ setting in at $t = 0$ (main plot) and correlation function $C(t) \equiv \langle (x(0) - x(t))x(0)\rangle$ measured over the unperturbed NESS (inset) for the slow (red) and the fast (blue) hairpin. We show an average over five (four) molecules for χ and ten (five) molecules for C for the slow (fast) hairpin. Theoretical predictions from the driven two state model are displayed in black. On the right hand side, we show the corresponding parametric plots and the equilibrium FDT prediction (gray). The effective temperature is $T_{\mathrm{eff}} \simeq 2\,\mathrm{T} = 596\,\mathrm{K}$ for the slow hairpin (red). For the fast hairpin, there is no T_{eff} since $\tau_e > \tau_s$ in this case. Figure reprinted from [23].

The stochastic driving is implemented by randomly changing this force at rate $1/\tau_e$ between $f_c - \Delta f$ and $f_c + \Delta f$, below and above the value of the coexistence force f_c of the hairpin, where the folded and unfolded states are equally populated (Fig. 4.3A - C). The controlled force is applied by a feedback loop operating on a millisecond time scale much shorter than any of the two characteristic times τ_s and τ_e, thereby leaving correlations and responses unchanged in the relevant time regime where the effective temperature is observed. A general discussion of the force feedback in DNA unfolding based on experimental data and simulations which explicitly include the feedback mechanism is given for the long hairpin in Chapter 5.
We have measured the correlation function C of the molecular extension and the response χ of this variable to a stepwise perturbation in the applied force for two different short hairpin sequences which in equilibrium show different hopping rates (that we will refer to as fast and slow). In Appendix A, we compare traces of these two hairpins to illustrate their different hopping dynamics. Driving the fast and the slow hairpin into a NESS with a similar force protocol, we find (i) the response of both sequences relaxes on a single time scale τ_s as in the case of the harmonic oscillator, and (ii) this time scale τ_s is noticeably smaller for the fast hopper. In particular, we observe that for this hairpin τ_s falls below the force switching time τ_e (see Fig. 4.3D, where we show averages over several single-molecule experiments, the results of these experiments are given in Appendix B). The corresponding parametric plot then remains curved for all times (right hand side of Fig. 4.3D) and an effective temperature cannot be identified. In contrast, a linear regime and thus an effective temperature can be observed in the parametric plot of the slow hopper, where $\tau_e < \tau_s$. In analogy to the harmonic oscillator system, we thus find $\tau_e < \tau_s$ as the necessary condition for a quasi-FDT and an effective temperature in the driven short hairpin system. To support these results, Appendix A demonstrates that we again have verified that in equilibrium conditions (i.e., the random switching protocol turned off), the usual FDT Eq. 4.1 is fulfilled.
The driven two-state hairpin can be modeled by an effective four-state Markovian dynamics (Fig. 4.3A) for which exact expressions for the response χ and correlation function C can be derived, as will be shown in the following.

The Driven Two-State System

For any applied force, the short hairpin can either be in the unfolded state UF or in the folded state F. If one applies the stochastic driving where the force is changed in a dichotomous fashion between two values $\pm = f_c \pm \Delta f$, the system therefore has four states (see Fig. 4.3A and B). Following the notation

introduced in Fig. 4.3A, we refer to these states as $\{F^+, UF^+, F^-, UF^-\}$. The transitions between the states occur at rate $1/\tau_e$ if the force is changed and at the rate $\omega^{\pm}_{F/UF}$ if the hairpin folds/unfolds at force $\pm$.
The probability to be in state $m \in \{1,2,3,4\} \equiv \{F^+, UF^+, F^-, UF^-\}$ at time t is governed by the master equation (see Sec. 3.3)

$$\partial_t p_m(t) = \sum_n L^0_{mn} p_n(t), \tag{4.22}$$

with

$$\begin{aligned} L^0_{mn} &= \begin{pmatrix} -(1/\tau_e + \omega^+_{\mathrm{UF}}) & \omega^+_{\mathrm{F}} & 1/\tau_e & 0 \\ \omega^+_{\mathrm{UF}} & -(1/\tau_e + \omega^+_{\mathrm{F}}) & 0 & 1/\tau_e \\ 1/\tau_e & 0 & -(1/\tau_e + \omega^-_{\mathrm{UF}}) & \omega^-_{\mathrm{F}} \\ 0 & 1/\tau_e & \omega^-_{\mathrm{UF}} & -(1/\tau_e + \omega^-_{\mathrm{F}}) \end{pmatrix} \\ &\equiv k_{nm} - \delta_{mn} \sum_l k_{ml}, \end{aligned} \tag{4.23}$$

where the rates k_{mn} comprise both the (un)folding rates $\omega^{\pm}_{(\mathrm{U})\mathrm{F}}$ and the force switching rate $1/\tau_e$. With each state m, we can associate a molecular extension according to

$$x_1 = 0 \qquad x_2 = x_{\mathrm{UF}} \qquad x_3 = 0 \qquad x_4 = x_{\mathrm{UF}}, \tag{4.24}$$

where x_{UF} equals the distance between the states F and UF. The linear response of this molecular extension x to a stepwise force perturbation δf setting in at $t = 0$ is defined as in Eq. 4.5 with

$$\chi(t) \equiv \langle x(t) - x(0) \rangle / \delta f. \tag{4.25}$$

Exploiting the general theory of the response in a NESS developed in Ref. [84], χ can be expressed by

$$\chi(t) = \int_0^t \langle x(\Delta t) B(0) \rangle \, \mathrm{d}\Delta t \tag{4.26}$$

as the time integral over a correlation function involving the variable B which is conjugate to the perturbation. The integral over time is necessary to change from the response to a delta-like perturbation used in Ref. [84] to the response to a stepwise perturbation considered here. We point out that B is the nonequilibrium steady state analogue to the equilibrium conjugate variable B^{eq} which appears in the equilibrium FDT

$$k_B T \chi^{\mathrm{eq}}(t) = \int_0^t \partial_{t_1} \langle x(t_2) B^{\mathrm{eq}}(t_1) \rangle \, \mathrm{d}(t_2 - t_1). \tag{4.27}$$

This quantity B^{eq} is conjugate to the perturbation f and takes the form

$$B^{\mathrm{eq}} = -\partial_f G \tag{4.28}$$

for our systems, where G is the free energy of the hairpin (see Eq. 2.6). In the NESS, the conjugate variable B has been shown to have different, yet equivalent representations all reproducing with the FDT Eq. 4.26 the NESS response χ of the system to a perturbation f (see Ref. [84]).
For the driven two state system, Eq. 4.26 turns into

$$\chi(t) = \int_0^t \sum_{mn} x_m \mathrm{prob}(m, \Delta t|n, 0) B_n p_n^s \, \mathrm{d}\Delta t, \tag{4.29}$$

where p_n^s is the stationary distribution and where $\mathrm{prob}(m, \Delta t|n, 0)$ is the conditional probability for the system to be in state m at time Δt provided that it was in state n at time $t = 0$. This probability can be calculated by solving the master equation Eq. 4.22, leading to

$$\chi(t) = \int_0^t \sum_{mn} x_m \left[\exp(L^0 \Delta t)\right]_{mn} B_n p_n^s \, \mathrm{d}\Delta t. \tag{4.30}$$

The conjugate variable B can be written in the "Agarwal form" (among other equivalent representations, as pointed out above)

$$B_n = \sum_l (p_l^0/p_n^s) k_{ln} \alpha_{ln} - \sum_l k_{nl} \alpha_{nl}, \tag{4.31}$$

with $\alpha_{nl} \equiv \partial_f \ln k_{nl}$ (with f being the perturbation). The response Eq. 4.30 is compared to the correlation function defined in Eq. 4.6 which takes the expression

$$C(t) \equiv \langle (x(0) - x(t)) x(0) \rangle = \sum_{mn} x_m \left(\delta_{mn} - \left[\exp(L^0 t)\right]_{mn}\right) x_n p_n^s. \tag{4.32}$$

for the driven two-state system.
Both χ and C can be simplified by expanding with

$$B_n p_n^s \equiv \sum_i c_\chi^{(i)} v_n^{(i)} \qquad x_n p_n^s \equiv \sum_i c_C^{(i)} v_n^{(i)} \qquad n = 1, 2, 3, 4 \tag{4.33}$$

in eigenstates $v^{(i)}$ of L^0 with eigenvalues $\lambda^{(i)}$. Then,

$$\chi(t) = -\sum_{im} x_m v_m^{(i)} c_\chi^{(i)} (1 - \exp(\lambda^{(i)} t))/\lambda^{(i)}, \tag{4.34}$$

$$C(t) = \sum_{im} x_m v_m^{(i)} c_C^{(i)} (1 - \exp(\lambda^{(i)} t)). \tag{4.35}$$

For this system, apart from the trivial eigenvalue

$$\lambda^{(0)} = 0 \tag{4.36}$$

corresponding to the NESS, the three eigenvalues characterizing the relaxation in this NESS are

$$\lambda^{(1)} = -2/\tau_e \tag{4.37}$$

and

$$\begin{aligned}\lambda^{(2,3)} = &- (1/\tau_e + (\omega_{\mathrm{UF}}^{+} + \omega_{\mathrm{F}}^{+} + \omega_{\mathrm{UF}}^{-} + \omega_{\mathrm{F}}^{-})/2 \\ &\pm \left[1/\tau_e^2 + (\omega_{\mathrm{UF}}^{-} - \omega_{\mathrm{UF}}^{+} + \omega_{\mathrm{F}}^{-} - \omega_{\mathrm{F}}^{+})^2/4\right]^{\frac{1}{2}}).\end{aligned} \tag{4.38}$$

The fact that τ_e is independent of the perturbation leads to $c_\chi^1 = 0$. In contrast to the correlation function, the response therefore has no contribution from the time scale $\tau^{(1)} \equiv -1/\lambda^{(1)} = \tau_e/2$. The time scales $\tau^{(2,3)} \equiv -1/\lambda^{(2,3)}$ differ from $\tau^{(1)}$ in that they reflect properties of the hairpin via the (un)folding rates $\omega_{(U)F}^{\pm}$. Since $\tau^{(2)} < \tau^{(1)}$, the contribution of $\tau^{(2)}$ converges faster than the violation (curvature) term associated with $\tau^{(1)}$. Moreover, in the experimental conditions, this fast time scale $\tau^{(2)}$ can be neglected even in the short-time regime (see below comparison of theory and experiment). In analogy to the harmonic oscillator system, the two relevant relaxation times of the driven two state system are $\tau^{(1)} = \tau_e/2$ and $\tau^{(3)} \equiv \tau_s$. We thus recover both, $\tau_e < \tau_s$ as the condition for an effective temperature, and τ_c from Eq. 4.17 as the time scale beyond which the parametric plot $\chi(C)$ becomes linear.
The effective temperature of the driven two state system then follows as

$$T_{\mathrm{eff}}/T = \frac{1}{k_B T} \left.\frac{\partial C(\chi(t))}{\partial \chi(t)}\right|_{t \gg \tau_c} \approx \frac{c_C^{(3)}}{k_{\mathrm{B}} T c_\chi^{(3)} \tau^{(3)}}. \tag{4.39}$$

This expression illustrates that the effective temperature only depends on the constants $c_\chi^{(3)}$ and $c_C^{(3)}$ and the time scale $\tau^{(3)}$. Through Eq. 4.33 and 4.38, respectively, these quantities are connected with the molecular extension and the (un)folding rates of the hairpin, the change of these rates to a force perturbation and the driving parameters Δf and τ_e of the external forcing. We stress that by replacing the observable "molecular extension x_m" by an arbitrary other observable A_m, the expression Eq. 4.39 for the effective temperature remains the same. The effective temperature Eq. 4.39 of the driven two-state system is thus independent of the choice of the observable which adds further support to T_{eff} playing the role of the temperature of the system. We stress that this result is not trivial since the effective temperature of a system can in general be observable-dependent (see, e.g., [97]).

Comparing Theory and Experiment

On the level of single base pairs, the free energy of the short hairpin can be modeled as

$$G(f,n) = G_{\mathrm{DNA}}(n) - \int_0^f x(f',n)\,\mathrm{d}f' \tag{4.40}$$

given an applied force f and for the first n base pairs open (see Eq. 2.6). The four-state model, however, describes the hairpin on a more coarse-grained level since it only distinguishes between the folded state F and the unfolded state UF. We model the free energy of these two states as

$$G_F = G_F^0 \quad \text{and} \quad G_{UF} = G_{UF}^0 - afx_{UF} \tag{4.41}$$

where $G_{F/UF}^0$ is the respective free energy at zero force. Here, we have exploited that in the folded state the hairpin has no molecular extension. We need to keep a as a fit parameter which, however, will turn out to take the naively expected value $a = 1$ for both equilibrium and the NESS of the fast hairpin. We demand that detailed balance is fulfilled for the unfolding and folding rate at each applied force. In particular, detailed balance has to hold for the two forces $\pm = f_c \pm \Delta f$ used in the stochastic driving, so that

$$\frac{\omega_{UF}^{\pm}}{\omega_F^{\pm}} = \exp(-(G_{UF}^0 - G_F^0 - a(f_c \pm \Delta f)x_{UF})/k_BT) \tag{4.42}$$

Since experimentally the unfolded and folded state are almost equally populated when subject to the stochastic driving, we can assume that f_c is the coexistence force of the hairpin so that $G_{UF}^0 - G_F^0 = af_cx_{UF}$ and

$$\frac{\omega_{UF}^{\pm}}{\omega_F^{\pm}} = \exp(\pm a\Delta f x_{UF}/k_BT). \tag{4.43}$$

Moreover, these two states are equally populated for any value of the force switching time τ_e and the force amplitude Δf only if

$$\omega_{UF}^{+} = \omega_F^{-} \quad \text{and} \quad \omega_{UF}^{-} = \omega_F^{+}, \tag{4.44}$$

which suggests that a symmetric splitting of the ratio in Eq. 4.43 can be used. Hence, we model the experimental unfolding and folding rate at force $\pm$ by

$$\omega_{UF}^{\pm} = k_0 \exp(\pm a\Delta f x_{UF}/2k_BT) \tag{4.45}$$

$$\omega_F^{\pm} = k_0 \exp(\mp a\Delta f x_{UF}/2k_BT), \tag{4.46}$$

with the hopping frequency at coexistence k_0.
Experimentally, the force amplitude Δf is large so that

$$\omega_{UF}^{+} \gg \omega_{F}^{+} \quad \text{and} \quad \omega_{UF}^{-} \ll \omega_{F}^{-}. \tag{4.47}$$

Referring to the fastest rates by

$$\omega^* \equiv \omega_{UF}^{+} = \omega_{F}^{-}, \tag{4.48}$$

the expressions Eq. 4.34 for the response and Eq. 4.35 for the correlation function become

$$\chi(t) = \frac{a x_{UF}^2}{2k_B T(2 + \tau_e \omega^*)}(1 - \exp(-\omega^* t)) \tag{4.49}$$

and

$$C(t) = \frac{x_{UF}^2}{4(4 - (\tau_e \omega^*)^2)}(4(1 - \exp(-\omega^* t)) - (\tau_e \omega^*)^2(1 - \exp(-2t/\tau_e))) \tag{4.50}$$

in the experimentally relevant regime of τ_e in the order of $1/\omega^*$ and smaller. Fitting these expressions to the experimental response and correlation functions gives $\omega^* \simeq 8.2\,\mathrm{s}^{-1}$, $a \simeq 0.68$ and $x_{UF} \simeq 18.1\,\mathrm{nm}$ for the slow hopper (red curve in Fig. 4.3D) and $\omega^* \simeq 20.7\,\mathrm{s}^{-1}$, $a \simeq 1.03$ and $x_{UF} \simeq 17.8\,\mathrm{nm}$ for the fast one (blue curve in the same figure). We point out that the response Eq. 4.49 and the correlation function Eq. 4.50 show that under the experimental conditions, the relaxation time τ_s is simply the inverse of the unfolding rate at the larger of the two applied forces, i.e.,

$$\tau_s = 1/\omega^*. \tag{4.51}$$

For the slow and the fast hairpin, the relaxation time then follows as $\tau_s \simeq 120\,\mathrm{ms}$ and $\tau_s \simeq 50\,\mathrm{ms}$, respectively. Finally, we note that the effective temperature of the driven two-state system is

$$T_{\mathrm{eff}}/T = \frac{1}{a(1 - \tau_e \omega^*/2)} \tag{4.52}$$

under the experimental conditions, as follows by evaluating the general expression Eq. 4.39 with the response χ (Eq. 4.49) and the correlation function C (Eq. 4.50).

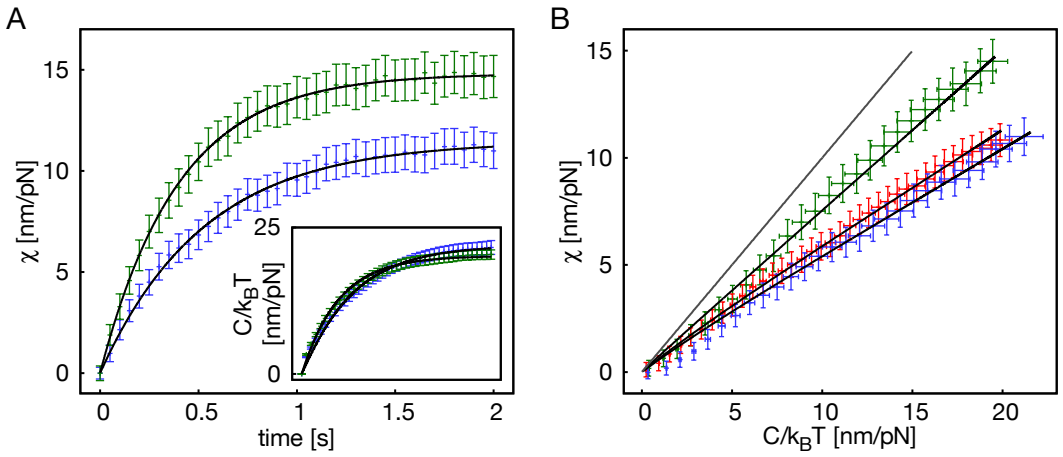

FIGURE 4.4.: Further single-molecule measurements of T_{eff} for short hairpins.
(**A**) For the slow hopper with a larger loop, the response χ and the correlation function C (inset) is shown for $f_c \simeq 12.8\,\text{pN}$, $\Delta f = 1.5\,\text{pN}$ and $\tau_e = 50\,\text{ms}$ (green) and $\tau_e = 200\,\text{ms}$ (blue). The relaxation time is $\tau_s \simeq 400 - 500\,\text{ms}$ for both τ_e. An average over five (four) molecules for χ and six (five) molecules for C for the condition $\tau_e = 50\,\text{ms}$ ($\tau_e = 200\,\text{ms}$) is shown. The theoretical results (black) use $\omega^* \simeq 2.5\,\text{s}^{-1}$, $a \simeq 0.80$, $x_{UF} \simeq 18.0\,\text{nm}$ ($\omega^* \simeq 1.9\,\text{s}^{-1}$, $a \simeq 0.62$, $x_{UF} \simeq 19.1\,\text{nm}$) for $\tau_e = 50\,\text{ms}$ ($\tau_e = 200\,\text{ms}$).
(**B**) The corresponding parametric plots together with the equilibrium FDT (gray). In red, the parametric plot for the slow hopper with a smaller loop with $\tau_e = 50\,\text{ms}$ and $\tau_s \simeq 120\,\text{ms}$ is included from Fig. 4.3D. Figure reprinted from [23].

Further Single-Molecule Measurements of the Effective Temperature

The good match between theory and experiment observed for the short hairpins extends to another series of measurements we have performed with a different molecule type which has the same hairpin sequence as the slow hopper but a larger loop, leading to a slower hopping kinetics. As a result, the system relaxation time of this molecule has increased to $\tau_s \simeq 400 - 500\,\text{ms}$ which has allowed us to vary the force switching time τ_e more widely while still matching the effective temperature condition $\tau_e < \tau_s$. In particular, we have increased the force switching time to $\tau_e = 200\,\text{ms}$ to restore the ratio $\tau_e/\tau_s \simeq 0.4$ that we have observed for the original slow hopper with a smaller loop. The experiment then confirms well the theoretical prediction (see Eq. 4.49 and 4.50) that the parametric plot depends on the force switching time

τ_e only through the ratio τ_e/τ_s, thus highlighting that this ratio is crucial for both the existence and the value of the effective temperature (see Fig. 4.4A and B, single-molecule results are given in Appendix B). For a smaller τ_e/τ_s, the experiment clearly shows that the effective temperature approaches room temperature, as is predicted by the four-state model (see Eq. 4.52). This result can be intuitively understood to reflect how for smaller τ_e/τ_s the hairpin is driven more weakly and is thus closer to equilibrium.

4.4. The Multiple-State Long Hairpin

For systems with multiple states, the natural extension of the Markovian model predicts an accordingly larger number of relaxation times which need not be well-separated so that both χ and C can have a quite complex structure. Moreover, since different time scales in general contribute with different weights to χ and C, the response and the correlation function are in general not connected by a simple time-independent proportionality factor such as the effective temperature. However, if one manages to find driving parameters for which the response has one well-separated relaxation time τ_s, an effective temperature still occurs, provided that the important constraint $\tau_e < \tau_s$ is matched.
As an example of a system with numerous states and multiple timescales, we considered a long 6800 base pairs DNA hairpin. The FDC of this hairpin shows many intermediates separated by random energy barriers that are dynamically populated under stochastic driving (Fig. 4.5A and B). Because (un)folding transitions can cover a much larger distance for the long hairpin, the feedback struggles more to maintain the desired force value (Fig. 4.5A and B). Still, on the relevant time scales τ_e and τ_s, the force is controlled to good approximation.
We find that the experimental response function relaxes on a well-separated time scale τ_s (Fig. 4.5C, single-molecule results are shown in Appendix B), showing that the long hairpin represents a special case of a multiple-state system with clear time scale separation. Such a result can nevertheless be expected to be typical for a system with large, non-degenerate barrier heights such as the long hairpin since the system relaxation times depend exponentially on these heights.

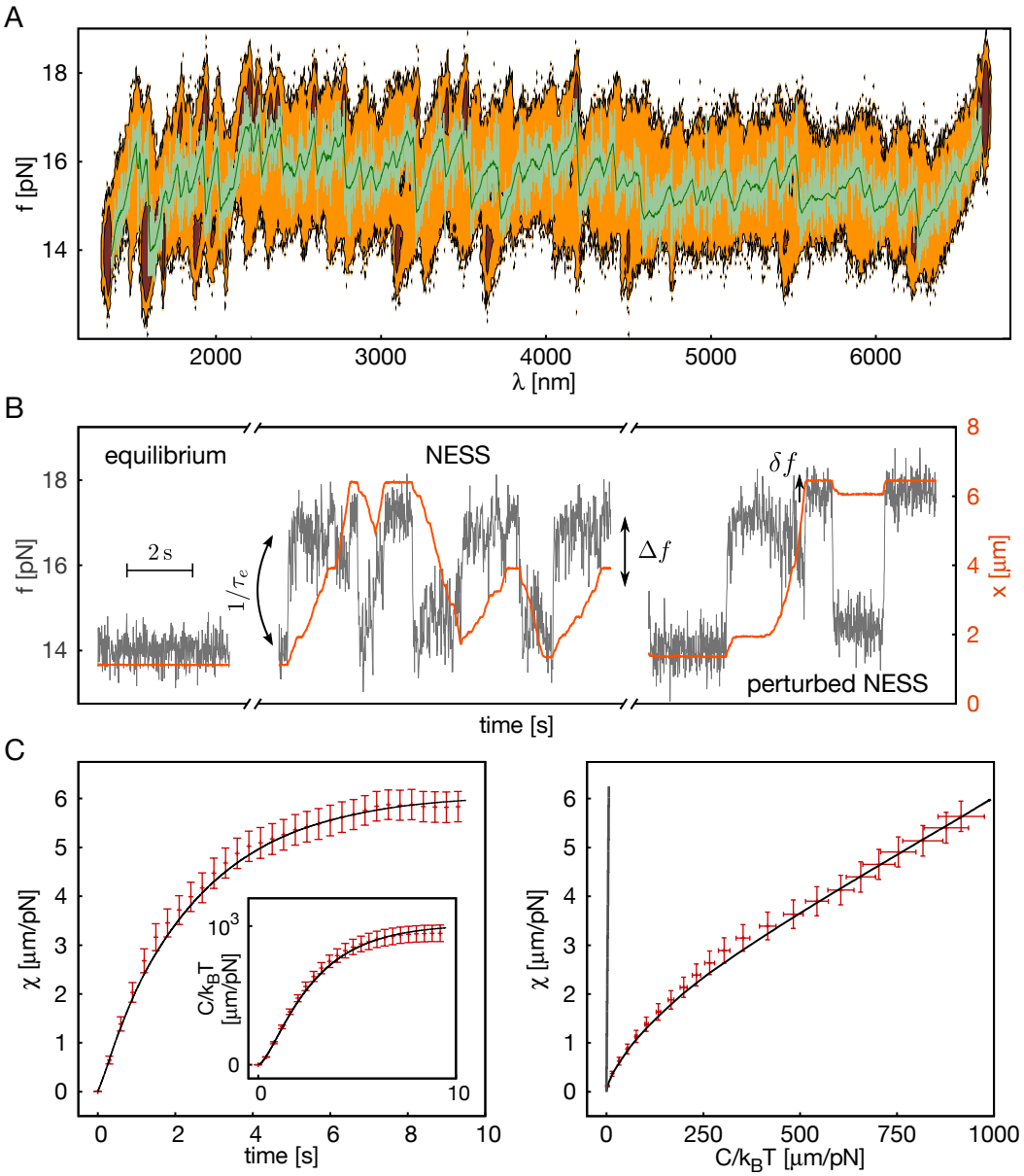
A
f [pN]
λ [nm]
B
equilibrium
NESS
perturbed NESS
2 s
$1/\tau_e$
Δf
δf
f [pN]
x [μm]
time [s]
C
χ [μm/pN]
time [s]
C/k_BT [μm/pN]
χ [μm/pN]
C/k_BT [μm/pN]

FIGURE 4.5: Long hairpin system.
(**A**) Experimental unzipping force-distance curve (data filtered at 4 Hz in dark green and unfiltered data in light green) for the 6.8kbp long hairpin. Large force rips in the force-distance curve reflect the need to overcome large barriers and thus mark stable intermediate states of the hairpin. Using feedback to apply a dichotomous force f changing at rate $1/\tau_e$ between $\pm \equiv f_c \pm \Delta f$, these states are populated most in the course of the dynamics. Accordingly, the experimental contour plot of the logarithmic histogram over a NESS with $f_c = 15.6\,\mathrm{pN}$, $\Delta f = 1.6\,\mathrm{pN}$ and $\tau_e = 1.33\,\mathrm{s}$ takes large values for these states (orange-brown colors). Because of the imperfect feedback, the system does not rigorously evolve along the two forces $\pm$. The force-distance curve has already been shown in Fig. 2.1.
(**B**) Experimental traces of the force f (gray) and the molecular extension x (orange), where δf is the size of the perturbation.
(**C**) Response function $\chi(t) \equiv \langle x(t) - x(0)\rangle/\delta f$ (main plot) and correlation function $C(t) \equiv \langle (x(0) - x(t))x(0)\rangle$ (inset) for these parameters. For both χ and C, we show an average over four molecules. The response and correlation function relax on $\tau_s \simeq 2\,\mathrm{s}$. We compare the experimental data with simulations of the full base-pairwise dynamics (black). On the right hand side, we show the corresponding parametric plots, where the effective temperature $T_{\mathrm{eff}} \simeq 190\,\mathrm{T} = 56620\,\mathrm{K}$ shows the pronounced deviation from the equilibrium FDT prediction (near vertical gray line). Figure reprinted from [23].

Furthermore, we observe that in analogy to the short hairpins, the relaxation time τ_s of the long hairpin decreases with growing force amplitude Δf, since a stronger stochastic forcing drives the hairpin more quickly across its barriers during the steady-state dynamics. The condition $\tau_e < \tau_s$ for an effective temperature can therefore be matched experimentally by adjusting Δf. The parametric plot then shows a linear regime (right hand side of Fig. 4.5C), thus demonstrating that there is an effective temperature for the multiple-state long hairpin. This effective temperature is quite large which fits in nicely with the observation that the stochastic driving significantly enhances the fluctuations of the molecular extension as it helps the hairpin to explore its full molecular free energy landscape whereas in equilibrium it would remain stuck in one region for exceedingly long times (Fig. 4.5B).
We support these experimental results with simulations describing the stochastically driven (un)folding dynamics at the level of single base pairs. In the following, we first define these simulations and subsequently show that they reproduce both the experimental response and correlation function remarkably well if one implements the random forcing with the experimental parameters (black lines in Fig. 4.5C).

Simulation of the Base-pairwise Dynamics

We model the dynamics of the long hairpin as a Markov process within its free energy profile $G(f, n)$ where the applied force f changes stochastically over time according to the external protocol Eq. 4.9. This free energy profile has already been shown in Sec. 2.2 to take the expression

$$G(f, n) = G_{\mathrm{DNA}}(n) + G_s(f, n), \tag{4.53}$$

with the free energies $G_{\mathrm{DNA}}(n)$ of the hairpin and

$$G_s(f, n) = -\int_0^f x(f', n)\,\mathrm{d}f'. \tag{4.54}$$

of the single-stranded DNA released during the unfolding process.
Within this free energy profile, the Markov process is modeled with rates $\omega_{nn\pm1}$ to break or close one base pair if n base pairs are open. For these rates, we use an asymmetric splitting of Kramers type rates [61,98] as suggested in Ref. [99]

$$\omega_{nn+1} = k_0 \exp\left(-\frac{G_{\mathrm{DNA}}(n+1) - G_{\mathrm{DNA}}(n)}{k_B T}\right) \tag{4.55}$$

$$\omega_{nn-1} = k_0 \exp\left(-\frac{G_s(f, n-1) - G_s(f, n)}{k_B T}\right) \tag{4.56}$$

with the attempt frequency k_0.
We stress that we have additionally taken into account that experimentally the force baseline can change along the x axis. Specifically, we observe that the actual applied force can vary by a few 0.1 pN across a distance of several μm. In the simulations, these conditions are included by adding an offset to the force decreasing linearly from zero at the most zipped state of the dynamics ($n \simeq 2000$) to some minimal value f_{off} at the fully unfolded state ($n \simeq 6800$). Finally, we point out that we have neglected the contribution from the loop which brings in an entropic barrier that has to be overcome to close the first base pair when the hairpin is fully unfolded. In the experiments, single base pair transitions cannot be resolved, though. Instead, we observe transitions in which many base pairs break or open at once [45]. On this more coarse-grained level, the entropic barrier caused by the loop is smoothed out so that it can be expected to have little effect on the dynamics.

Comparing Theory and Experiment

We reach good agreement with the experiment by using the parameters $f_{\text{off}} = -0.35\,\text{pN}$ and $k_0 = 6.1{\cdot}10^5\,\text{Hz}$ for the simulations (see Fig. 4.5C). Furthermore, all theoretical parameters but f_c, i.e., τ_e, Δf and δf, take the respective experimental value. The theoretical mean force f_c had to be adjusted somewhat since we observe that the experimental mean unzipping force of the FDC can change by up to 1 pN between molecules of the same type. In order to similarly populate the states of the hairpin for different molecules, the experimental mean force was always set $0.1 - 0.2\,\text{pN}$ larger than the respective mean unzipping force. Theoretically, the mean unzipping force is around 16.9 pN, and therefore, the experimental conditions have been reproduced using $f_c = 17.0\,\text{pN}$ in the simulations.

4.5. Conclusion

In summary, we have identified an effective temperature for three different systems with varying complexity, from the bead in the optical trap to various two-state short DNA hairpins and a multiple-state long hairpin. All of these systems have been driven into a NESS by applying random forces. We have found a necessary condition for observing an effective temperature in these systems: the force switching time τ_e of the external driving has to be smaller than the relaxation time τ_s of the system, i.e., $\tau_e < \tau_s$. We have observed

a wide range of effective temperatures, from $T_{\text{eff}} \simeq 2\,\text{T}$ for the short hairpin, $T_{\text{eff}} \simeq 7\,\text{T}$ for the bead in the optical trap to $T_{\text{eff}} \simeq 190\,\text{T}$ for the long hairpin. All these values are well above the room temperature T, thus demonstrating that we have identified effective temperatures for systems driven deep into the nonequilibrium regime.

The experimental results have been found to be in good agreement with predictions from theoretical models. These models include an overdamped Langevin dynamics for the bead in the optical trap, a four-state Markov system for the short hairpins and a base-pairwise simulation of the long hairpin dynamics which takes into account both its elastic properties and its base pair sequence. The analysis of these theoretical models has not only given support to our experimental results. It has also suggested the identification of the crossover time τ_c into the effective temperature regime and highlighted the physical meaning of the relaxation time τ_s. Furthermore, the four-state model for the short hairpins has proven that the effective temperature is independent of the choice of the observable, a statement whose generalization should be in the focus of future work.

On a side note, we stress that an earlier suggestion [21] to measure the effective temperature by coupling an isolated harmonic oscillator to the system is shown in Appendix C to exactly reproduce the effective temperature for $\tau_e \ll \tau_s$ and to yield quite good agreement with T_{eff} outside this limit. However, how to implement this suggestion experimentally is far from obvious, since the oscillator cannot be isolated. Rather, the oscillator feels additional noise by the heat bath compromising a direct measurement of the effective temperature.

5. Force Feedback in DNA Unfolding

5.1. Introduction

In the previous chapter, it was demonstrated that an effective temperature can be identified for single DNA hairpins driven into a NESS by random external forces. Since the position of the optical trap is the control parameter in the DNA unfolding setup rather than the force (see Sec. 2.1), a feedback mechanism is needed to gain control of the force and apply the stochastic driving according to the external protocol.
This force feedback is implemented in our setup by repeatedly first measuring the force f that works against the captured bead and then moving the optical trap depending on the measurement outcome to get closer to some target force f_T [33, 100, 101]. More precisely, given some measured force f as input, the feedback adjusts the trap position λ by means of

$$\Delta\lambda = G\frac{f_T - f}{k_{\text{eff}}}, \tag{5.1}$$

where G is the dimensionless feedback gain and where k_{eff} is an effective rigidity with fixed value. Hence, if the force is smaller than the desired value f_T, the feedback increases the distance λ to pull stronger ($\Delta\lambda > 0$). Conversely, if f is larger than f_T, $\Delta\lambda < 0$ to decrease the tension. At this point, we stress that our notation differs somewhat from the one used in the previous chapter since we now distinguish between the actual force f of the system and the external target force f_T. In the previous chapter where the feedback is assumed to be perfect, these two forces coincide and are both referred to as f.

The force feedback has two parameters: The first one is the feedback gain G which according to Eq. 5.1 determines by how much the trap is moved given some measurement of the force f. The other free parameter is the time scale τ_F on which the feedback operates, i.e., on which it measures the force and adjusts the trap. The feedback responds to changes of the force with some delay due to this finite operation time. Additionally, once it responds,

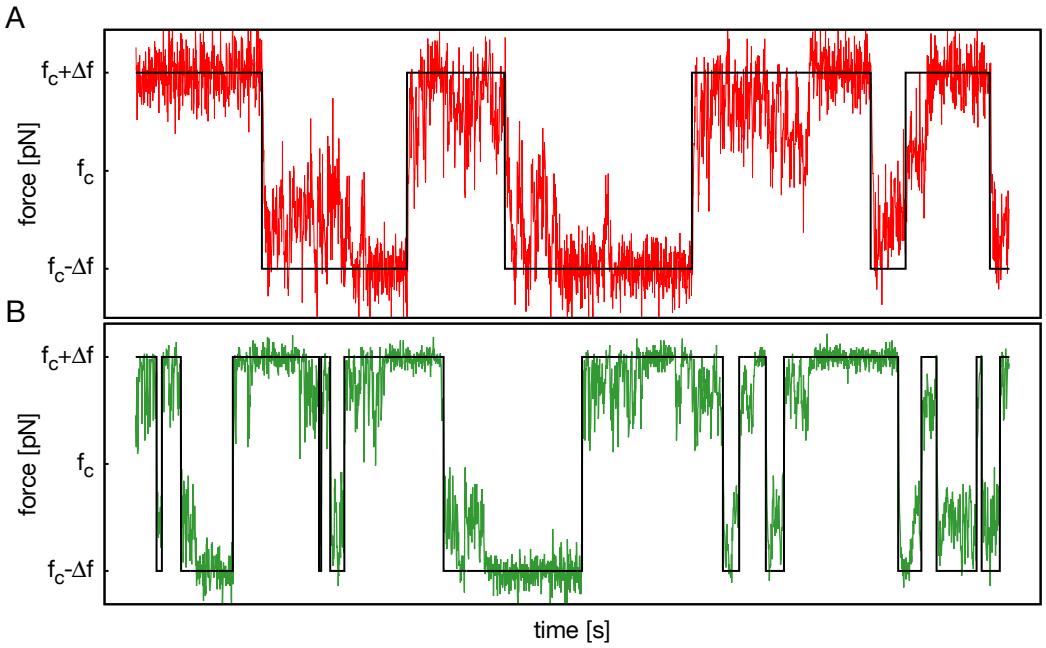

FIGURE 5.1.: Feedback control of the force.
(**A**) Experimental trajectory segment of the target force f_T (black) and the measured force f (red) in the NESS, where $f_c = 15.6\,\mathrm{pN}$, $\Delta f = 1.6\,\mathrm{pN}$, $\tau_e = 1.33\,\mathrm{s}$, $\tau_F = 1\,\mathrm{ms}$ and $G = 0.5$. This panel has already been shown in the introductory Fig. 1.2.
(**B**) Corresponding simulated trajectory segments with the same parameters as in (**A**) but using a different mean force $f_c = 17.0\,\mathrm{pN}$. However, both the theoretical and the experimental f_c are by the same amount larger than the respective mean unzipping force which in the experiments can change from molecule to molecule. Hence, the physical situation is the same in theory and experiment even though the value of f_c is different. We note that here and in the following, the force offset f_{off} introduced in Sec. 4.4 has been set to zero.

it does not know the instantaneous force but rather a time-averaged one. The trap adjustment which the feedback calculates therefore in general does not match the actual state of the system and so even after the feedback operation f might not coincide with the target value f_T. Still, Fig. 5.1 shows that, with an appropriate choice of the parameters G and τ_F, the force is in general close to f_T along the stochastically driven NESS. In this NESS, the target force is

randomly changed at rate $1/\tau_e$ between the two values

$$f_T^{\pm} \equiv f_c \pm \Delta f \tag{5.2}$$

(see Eq. 4.9). Furthermore, Fig. 5.1 not only contains experimental data but also introduces the simulations our following discussion of the force feedback in DNA unfolding will also be based on. These simulations use an extension of the base-pairwise model introduced in Sec. 4.5 for the long hairpin by explicitly implementing the experimental feedback mechanism according to Eq. 5.1. With these simulations, the dependence of the feedback-controlled dynamics on the parameters G and τ_F will be investigated.
However, before considering the DNA unfolding system, we discuss the force feedback for the overdamped harmonic oscillator since this much simplified system already illustrates some of the features of the feedback (Sec. 5.2). For this system, we introduce a description of the feedback-driven dynamics in terms of the time-resolved mean reaction of the force f to a change of the target value f_T. We subsequently move on to the DNA unfolding system for which we combine the temporal resolution of the dynamics offered by this mean force trajectory with a spatial one by additionally considering the force population in a given state of the hairpin (Sec. 5.3).

5.2. Toy Model: Harmonic Oscillator

The force feedback for the overdamped particle in a harmonic oscillator is modeled in analogy to the one for the DNA unfolding experiments. Hence, in each time interval τ_F, the feedback first measures the mean force f that acts on the particle and then adjusts the position λ of the oscillator according to Eq. 5.1 in order to bring f closer to the desired target force f_T. Assuming that this adjustment has led to the oscillator position λ_0 at time $t = 0$, this position is kept until $t = \tau_F$ when the feedback has measured a new force and responds to it with another trap adjustment. In the meantime, the dynamics of the trapped particle is governed by the Langevin equation

$$\dot{x} = -\mu k(x - \lambda_0) + \zeta(t) \qquad (0 < t < \tau_F), \tag{5.3}$$

where μ is the mobility and $\zeta(t)$ the thermal white noise with mean $\langle\zeta\rangle = 0$ and variance $\langle\zeta(t')\zeta(t'')\rangle = 2\mu k_B T\delta(t' - t'')$, with k_BT the thermal energy (see Sec. 3.1). During this dynamics, the feedback first measures the mean force

$$f_1 \equiv \frac{1}{\tau_F}\int_0^{\tau_F} f(t)\,\mathrm{d}t \tag{5.4}$$

and then, at time $t = \tau_F$, changes the trap position to the new value

$$\lambda_1 = G\frac{f_T - f_1}{k_{\text{eff}}} + \lambda_0 \tag{5.5}$$

(see Eq. 5.1). In the following time interval, the particle follows the same Langevin dynamics as before (see Eq. 5.3) but the position of the trap is updated to λ_1. The feedback then starts a new iteration in which it first measures the force and afterwards adjusts the potential. The dynamics of the feedback-controlled overdamped particle can therefore be solved in an iterative manner provided that the external protocol for the target force is known. Here, we use the same protocol as for the DNA unfolding setup and hence randomly switch the target force between two values at rate $1/\tau_e$ (see Eq. 5.2).
In the following, the resulting feedback-driven dynamics will be described by looking at how the force changes on average over time once the target force takes a new value. Here, we consider an average of the force over both the thermal noise and the ensemble of all time segments in the course of the dynamics where the target force takes the same value f_T. Hence, we can evaluate this quantity either for the larger ($f_T = f_T^+$) or the smaller target force ($f_T = f_T^-$) of the stochastic driving. In general, the corresponding mean trajectories can be different; however, for the harmonic oscillator they differ by just a sign due to the symmetry of the oscillator with respect to its minimum.
As illustration, we show in Fig. 5.2A the mean force change after a transition of the target force from f_T^- to f_T^+ for a given set of the feedback parameters G and τ_F. We observe that the mean force approaches the new target force periodically; hence, for these feedback parameters, the mean force gets closer to the target force with every adjustment that the feedback performs. The oscillations of the mean force which we see in Fig. 5.2A will later turn out to be characteristic for large feedback gains. In fact, if G is further increased and surpasses some threshold $G_{\max}$, these oscillations get stronger over time and thus destabilize the system. In contrast, if G is small, the feedback applies only soft changes to the trap position, leading to a monotonous increase of the force towards its target value. However, as a common feature of this monotonous increase of the force for small G and its oscillations for large G (but smaller than $G_{\max}$), their enveloping function is an exponential decay on a time scale τ_r towards a limit value $\overline{f}_\infty$ (see Fig 5.2A).
For these two quantities, analytical expressions can be derived by solving the dynamics in the iterative manner outlined above but including an average over both the thermal noise and different time segments of the particle trajectory with the same target force. While the former average can be implemented simply, the latter is more formal. Hence, in the following, we will first calculate

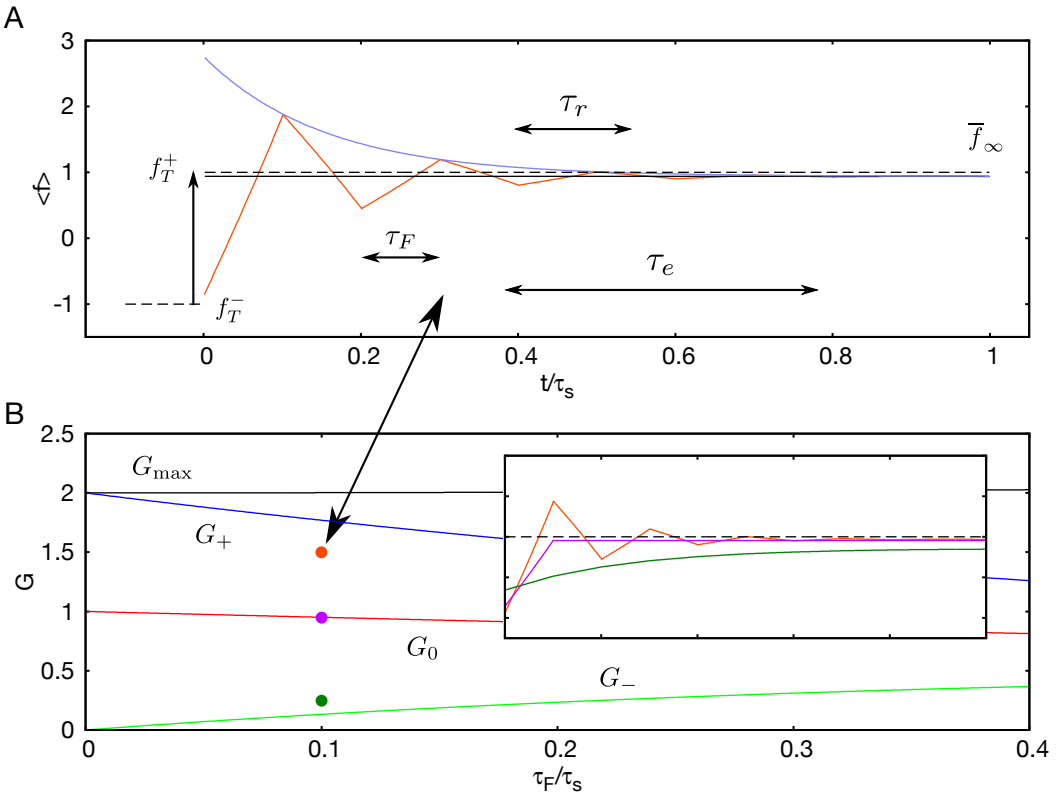

FIGURE 5.2.: Force feedback for the harmonic oscillator.
(**A**) Mean force trajectory (orange) for $G = 1.5$, $\tau_F/\tau_s = 0.1$ and $\tau_e/\tau_s = 0.4$. In blue, we show the exponential decay of the mean force at times $t = n\tau_F$ $(n = 0, 1, 2, \dots)$ towards the limit value $\overline{f}_\infty$ (black line). The external protocol Eq. 5.2 for the target force runs with $f_c = 0$ and $\Delta f/\sqrt{kk_BT} = 1$ (dashed line).
(**B**) The threshold value $G_{\max}$ (Eq. 5.14), the optimal value G_0 (Eq. 5.19) and the two boundaries G_+ (Eq. 5.21) and G_- (Eq. 5.20) for the feedback gain using $\tau_e/\tau_s = 0.4$. The colored dots mark the respective conditions of the mean force trajectories shown in the inset. For this inset, the axis are the same as in (**A**). For $G = G_0$, the mean force reaches its limit value $\overline{f}_\infty$ after one feedback iteration. Increasing G further leads to oscillations (shown data the same as in (**A**)) whereas for $G < G_0$, the mean force converges monotonically towards $\overline{f}_\infty$.

τ_r and f_∞ for one time segment, i.e., one change of the target force, and then state how these expressions change when one performs the ensemble average over different trajectory segments with the same target force.
The thermal average can be implemented directly by just dropping the thermal noise. Indeed, for the harmonic oscillator, since the noise enters the force linearly, it is canceled by the thermal average with $\langle\zeta\rangle = 0$. Then, starting the feedback at time $t = 0$ with the particle and the trap at the mean positions $\langle x(0)\rangle$ and $\langle\lambda_0\rangle$, respectively, the mean particle trajectory for all times $0 < t < \tau_F$ follows as

$$\langle x(t)\rangle = (\langle x(0)\rangle - \langle\lambda_0\rangle)\exp(-t/\tau_s) + \langle\lambda_0\rangle \tag{5.6}$$

by solving Eq. 5.3. With the mean initial force $\langle f(0)\rangle \equiv -k(\langle x(0)\rangle - \langle\lambda_0\rangle)$, the corresponding mean force trajectory in this time interval is

$$\langle f(t)\rangle = -k(\langle x(t)\rangle - \langle\lambda_0\rangle) = \langle f(0)\rangle\exp(-t/\tau_s), \tag{5.7}$$

from which get the average force

$$\langle f_1\rangle \equiv \frac{1}{\tau_F}\int_0^{\tau_F}\langle f(t)\rangle\,\mathrm{d}t. \tag{5.8}$$

The feedback uses this force to calculate with

$$\langle\lambda_1\rangle \equiv G\frac{f_T - \langle f_1\rangle}{k} + \langle\lambda_0\rangle \tag{5.9}$$

the mean new position of the trap after the first feedback interval (see Eq. 5.5). The mean force at $t = \tau_F$ then follows as

$$\langle f(\tau_F)\rangle = Gf_T + \langle f(0)\rangle\alpha, \tag{5.10}$$

where

$$\alpha \equiv \exp(-\tau_F/\tau_s)(1 + G\tau_s/\tau_F) - G\tau_s/\tau_F. \tag{5.11}$$

This calculation can be iterated to get the mean force at time $t = n\tau_F$

$$\langle f(n\tau_F)\rangle = \langle f(0)\rangle\alpha^n + Gf_T\sum_{m=0}^{n-1}\alpha^m. \tag{5.12}$$

In the limit $n \to \infty$, this force converges to some finite value only if

$$|\alpha| \overset{!}{<} 1. \tag{5.13}$$

For a given feedback time τ_F, this condition is matched for feedback gains

$$G \overset{!}{<} G_{\max} \equiv \frac{\tau_F}{\tau_s} \frac{1 + \exp(-\tau_F/\tau_s)}{1 - \exp(-\tau_F/\tau_s)} \tag{5.14}$$

(see Figure 5.2B). For these feedback gains, the mean force at time $t = n\tau_F$ is

$$\begin{aligned} \langle f(n\tau_F) \rangle &= \langle f(0) \rangle \alpha^n + \frac{G f_T}{1 - \alpha}(1 - \alpha^n) \\ &= f_\infty + \alpha^n (\langle f(0) \rangle - f_\infty). \end{aligned} \tag{5.15}$$

with the limit force

$$f_\infty \equiv \lim_{n \to \infty} \langle f(n\tau_F) \rangle = \frac{G f_T}{1 - \alpha}. \tag{5.16}$$

The force relaxation towards the limit value f_∞ is thus governed by an exponential law in n. The time scale of this relaxation τ_r can be determined by

$$\frac{\langle f((n+2)\tau_F) \rangle - f_\infty}{\langle f(n\tau_F) \rangle - f_\infty} = \alpha^2 \equiv \exp(-2\tau_F/\tau_r) \tag{5.17}$$

(see Figure 5.2A) or, equivalently,

$$\exp(-\tau_F/\tau_r) = |\alpha|. \tag{5.18}$$

If one uses the optimal feedback gain

$$G_0 = \frac{\tau_F}{\tau_s} \frac{\exp(-\tau_F/\tau_s)}{1 - \exp(-\tau_F/\tau_s)} \tag{5.19}$$

(see Figure 5.2B), the relaxation time τ_r apparently becomes zero. However, one should note that the mean force does not jump instantaneously to its limit value if $\tau_r \to 0$. Instead, in this case, the force is equal to the limit value f_∞ at time $t = \tau_F$, hence right after the first feedback adjustment. However, it can be very different from f_∞ for times $t < \tau_F$. To ensure that the convergence of the mean force is faster than the switching time τ_e, we thus not only need $\tau_r < \tau_e$ but also $\tau_F < \tau_e$. While the latter condition puts a constraint on the feedback time scale, the former leads to the lower bound

$$G \overset{!}{>} G_- \equiv \frac{\tau_F}{\tau_s} \frac{\exp(-\tau_F/\tau_s) - \exp(-\tau_F/\tau_e)}{1 - \exp(-\tau_F/\tau_s)} \tag{5.20}$$

and the upper bound

$$G \overset{!}{<} G_+ \equiv \frac{\tau_F}{\tau_s} \frac{\exp(-\tau_F/\tau_s) + \exp(-\tau_F/\tau_e)}{1 - \exp(-\tau_F/\tau_s)} \tag{5.21}$$

for the feedback gain. These bounds refine the previous constraint $G < G_{\max}$ (see Figure 5.2B).
In summary, we note that the feedback works well for the harmonic oscillator if the conditions $\tau_F < \tau_e$ and $G_- < G < G_+$ are both matched. In particular, we observe that there is an optimal value G_0 for which the relaxation time of the force towards the target value is minimal. These statements, although derived for just one realization of the change of the target force, are still true if one additionally performs an average over the many of these changes that take place in the course of the dynamics. In fact, this average leaves the relaxation time τ_r unaffected and just replaces the limit force f_∞ from Eq. 5.16 by the mean value

$$\overline{f}_\infty \equiv \frac{1}{\tau_F}\int_0^{\tau_F} f_\infty \exp(-t/\tau_s)\,\mathrm{d}t = \frac{G f_T}{\tau_F/\tau_s + G}. \tag{5.22}$$

This expression emphasizes that for realistic feedbacks with finite operation time scales τ_F, the mean force never converges to the target value f_T. Instead, the limit mean force is always below f_T since the system inevitably tends to relax towards its equilibrium state where the mean force is zero.

5.3. Feedback in DNA Unfolding

5.3.1. Mean Force Trajectory

We start the discussion of the force feedback in the DNA unfolding setup by considering the mean force trajectory we have introduced for the harmonic oscillator. We first demonstrate that theory and experiment agree reasonably well for this quantity and then use further simulations to explore the parameter space spanned by the feedback gain G and the feedback time scale τ_F.
Figure 5.3 shows that the feedback performs somewhat better in theory than it does in the experiments, as the theoretical mean force relaxes faster towards the target value. This better performance of the theoretical feedback is most likely caused by the simplifications we have used to model the system dynamics since these tend to make the feedback more (or too) efficient. However, we observe that the theoretical and the experimental mean force trajectory agree qualitatively so far as they both show the same structure of local maxima and minima. This complex structure reflects the many relaxation times of the DNA unfolding: While for small times, the feedback just needs to work against the relaxation of single base pairs, big unfolding transitions that significantly decrease the applied force kick in at larger times. Since the feedback needs

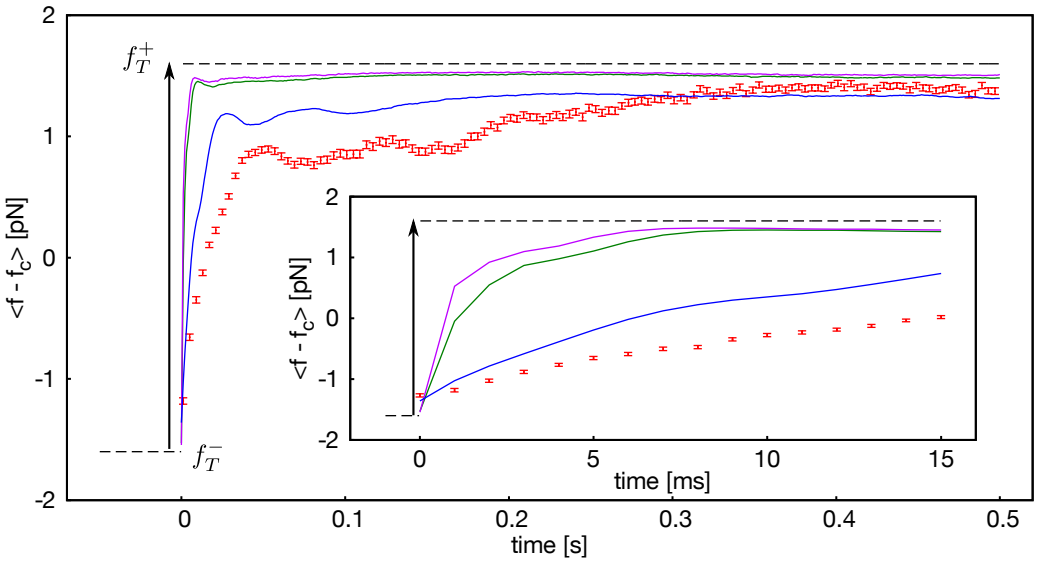

FIGURE 5.3.: Mean force trajectory in DNA unfolding. Experimental (red) and theoretical (other colors) mean force trajectories after a change of the target force for $f_c = 17.0\,\mathrm{pN}$ (experiment: $f_c = 15.6\,\mathrm{pN}$), $\Delta f = 1.6\,\mathrm{pN}$, $\tau_e = 1.33\,\mathrm{s}$, $\tau_F = 1\,\mathrm{ms}$ and $G = 0.5$ (red, blue), $G = 2$ (green) or $G = 2.7$ (violet). Note that in contrast to the harmonic oscillator, the mean force trajectory from the upper to the lower target force can in principle look different. Under the experimental conditions, this difference is small, though. The inset shows the short time regime of the mean force trajectories. Figure in part reprinted from [23].

some time to respond to these transitions, the mean force first drops and then rises again. The different maxima and minima of the mean force trajectories illustrate that this process takes place on several time scales.
Hence, due to the various relaxation time scales of the DNA unfolding system, its mean force trajectory is quite different from the one of the harmonic oscillator. However, one could expect that these two systems behave similarly in the short time regime where the relaxation time scale of single base pairs dominates. Fig. 5.3 demonstrates that for moderate $G < 2.7$, the periodic adjustments of the feedback lead to a monotonous increase of the mean force trajectory in the short-time regime that is indeed similar to that observed for the harmonic oscillator for small G. The analogy breaks down, however, for larger G where the mean force does not show decaying oscillations as predicted by the harmonic oscillator but rather becomes unstable.
This abrupt instability can be attributed to the fact that the stiffness of the

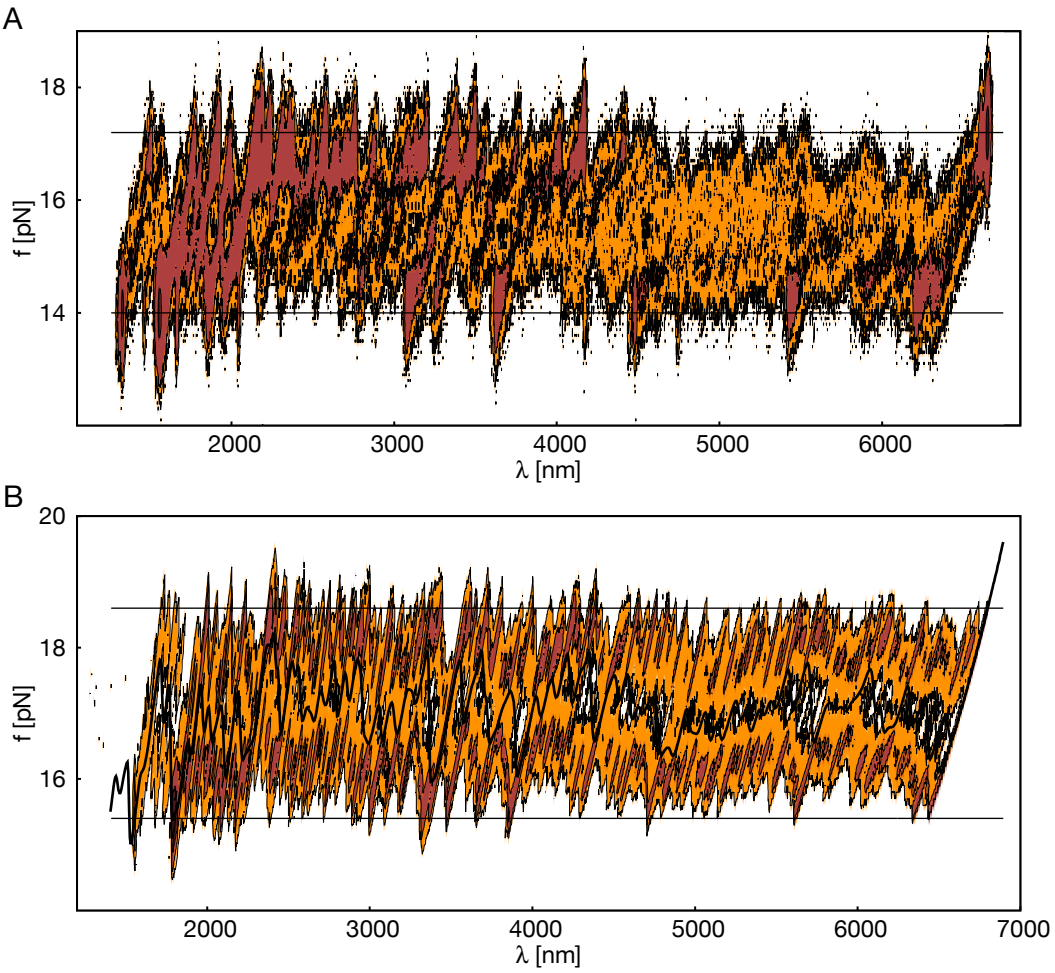

FIGURE 5.4.: Population in the (λ, f) plane in theory and experiment.
(**A**) Logarithm of the experimental histogram for $f_c = 15.6\,\mathrm{pN}$, $\Delta f = 1.6\,\mathrm{pN}$, $\tau_e = 1.33\,\mathrm{s}$, $\tau_F = 1\,\mathrm{ms}$ and $G = 0.5$. Here and in the following, the horizontal black lines represent the two target forces.
(**B**) Logarithm of the theoretical histogram for the same parameters as in (**A**) except for the mean force, where we use $f_c = 17.0\,\mathrm{pN}$. In black, we show the theoretical force-distance curve (FDC) obtained if one unfolds the hairpin infinitely slowly. For both panels, a darker color represents a larger population. Figure in part reprinted from [23].

hairpin, unlike the stiffness of the harmonic oscillator, is not fixed but depends on which state the hairpin is in. If the hairpin is in a state where less base pairs are open, it is stiffer and the same trap displacement leads to a larger change of the force. Since the size of the trap displacement is controlled by the feedback gain G, the same G that is rather soft when the hairpin is wide open can destabilize the system if the hairpin is almost closed. However, since the mean force trajectory does not know about the state of the hairpin, it will display an average over all states. Therefore, the mean force trajectory can suggest a moderate average reaction of the system to the feedback when the feedback gain G is almost large enough to fully destabilize the hairpin if it is closed. Increasing G any further then leads to the abrupt instability of the system noted above.
Compared to the feedback gain G, the influence of the feedback operation time scale τ_F on the system dynamics is more straightforward: A feedback with smaller τ_F can control the system better, leading to a mean force that converges faster towards the target value (data not shown).
Summarizing, we note that the mean force trajectories suggest that the feedback works best for the minimal value of τ_F available and for some optimal value of the feedback gain G. This optimal value is estimated to be around $G \simeq 2.5$ for the hairpin we considered. For larger and smaller G, the feedback either excites the system too strongly or adjusts the trap position too softly, leading to a slower relaxation towards the target force.

5.3.2. Population of States in the (λ, f) plane

The mean force trajectory has provided us with a temporal resolution of the feedback-controlled dynamics of the DNA unfolding system. However, it hides the dependence of the dynamics on the instantaneous state of the hairpin. This spatial dependence can be resolved by considering the population of forces in the state of the hairpin where n base pairs are open. As every number of open base pairs can be translated into a trap position λ intuitively (see Eq. 2.1), this population is equivalent to a histogram in the (λ, f) plane.

For this histogram, Fig. 5.4 demonstrates good agreement between the theoretical prediction and the experimental result. Although the experiments naturally offer a lower resolution than the simulations, they coincide well with the theoretical results in both the high and the low population regime. The rough structure of the histogram can be understood when comparing it with the FDC one would measure if the DNA were unfolded infinitely slowly (by increasing λ). Since the system can then equilibrate for every fixed value of λ,

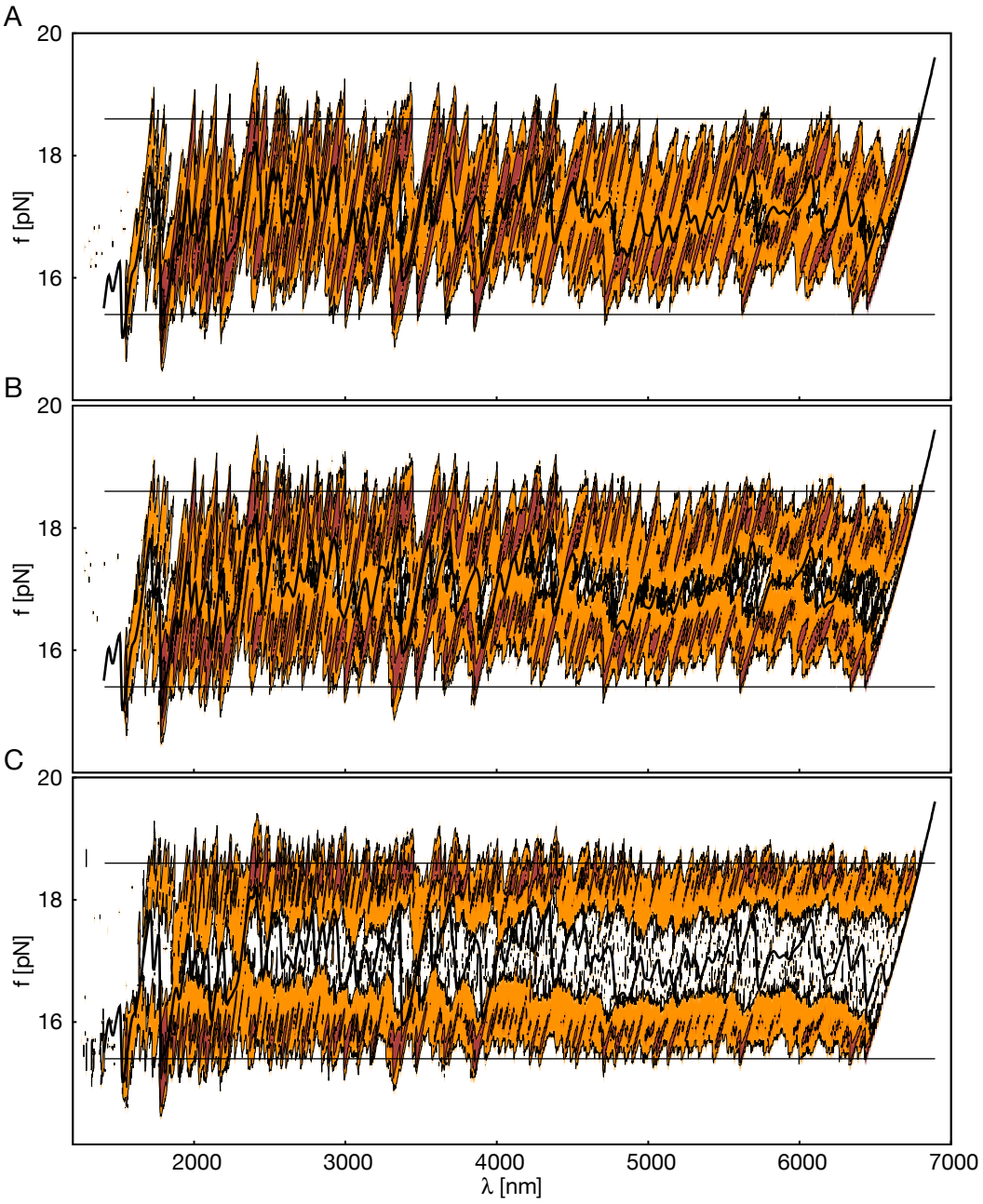

FIGURE 5.5.: Logarithm of the theoretical histogram for $f_c = 17.0\,\mathrm{pN}$, $\Delta f = 1.6\,\mathrm{pN}$, $\tau_e = 1.33\,\mathrm{s}$, $\tau_F = 1\,\mathrm{ms}$ and $G = 0.2$ (**A**), $G = 0.5$ (**B**) and $G = 2.0$ (**C**). As in Fig. 5.4, we show the FDC and the target forces in black.

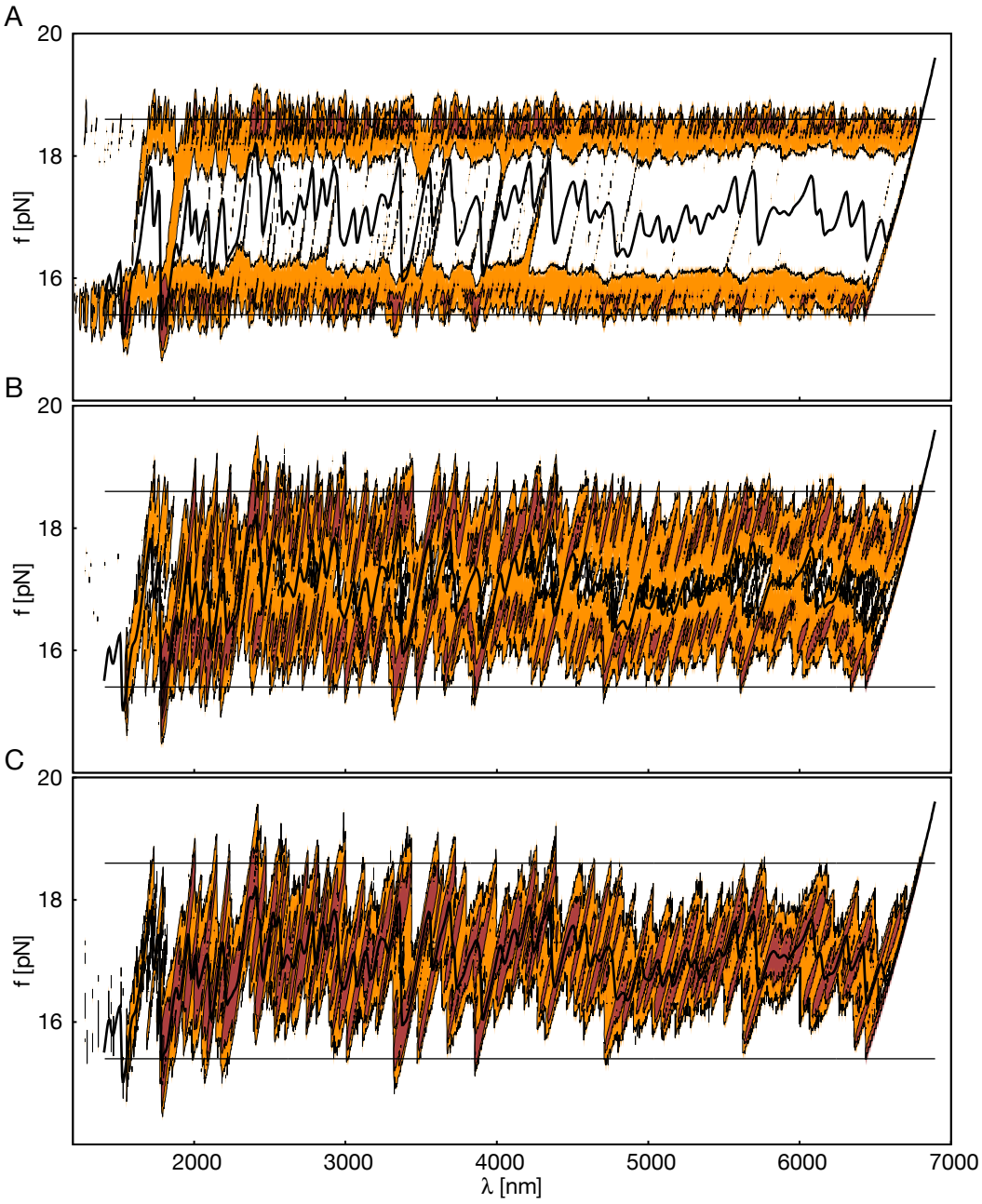

FIGURE 5.6.: Logarithm of the theoretical histogram for $f_c = 17.0\,\mathrm{pN}$, $\Delta f = 1.6\,\mathrm{pN}$, $\tau_e = 1.33\,\mathrm{s}$, $G = 0.5$ and $\tau_F = 0.1\,\mathrm{ms}$ (**A**), $\tau_F = 1\,\mathrm{ms}$ (**B**) and $\tau_F = 10\,\mathrm{ms}$ (**C**). The FDC and the target forces are shown in black.

this curve marks the mean equilibrium force in the (λ, f) plane.
In the stochastic driving considered here, the feedback attempts to apply a force which is either larger or smaller than this equilibrium force. However, since the feedback operates on a finite time scale τ_F, it has to permanently fight against the relaxation of the force towards its equilibrium value taking place within each τ_F. The more it manages to do so, the more both larger and smaller forces are applied in each state of the hairpin. Hence, to some degree the system explores the elastic response of each of these states more than in equilibrium. In the (λ, f) plane, these elastic responses are represented as force ramps so that the histogram in this plane looks as if these force ramps were extrapolated to larger and smaller values.
The good match of theory and experiment shown above allows us to use simulations to explore the feedback-driven dynamics outside the experimental conditions, too. These simulations demonstrate that there is an optimal value for the feedback gain G for which the force is closest to its target value along the dynamics. This value can be estimated to be around $G \simeq 2$ (see Fig. 5.5C) which is in good agreement with the previous value derived on the basis of the mean force trajectories (see Sec. 5.3.1). For both larger and smaller values of G, the feedback is less efficient: While strong adjustments of the trap destabilize the system for large G, the feedback is too soft for small ones. The simulations show that for these G, the hairpin hardly leaves the equilibrium states marked by the equilibrium FDC (see Fig. 5.5A). Indeed, for small G, the feedback becomes weak in the sense that it does not change the position of the optical trap significantly. Then, the system can relax into equilibrium for every value of λ so that only forces in the proximity of the FDC are populated. Keeping G fixed and varying τ_F instead reproduces the intuitive result already stated for the mean force trajectories: The more often the feedback can adjust the optical trap in a given time, i.e. the smaller τ_F, the better the target forces can be generated. Specifically, Fig. 5.6A and 5.6B show that while the experimental $\tau_F = 1\,\mathrm{ms}$ already leads to a good control of the force, the quality of the feedback is dramatically increased when decreasing its operation time scale down to $\tau_F = 0.1\,\mathrm{ms}$. For large τ_F on the other hand, the system is hardly driven out of equilibrium (see Fig. 5.6C).

5.4. Conclusion

We have considered a force feedback mechanism for an overdamped particle in a harmonic oscillator and for a long multiple-state DNA hairpin with a rough unfolding free energy profile. For the harmonic oscillator system, the analysis

of the mean force trajectory after a change of the target force f_T has confirmed the naive expectation that the feedback reacts more quickly to a change of f_T if its operation time τ_F is smaller. Furthermore, the mean force trajectory suggests that there is an optimal value of the feedback gain G for which the feedback is most capable of following the external protocol for the force: For feedback gains smaller than this optimal value, the mean force responds to a change of f_T more slowly since the feedback adjusts the trap more softly. For larger feedback gains on the other hand, the trap adjustments are too strong, leading to oscillations of the force which, if G is increased beyond a threshold value, even grow over time, thus destabilizing the system.
In comparison, the mean force trajectory of the long DNA hairpin has a significantly more complex structure, reflecting the broad spectrum of system time scales which range from the short times of the breaking and closing of single base pairs to the large times for which big (un)folding transitions take place. Yet, in the short-time regime, the mean force trajectory has been found to be similar for the long hairpin and the overdamped particle in the harmonic trap. In particular, we have confirmed the result that the feedback works better for smaller τ_F and that there is an optimal value of G for which the force is most quickly adjusted to a change of the target value.
A complementary perspective on the feedback-controlled dynamics has been reached by considering the force histogram in a given state of the DNA hairpin. This histogram illustrates that the feedback drives the system away from equilibrium as it attempts to realize the external random forcing. In particular, the system is pushed further into the nonequilibrium regime for larger G but becomes unstable if G is increased beyond some threshold value. Furthermore, we have observed that the agreement of the force with its target value is maximal for some optimal feedback gain whose value has turned out to agree well with the prediction by the mean force trajectory. Finally, considering the force population for fixed G but varying feedback operation times τ_F has confirmed the earlier result that the feedback controls the force better if τ_F is smaller.
In conclusion, the consideration of the mean force trajectory and the force population has clearly resolved the role of the gain G and the operation time τ_F in the feedback-controlled dynamics of DNA hairpins. Along this dynamics, thermodynamic quantities such as the heat which is dissipated by the hairpin into the medium should be evaluated in future work. The analysis of such quantities can be expected to further illustrate how the thermodynamics of the DNA hairpin depends on the feedback parameters.

A. Verification of the Equilibrium FDT and Short Hairpin Traces

This appendix demonstrates that if the experiments with the trapped bead (see Sec. 4.2) and the short hairpins (see Sec. 4.3) are performed in equilibrium conditions, the usual FDT Eq. 4.1 is fulfilled with room temperature T. Additionally, we illustrate that the fast and the slow short hairpin have different hopping rates when driven by a similar force protocol.

Equilibrium FDT for the Bead in the Optical Trap

We have measured the response and correlation function in equilibrium to verify that the FDT is satisfied. Fig. A.1A shows that the FDT is fulfilled well except for a small deviation in the short time regime which, however, covers the first milliseconds of χ and C only. Note that the overall good agreement with the equilibrium FDT also confirms the linearity of the response of the driven harmonic oscillator even for large perturbation sizes such as the value $\delta f \simeq 1.7\,\mathrm{pN}$ used here.

Equilibrium FDT for the Short Hairpin

In analogy to the harmonic oscillator system, we verify the FDT by measuring the response and correlation function in equilibrium which, for the DNA hairpin systems, corresponds to the application of a constant force (Fig. 4.3C and 4.5B). The results for χ and C of such an equilibrium experiment shown in Fig. A.1B demonstrate that the FDT is fulfilled well across the whole time axis for our experimental setup.

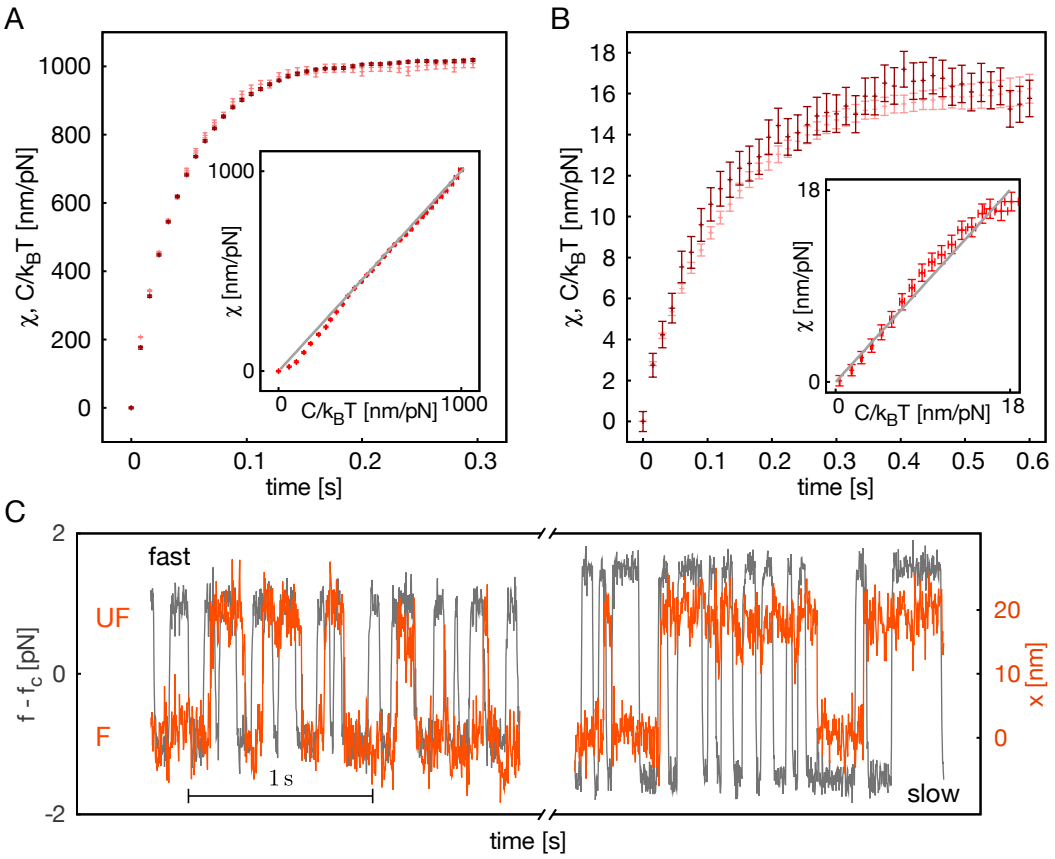

FIGURE A.1: Verification of the equilibrium FDT and short hairpin traces. (**A**) Verification of the equilibrium FDT for the bead in the optical trap. The main frame shows the response function $\chi(t) \equiv \langle x(t) - x(0) \rangle / \delta f$ (dark red) and the correlation function $C(t) \equiv \langle (x(0) - x(t)) x(0) \rangle$ (light red), while the inset depicts the corresponding parametric plot (red) together with the equilibrium FDT (gray). The size of the perturbation is $\delta f \simeq 1.7\,\mathrm{pN}$ ($\delta\lambda \simeq 1700\,\mathrm{nm}$).
(**B**) Verification of the equilibrium FDT for the slow hopping hairpin. The main frame shows the response function $\chi(t) \equiv \langle x(t) - x(0) \rangle / \delta f$ (dark red) and the correlation function $C(t) \equiv \langle (x(0) - x(t)) x(0) \rangle$ (light red). The corresponding parametric plot (red) is depicted in the inset together with the equilibrium FDT (gray). Experiments use the protocol parameters $f_c = 14.7\,\mathrm{pN}$ and $\delta f = 0.5\,\mathrm{pN}$.
(**C**) Experimental trace of the force (gray) and the molecular extension (orange) for the fast (left) and the slow (right) hopping hairpin in the stochastically driven NESS. The NESS is generated with $\tau_e = 50\,\mathrm{ms}$ and $\Delta f = 1\,\mathrm{pN}$, $f_c = 15\,\mathrm{pN}$ ($\Delta f = 1.5\,\mathrm{pN}$, $f_c = 14\,\mathrm{pN}$) for the fast (slow) hairpin. Figure reprinted from [23].

Short Hairpin Traces

The traces shown in Fig. A.1C exemplify that the two short hairpins we have considered in Sec. 4.3 show hopping at different rates between the unfolded and folded state although they are driven by similar force protocols. In fact, the slow hopper is even driven a bit stronger, with larger Δf, but still its hopping rate is noticeably below the one for the fast hairpin. The difference in the hopping rates reflects that the barrier which the hairpin needs to overcome to fold or unfold is significantly larger for the slow hopper, as a result of its different sequence of base pairs.

B. Single-Molecule Results

In this appendix, we present single-molecule results for the response χ and the correlation function C. With these results, we have calculated the average χ and C which we show in Sec. 4.3 for the short hairpins and Sec. 4.4 for the long hairpin.

Short Hairpins

Fig. B.1A and Fig. B.1B show that the variability among different experiments is noticeably larger for the short hairpin experiments (first presented in Fig. 4.3D) than it is for the harmonic oscillator (see Fig. 4.1B). In particular, the response functions for the slow short hairpin show large variability. Still, the finding that there is a linear regime in the parametric plot, i.e., an effective temperature, for $\tau_e < \tau_s$ but none for $\tau_e > \tau_s$ is recovered at the level of single molecules. For the third molecule type with a larger loop (see Fig. 4.4A and B), we also observe a variability of the response and correlation function stronger than the one found for the harmonic oscillator (Fig. B.1C and B.1D). We find, however, mostly similar effective temperatures on the single-molecule level. Still, we point out that some of the single-molecule parametric plots for the third hairpin type tend to be a bit noisy since on some occasions, the hairpin broke before we could collect long traces for both the response and the correlation function. However, for all molecules, at least either a long NESS or a long perturbed NESS trace could be measured, so that reliable single-molecule estimates of the response and the correlation function are available, as is demonstrated by the left hand sides of Fig. B.1C and B.1D.

Long Hairpin

For the long hairpin discussed in Sec. 4.4, the variability among different molecules is small, especially considering the complexity of the hairpin (Fig. B.1E). In particular, all single molecules clearly show a linear regime in their parametric plot, thus demonstrating the existence of an effective temperature at the level of single experiments as well. Moreover, even the value of this effective temperature is similar for different molecules.

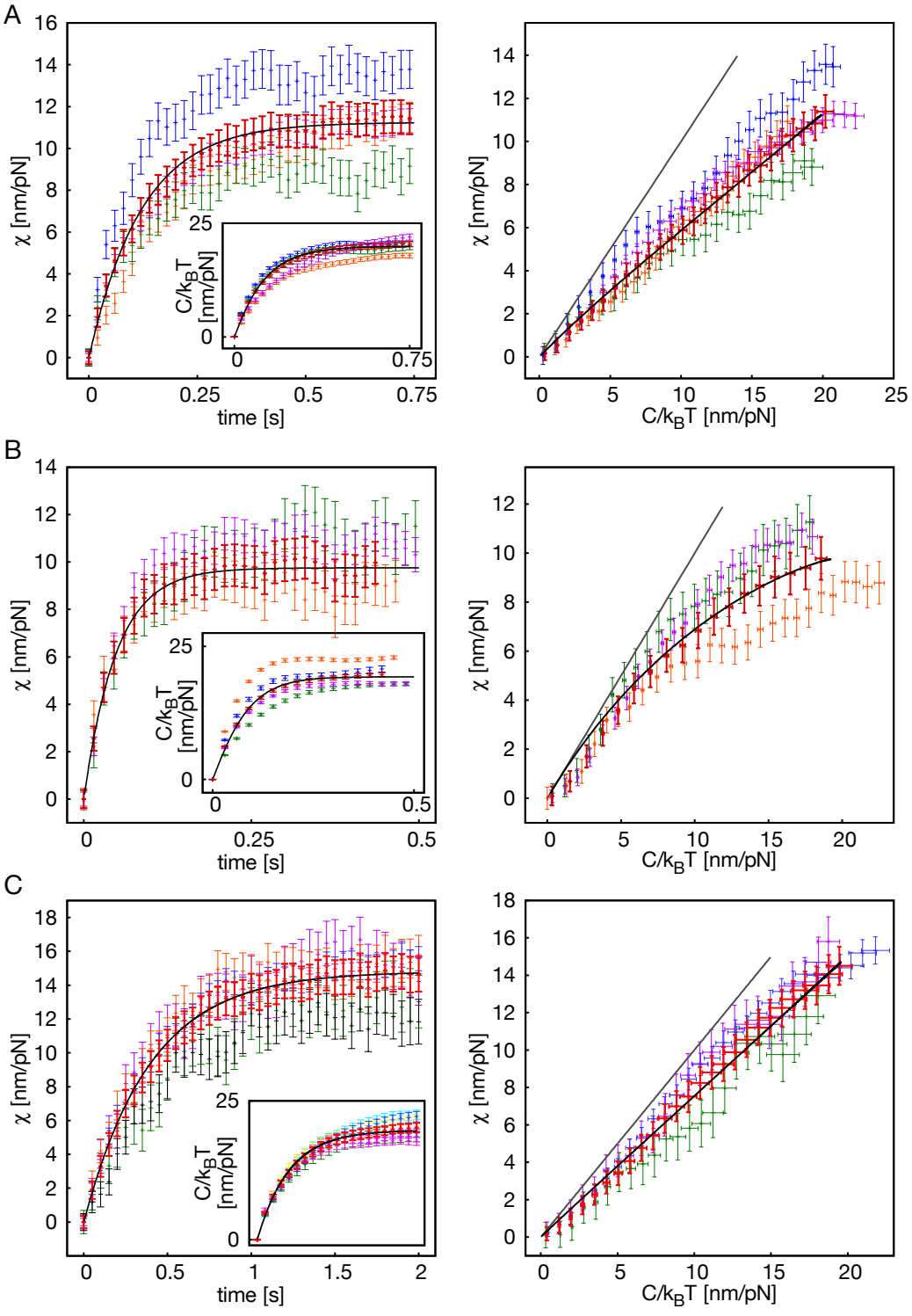
A
B
C
χ [nm/pN]
time [s]
C/k_BT [nm/pN]

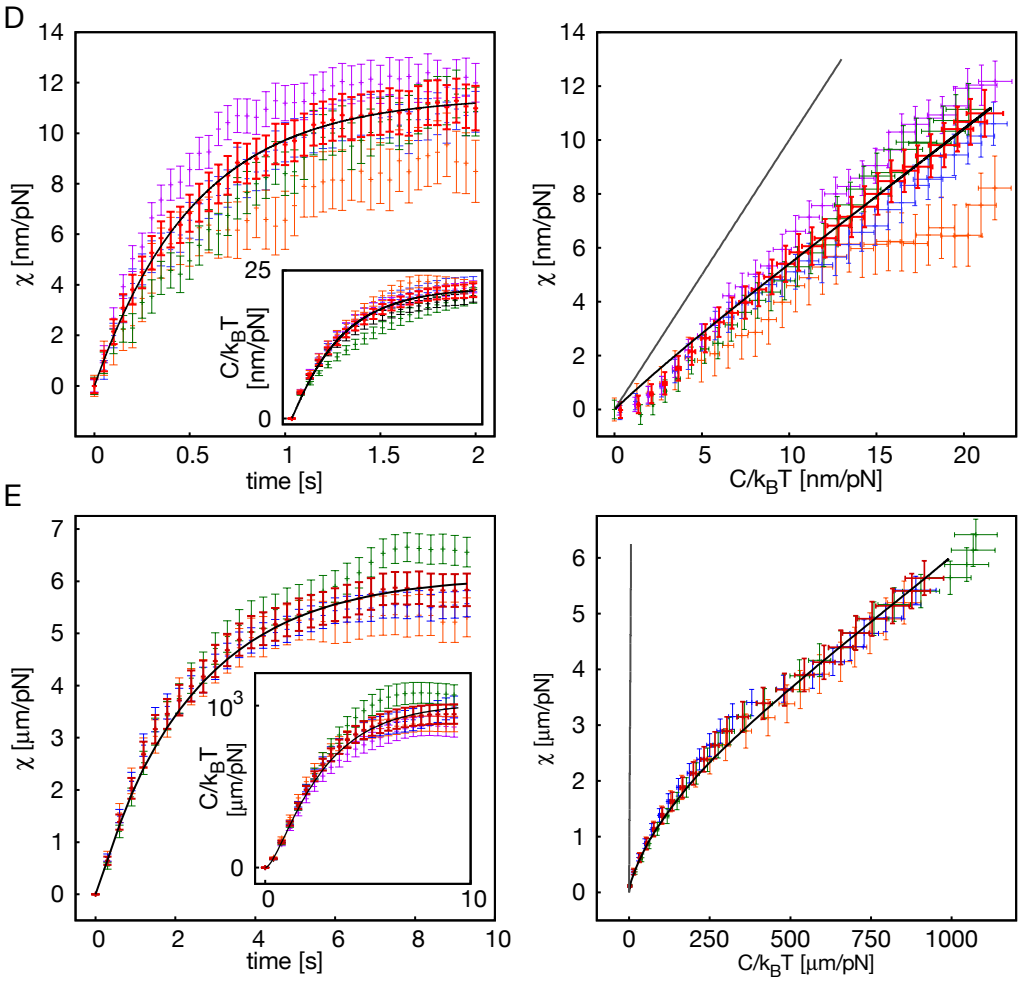

FIGURE B.1: Single-molecule results (various colors) and averages (red) for the response χ and the correlation function C (left) and the corresponding parametric plots (right) at the experimental conditions listed in below table. Figure reprinted from [23].

panel	molecule	τ_e [ms]	Δf [pN]	#mol for χ	#mol for C
(**A**)	slow	50	1.5	5	10
(**B**)	fast	100	1.0	4	5
(**C**)	larger loop	50	1.5	5	6
(**D**)	larger loop	200	1.5	4	5
(**E**)	long	1.33 s	1.6	4	4

C. Coupling an Oscillator to the System

Here, we follow a suggestion by Cugliandolo et al. [21] to measure the effective temperature of a system by coupling a harmonic oscillator to it. Assuming that this coupling is weak and linear and exploiting the equipartition theorem, Cugliandolo et al. [21] found that an oscillator with resonance frequency ω measures the temperature

$$\tilde{T}_{\text{eff}}(\omega) \equiv \frac{\omega \tilde{C}'(\omega)}{k_B \tilde{R}(\omega)}. \tag{C.1}$$

Here, we have introduced the Fourier transforms

$$\tilde{R}(\omega) \equiv \text{Im}\left(\int_0^\infty R(t) \exp(i\omega t)\, \mathrm{d}t\right) \tag{C.2}$$

and

$$\tilde{C}'(\omega) \equiv \text{Re}\left(\int_0^\infty C'(t) \exp(i\omega t)\, \mathrm{d}t\right) \tag{C.3}$$

of the response

$$R(t) \equiv \frac{\delta \langle x \rangle(t)}{\delta f(0)} \tag{C.4}$$

of the system to a delta-like perturbation f at time $t = 0$ and of the correlation function

$$C'(t) \equiv \langle (x(t) - \langle x \rangle)(x(0) - \langle x \rangle) \rangle. \tag{C.5}$$

In the following, we will compare this temperature $\tilde{T}_{\text{eff}}(\omega)$ with the effective temperature T_{eff} which the quasi-FDT predicts for large enough times. In the frequency domain, large times roughly correspond to small frequencies. Therefore, we expect that $\tilde{T}_{\text{eff}}(\omega)$ and T_{eff} coincide for small ω. Since according to the FDT, the system equilibrates at room temperature T in the short time regime, we moreover expect to obtain T for large enough ω.

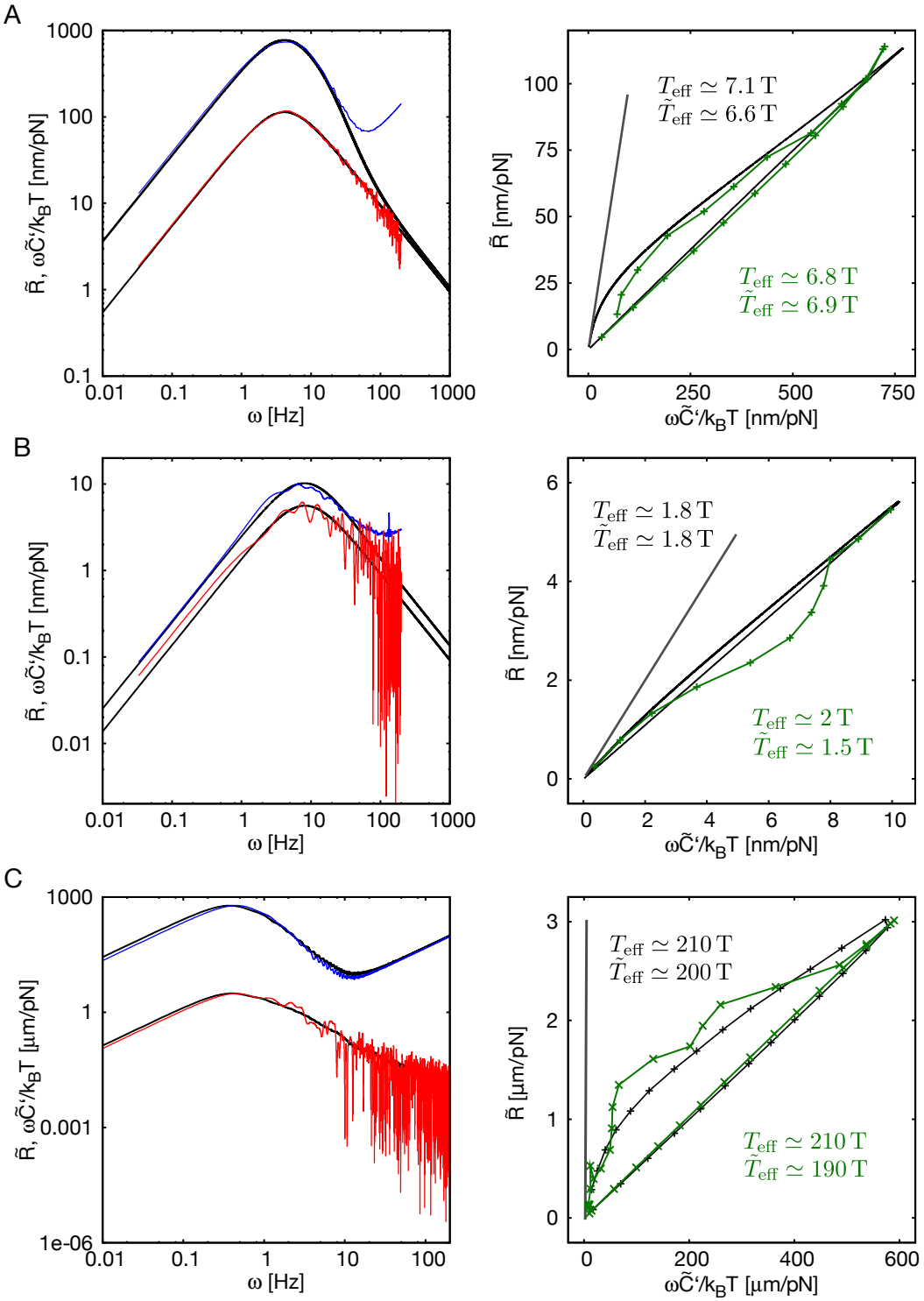
A
B
C
ω [Hz]
R̃, ωC̃'/k_BT [nm/pN]
R̃, ωC̃'/k_BT [µm/pN]
R̃ [nm/pN]
R̃ [µm/pN]
ωC̃'/k_BT [nm/pN]
ωC̃'/k_BT [µm/pN]
T_eff ≃ 7.1 T
T̃_eff ≃ 6.6 T
T_eff ≃ 6.8 T
T̃_eff ≃ 6.9 T
T_eff ≃ 1.8 T
T̃_eff ≃ 1.8 T
T_eff ≃ 2 T
T̃_eff ≃ 1.5 T
T_eff ≃ 210 T
T̃_eff ≃ 200 T
T_eff ≃ 210 T
T̃_eff ≃ 190 T

FIGURE C.1: Coupling an oscillator to the system.
For each, the harmonic oscillator (**A**), the slow short hairpin (**B**) and the long hairpin (**C**), we present the experimental $\tilde{R}(\omega)$ (red) and $\omega\tilde{C}'(\omega)/k_BT$ (blue) on the left hand side and the experimental parametric plot $\tilde{R}(\omega\tilde{C}'/k_BT)$ (green) on the right hand side. The respective theoretical prediction is displayed in black. As a comparison, the equilibrium FDT prediction is shown in the parametric plots (gray). For each system, we give the theoretical (black) and experimental (green) value of the effective temperature T_{eff} and the temperature $\tilde{T}_{\text{eff}} \equiv \tilde{T}_{\text{eff}}(\omega \ll 1/\tau_e, 1/\tau_s)$ which an oscillator with small resonance frequency would measure. The experimental parameters are $\Delta f \simeq 0.7\,\text{pN}$, $\delta f \simeq 1.0\,\text{pN}$ and $\tau_e = 100\,\text{ms}$ for the harmonic oscillator, $\Delta f = 1.5\,\text{pN}$, $\delta f = 0.5\,\text{pN}$ and $\tau_e = 50\,\text{ms}$ for the slow short hairpin and $\Delta f = 1.6\,\text{pN}$, $\delta f = 0.5\,\text{pN}$ and $\tau_e = 1.33\,\text{s}$ for the long hairpin. Note that for the short hairpin, the large frequency regime of the parametric plot has been cut off since it shows strong fluctuations. We also point out that we have added zeros to the ends of the experimental and simulated time signals $R(t)$ and $C'(t)$ before calculating their Fourier transforms in order to make the low frequency regime better visible. This zero-padding is possible here since both $R(t)$ and $C'(t)$ decay almost entirely within the observed time span. Figure reprinted from [23].

We present plots of both $\tilde{R}(\omega)$ and $\omega\tilde{C}'(\omega)$ at the experimental conditions for all of our systems (Fig. C.1). These plots show that at small frequencies, $\tilde{T}_{\text{eff}}(\omega)$, i.e., the ratio of $\omega\tilde{C}'(\omega)$ and $k_B\tilde{R}(\omega)$, is almost constant. Equivalently, we observe that the parametric plots $\tilde{R}(\omega\tilde{C}'(\omega))$ show a linear regime at small frequencies in analogy to the linear regime which the corresponding parametric plot $\chi(C)$ shows at large times. This analogy breaks down, however, for force switching times τ_e larger than τ_s: In the frequency domain, a linear regime then still exists (data not shown) whereas in the time domain it does not.
As a consequence, there is strictly speaking no crossover frequency (indicating the breakdown of the concept of an effective temperature) which is analogous to the crossover time scale τ_c since τ_c diverges as τ_e approaches τ_s. Finding the frequency ranges corresponding to the time ranges $t \ll \tau_c$ and $t \gg \tau_c$ for which the quasi-FDT predicts room temperature and the effective temperature, respectively, is thus not straightforward. Roughly, however, we can use the limits $\omega \gg 1/\tau_e, 1/\tau_s$ and $\omega \ll 1/\tau_e, 1/\tau_s$. In the following, these limits will be discussed for the harmonic oscillator and the different hairpin systems using both experimental results and theoretical predictions for the respective model system.

Harmonic Oscillator

For the driven harmonic oscillator, the Langevin model introduced in Eq. 4.10 gives

$$\tilde{R}(\omega) = \frac{\mu\omega\tau_s^2}{1+(\omega\tau_s)^2} \tag{C.6}$$

and

$$\omega\tilde{C}'(\omega)/k_BT = \tilde{R}(\omega) + \frac{2\alpha\tau_s/\tau_e}{(2\tau_s/\tau_e)^2-1}\left(\tilde{R}(\omega) - \frac{\mu\omega(\tau_e/2)^2}{1+(\omega\tau_e/2)^2}\right). \tag{C.7}$$

The temperature measured by an oscillator with resonance frequency ω follows as

$$\tilde{T}_{\text{eff}}(\omega)/T = \frac{\omega\tilde{C}'(\omega)/k_BT}{\tilde{R}(\omega)} = 1 + \frac{2\alpha\tau_s/\tau_e}{(2\tau_s/\tau_e)^2-1}\left(1 - \left(\frac{\tau_e}{2\tau_s}\right)^2 \frac{1+(\omega\tau_s)^2}{1+(\omega\tau_e/2)^2}\right). \tag{C.8}$$

In the limits $\omega \gg 1/\tau_e, 1/\tau_s$ and $\omega \ll 1/\tau_e, 1/\tau_s$, we find

$$\tilde{T}_{\text{eff}}(\omega \gg 1/\tau_e, 1/\tau_s)/T \approx 1 \tag{C.9}$$

and

$$\tilde{T}_{\text{eff}}(\omega \ll 1/\tau_e, 1/\tau_s)/T \approx 1 + \frac{2\alpha\tau_s/\tau_e}{(2\tau_s/\tau_e)^2 - 1}\left(1 - \left(\frac{\tau_e}{2\tau_s}\right)^2\right) = 1 + \frac{\alpha\tau_e}{2\tau_s}, \quad \text{(C.10)}$$

respectively. Hence, while at large frequencies the oscillator measures room temperature as expected, the temperature at small frequencies is different from the expression derived in Eq. 4.18

$$T_{\text{eff}}/T \approx 1 + \frac{2\alpha\tau_s/\tau_e}{(2\tau_s/\tau_e)^2 - 1}. \quad \text{(C.11)}$$

In fact, these two temperatures are strictly the same only if $\tau_e \ll \tau_s$. However, their deviation is still small for larger force switching times $\tau_e < \tau_s$ outside this limit. This statement is illustrated by Fig. C.1A which demonstrates that for both, theory and experiment, the difference between $\tilde{T}_{\text{eff}}(\omega \ll 1/\tau_e, 1/\tau_s)$ and T_{eff} is just around six percent even for a force switching time $\tau_e \simeq \tau_s/2$.
On a side note we point out that the discrepancy between the experimental and the theoretical estimate of $\omega\tilde{C}'(\omega)$ visible in Fig. C.1A is caused by the finite experimental time resolution which at large frequencies leads to errors in $\tilde{C}'(\omega)$.

Short Hairpins

As a toy model for the short hairpins, the driven two state system discussed in Sec. 4.3 predicts that

$$\tilde{R}(\omega) = \frac{a x_{UF}^2}{2k_BT(2 + \tau_e/\tau_s)} \frac{\omega\tau_s}{1 + (\omega\tau_s)^2} \quad \text{(C.12)}$$

and

$$\omega\tilde{C}'(\omega)/k_BT = \frac{x_{UF}^2}{4k_BT(4 - (\tau_e/\tau_s)^2)}\left(\frac{4\omega\tau_s}{1 + (\omega\tau_s)^2} - \left(\frac{\tau_e}{\tau_s}\right)^2 \frac{\omega\tau_e/2}{1 + (\omega\tau_e/2)^2}\right) \quad \text{(C.13)}$$

which leads to the oscillator temperature

$$\tilde{T}_{\text{eff}}(\omega)/T = \frac{\omega\tilde{C}'(\omega)/k_BT}{\tilde{R}(\omega)} = \frac{1}{a(1 - \tau_e/2\tau_s)}\left(1 - \left(\frac{\tau_e}{2\tau_s}\right)^3 \frac{1 + (\omega\tau_s)^2}{1 + (\omega\tau_e/2)^2}\right). \quad \text{(C.14)}$$

In analogy to the driven harmonic oscillator, we consider the limits

$$\tilde{T}_{\text{eff}}(\omega \gg 1/\tau_e, 1/\tau_s)/T \approx 1/a \quad \text{(C.15)}$$

and

$$\tilde{T}_{\text{eff}}(\omega \ll 1/\tau_e, 1/\tau_s)/T = T_{\text{eff}} \left(1 - \left(\frac{\tau_e}{2\tau_s}\right)^3\right). \tag{C.16}$$

We note that an oscillator with a large resonance frequency reproduces the short-time limit of the FDT. For small resonance frequencies, the oscillator measures a temperature which is slightly different from the effective temperature. This deviation is, however, even smaller than in the case of the harmonic oscillator. This statement is exemplified by Fig. C.1B which on the theory side shows good agreement between the effective temperature and the oscillator temperature at small resonance frequencies. The agreement is less good for the experimental data which is, however, quite noisy in the frequency domain leading to a rather inaccurate estimate of the oscillator temperature.

Long Hairpin

For the long hairpin, the theoretical predictions are given by simulations rather than by analytical expressions. Since these simulations operate with a finite time resolution like the experiments do, the theoretical estimate for $\omega\tilde{C}'(\omega)$ is affected by errors for large frequencies as is the experimental one. These estimates are good enough, however, to suggest that $\tilde{T}_{\text{eff}}(\omega)$ becomes the room temperature T at large ω (corresponding to the upper branch for small $\omega\tilde{C}'(\omega)$ in Fig. C.1C). For small ω (lower branch for small $\omega\tilde{C}'(\omega)$ in Fig. C.1C), we find little difference between the effective temperature and the oscillator temperature in both theory and experiment.

Bibliography

[1] Bustamante, C., Liphardt, J. & Ritort, F. The nonequilibrium thermodynamics of small systems. Physics Today **58**, 43–48 (2005).

[2] Ritort, F. Nonequilibrium fluctuations in small systems: from physics to biology. Adv. Chem. Phys. **137**, 31–123 (2008).

[3] Jarzynski, C. Equalities and inequalities: Irreversibility and the second law of thermodynamics at the nanoscale. Annu. Rev. Condens. Matter Phys. **2**, 329–351 (2011).

[4] Seifert, U. Stochastic thermodynamics, fluctuation theorems and molecular machines. Rep. Prog. Phys. **75** (2012).

[5] See the collected articles in the special insight volume. Nature Phys. **11**, 104–139 (2015).

[6] Smith, S. B., Finzi, L. & Bustamante, C. Direct mechanical measurements of the elasticity of single DNA molecules by using magnetic beads. Science **258**, 1122–1126 (1992).

[7] Smith, S. B., Cui, Y. J. & Bustamante, C. Overstretching B-DNA: The elastic response of individual double-stranded and single-stranded DNA molecules. Science **271**, 795–799 (1996).

[8] Kellermayer, M. S. Z., Smith, S. B., Granzier, H. L. & Bustamante, C. Folding-unfolding transitions in single titin molecules characterized with laser tweezers. Science **276**, 1112–1116 (1997).

[9] Liphardt, J., Onoa, B., Smith, S. B., Tinoco, I. & Bustamante, C. Reversible unfolding of single RNA molecules by mechanical force. Science **292**, 733–737 (2001).

[10] Rief, M., Gautel, M., Oesterhelt, F., Fernandez, J. M. & Gaub, H. E. Reversible unfolding of individual titin immunoglobulin domains by AFM. Science **276**, 1109–1112 (1997).

[11] Rief, M., Clausen-Schaumann, H. & Gaub, H. E. Sequence-dependent mechanics of single DNA molecules. Nat. Struct. Biol. **6**, 346–349 (1999).

[12] Jarzynski, C. Nonequilibrium equality for free energy differences. Phys. Rev. Lett. **78**, 2690–2693 (1997).

[13] Evans, D. J., Cohen, E. G. D. & Morriss, G. P. Probability of 2nd law violations in shearing steady-states. Phys. Rev. Lett. **71**, 2401–2404 (1993).

[14] Crooks, G. E. Entropy production fluctuation theorem and the nonequilibrium work relation for free energy differences. Phys. Rev. E **60**, 2721–2726 (1999).

[15] Hatano, T. & Sasa, S. Steady-state thermodynamics of Langevin systems. Phys. Rev. Lett. **86**, 3463–3466 (2001).

[16] Seifert, U. Entropy production along a stochastic trajectory and an integral fluctuation theorem. Phys. Rev. Lett. **95**, 040602 (2005).

[17] Liphardt, J., Dumont, S., Smith, S. B., Tinoco, I. & Bustamante, C. Equilibrium information from nonequilibrium measurements in an experimental test of Jarzynski's equality. Science **296**, 1832–1835 (2002).

[18] Gore, J., Ritort, F. & Bustamante, C. Bias and error in estimates of equilibrium free-energy differences from nonequilibrium measurements. Proc. Nat. Acad. Sci. **100**, 12564–12569 (2003).

[19] Collin, D. et al. Verification of the Crooks fluctuation theorem and recovery of RNA folding free energies. Nature **437**, 231–234 (2005).

[20] Mossa, A., de Lorenzo, S., Huguet, J. M. & Ritort, F. Measurement of work in single-molecule pulling experiments. J. Chem. Phys. **130**, 234116 (2009).

[21] Cugliandolo, L. F., Kurchan, J. & Peliti, L. Energy flow, partial equilibration, and effective temperatures in systems with slow dynamics. Phys. Rev. E **55**, 3898–3914 (1997).

[22] Cugliandolo, L. F. The effective temperature. J. Phys. A **44** (2011).

[23] Dieterich, E., Camunas-Soler, J., Ribezzi-Crivellari, M., Seifert, U. & Ritort, F. Single molecule measurement of the effective temperature in nonequilibrium steady states. Nature Phys. to be published.

[24] Sagawa, T. & Ueda, M. Generalized Jarzynski equality under nonequilibrium feedback control. Phys. Rev. Lett. **104**, 090602 (2010).

[25] Toyabe, S., Sagawa, T., Ueda, M., Muneyuki, E. & Sano, M. Experimental demonstration of information-to-energy conversion and validation of the generalized Jarzynski equality. Nature Phys. **6**, 988–992 (2010).

[26] Abreu, D. & Seifert, U. Thermodynamics of genuine nonequilibrium states under feedback control. Phys. Rev. Lett. **108**, 030601 (2012).

[27] Abreu, D. & Seifert, U. Extracting work from a single heat bath through feedback. Europhys. Lett. **94**, 10001 (2011).

[28] Bauer, M., Abreu, D. & Seifert, U. Efficiency of a Brownian information machine. J. Phys. A **45**, 162001 (2012).

[29] Landauer, R. Irreversibility and heat generation in the computing process. IBM J. Res. Develop. **5**, 183–191 (1961).

[30] Berut, A. et al. Experimental verification of Landauer's principle linking information and thermodynamics. Nature **483**, 187 (2012).

[31] Jun, Y., Gavrilov, M. & Bechhoefer, J. High-precision test of Landauer's principle in a feedback trap. Phys. Rev. Lett. **113**, 190601 (2014).

[32] Smith, S. B., Cui, Y. J. & Bustamante, C. Optical-trap force transducer that operates by direct measurement of light momentum. Methods in Enzymology **361**, 134–162 (2003).

[33] Wen, J. D. et al. Force unfolding kinetics of RNA using optical tweezers. I. Effects of experimental variables on measured results. Biophys. Jour. **92**, 2996–3009 (2007).

[34] Mossa, A., Manosas, M., Forns, N., Huguet, J. M. & Ritort, F. Dynamic force spectroscopy of DNA hairpins: I. Force kinetics and free energy landscapes. J. Stat. Mech. (2009).

[35] Manosas, M., Mossa, A., Forns, N., Huguet, J. M. & Ritort, F. Dynamic force spectroscopy of DNA hairpins: II. Irreversibility and dissipation. J. Stat. Mech. P02061 (2009).

[36] Forns, N. et al. Improving signal/noise resolution in single-molecule experiments using molecular constructs with short handles. Biophys. Jour. **100**, 1765–1774 (2011).

[37] Ribezzi-Crivellari, M., Huguet, J. M. & Ritort, F. Counter-propagating dual-trap optical tweezers based on linear momentum conservation. Rev. Sci. Instrum. **84**, 043104 (2013).

[38] Ribezzi-Crivellari, M. & Ritort, F. Free-energy inference from partial work measurements in small systems. Proc. Nat. Acad. Sci. **111**, E3386–E3394 (2014).

[39] Neuman, K. C. & Nagy, A. Single-molecule force spectroscopy: optical tweezers, magnetic tweezers and atomic force microscopy. Nature Methods **5**, 491–505 (2008).

[40] Marko, J. F. & Siggia, E. D. Stretching DNA. Macromolecules **28**, 8759–8770 (1995).

[41] Bosco, A., Camunas-Soler, J. & Ritort, F. Elastic properties and secondary structure formation of single-stranded DNA at monovalent and divalent salt conditions. Nucleic Acids Res. **44**, 2064–2074 (2014).

[42] Alemany, A., Mossa, A., Junier, I. & Ritort, F. Experimental free-energy measurements of kinetic molecular states using fluctuation theorems. Nature Phys. **8**, 688–694 (2012).

[43] Camunas-Soler, J. et al. Electrostatic binding and hydrophobic collapse of peptide-nucleic acid aggregates quantified using force spectroscopy. ACS NANO **7**, 5102–5113 (2013).

[44] Camunas-Soler, J. et al. Single-molecule kinetics and footprinting of DNA bis-intercalation: the paradigmatic case of thiocoraline. Nucleic Acids Res. **43**, 2767–2779 (2015).

[45] Huguet, J. M., Forns, N. & Ritort, F. Statistical properties of metastable intermediates in DNA unzipping. Phys. Rev. Lett. **103** (2009).

[46] Huguet, J. M. et al. Single-molecule derivation of salt dependent base-pair free energies in DNA. Proc. Nat. Acad. Sci. **107**, 15431–15436 (2010).

[47] Brown, R. A brief account of microscopical observations made in the months of June, July and August, 1827, on the particles contained in the pollen of plants; and on the general existence of active molecules in organic and inorganic bodies. Phil. Mag. **4**, 161–173 (1828).

[48] Einstein, A. Über die von der molekularkinetischen Theorie der Wärme geforderte Bewegung von in ruhenden Flüssigkeiten suspendierten Teilchen. Annalen der Physik **17**, 549–560 (1905).

[49] Smoluchowski, M. Zur kinetischen Theorie der Brownschen Molekularbewegung und der Suspensionen. Annalen der Physik **21**, 756–780 (1906).

[50] Langevin, P. Sur la théorie du mouvement brownien. C. R. Acad. des Sci. **146**, 530–533 (1908).

[51] Perrin, J. Mouvement brownien et réalité moléculaire. Ann. de Chim. et de Phys. **18**, 5–114 (1909).

[52] Risken, H. The Fokker-Planck Equation. Methods of Solution and Applications (Springer, 1996), 2nd edn.

[53] Gardiner, C. W. Handbook of Stochastic Methods for Physics, Chemistry and the Natural Sciences (Springer, 2003), 2nd edn.

[54] van Kampen, N. G. Stochastic processes in physics and chemistry (Elsevier, 2004), revised and enlarged edn.

[55] Zwanzig, R. Ensemble method in the theory of irreversibility. J. Chem. Phys. **33**, 1338–1341 (1960).

[56] Zwanzig, R. Nonlinear generalized Langevin equations. J. Stat. Phys. **9**, 215–220 (1973).

[57] Sekimoto, K. Stochastic Energetics (Springer, 2010), 1st edn.

[58] Blum, J., Bruns, S., Rademacher, D., Voss, A. & Willenberg, B. Measurement of the translational and rotational Brownian motion of individual particles in a rarefied gas. Phys. Rev. Lett. **97**, 230601 (2006).

[59] Li, T. C., Kheifets, S., Medellin, D. & Raizen, M. G. Measurement of the instantaneous velocity of a Brownian particle. Science **328**, 1673–1675 (2010).

[60] Huang, R. et al. Direct observation of the full transition from ballistic to diffusive Brownian motion in a liquid. Nature Phys. **7**, 576–580 (2011).

[61] Kramers, H. A. Brownian motion in a field of force and the diffusion model of chemical reactions. Physica **7**, 284–304 (1940).

[62] Moyal, J. E. Stochastic processes and statistical physics. J. R. Stat. Soc. Ser. B Stat. Methodol **11**, 150–210 (1949).

[63] Schnakenberg, J. Network theory of microscopic and macroscopic behaviour of master equation systems. Rev. Mod. Phys. **48**, 571–585 (1976).

[64] Bortz, A. B., Kalos, M. H. & Lebowitz, J. L. New algorithm for Monte-Carlo simulation of Ising spin systems. J. Comp. Phys. **17**, 10–18 (1975).

[65] Gillespie, D. T. Exact stochastic simulation of coupled chemical reactions. J. Phys. Chem. **81**, 2340–2361 (1977).

[66] Kubo, R. Statistical-mechanical theory of irreversible processes. I. General theory and simple applications to magnetic and conduction problems. J. Phys. Soc. Jpn. **12**, 570–586 (1957).

[67] Kubo, R. & Toda, M. Statistical Physics II: Nonequilibrium Statistical Mechanics (Springer, 1998), 2nd edn.

[68] Marconi, U. M. B., Puglisi, A., Rondoni, L. & Vulpiani, A. Fluctuation-dissipation: Response theory in statistical physics. Phys. Rep. **461**, 111–195 (2008).

[69] Bouchaud, J. P., Cugliandolo, L. F., Kurchan, J. & Mezard, M. Out of equilibrium dynamics in spin-glasses and other glassy systems. In Young, A. P. (ed.) Spin Glasses and Random Fields, 161–223 (Singapore: World Scientific, 1998).

[70] Grigera, T. S. & Israeloff, N. E. Observation of fluctuation-dissipation-theorem violations in a structural glass. Phys. Rev. Lett. **83**, 5038–5041 (1999).

[71] Herisson, D. & Ocio, M. Fluctuation-dissipation ratio of a spin glass in the aging regime. Phys. Rev. Lett. **88**, 257202 (2002).

[72] Crisanti, A. & Ritort, F. Violations of the fluctuation-dissipation theorem in glassy systems: basic notions and the numerical evidence. Journal of Physics A (Math. Gen.) **36**, R181–R290 (2003).

[73] Leuzzi, L. A stroll among effective temperatures in aging systems: limits and perspectives. J. Non-Cryst. Solids **355**, 686–693 (2009).

[74] Song, C., Wang, P. & Makse, H. A. Experimental measurement of an effective temperature for jammed granular materials. Proc. Natl. Acad. Sci. U.S.A **102**, 2299–2304 (2005).

[75] Berthier, L., Barrat, J.-L. & Kurchan, J. A two-time-scale, two-temperature scenario for nonlinear rheology. Phys. Rev. E **61**, 5464–5472 (2000).

[76] Loi, D., Mossa, S. & Cugliandolo, L. F. Effective temperature of active matter. Phys. Rev. E **77**, 051111 (2008).

[77] Berthier, L. & Kurchan, J. Non-equilibrium glass transitions in driven and active matter. Nature Phys. **9**, 310–314 (2013).

[78] Coniglio, A., Fierro, A., Herrmann, H. J. & Nicodemi, M. (eds.) Unifying Concepts in Granular Media and Glasses (Elsevier, Amsterdam, 2004), 1st edn.

[79] Marchetti, M. C. et al. Hydrodynamics of soft active matter. Rev. Mod. Phys. **85**, 1143–1189 (2013).

[80] Speck, T. & Seifert, U. Restoring a fluctuation-dissipation theorem in a nonequilibrium steady state. Europhys. Lett. **74**, 391–396 (2006).

[81] Prost, J., Joanny, J.-F. & Parrondo, J. M. R. Generalized fluctuation-dissipation theorem for steady-state systems. Phys. Rev. Lett. **103**, 090601 (2009).

[82] Baiesi, M., Maes, C. & Wynants, B. Fluctuations and response of nonequilibrium states. Phys. Rev. Lett. **103**, 010602 (2009).

[83] Gomez-Solano, J. R., Petrosyan, A., Ciliberto, S., Chetrite, R. & Gawedzki, K. Experimental verification of a modified fluctuation-dissipation relation for a micron-sized particle in a nonequilibrium steady state. Phys. Rev. Lett. **103**, 040601 (2009).

[84] Seifert, U. & Speck, T. Fluctuation-dissipation theorem in nonequilibrium steady states. Europhys. Lett. **89** (2010).

[85] Baiesi, M. & Maes, C. An update on the nonequilibrium linear response. New J. Phys. **15** (2013).

[86] Gomez-Solano, J. R., Bellon, L., Petrosyan, A. & Ciliberto, S. Steady-state fluctuation relations for systems driven by an external random force. Europhys. Lett. **89**, 60003 (2010).

[87] Martinez, I. A., Roldan, R., Parrondo, J. M. R. & Petrov, D. Effective heating to several thousand kelvins of an optically trapped sphere in a liquid. Phys. Rev. E **87**, 032159 (2013).

[88] Berthier, L. & Kurchan, J. Non-equilibrium glass transitions in driven and active matter. Nature Phys. **9**, 310–314 (2013).

[89] Szamel, G. Self-propelled particle in an external potential: Existence of an effective temperature. Phys. Rev. E **90**, 012111 (2014).

[90] Trepagnier, E. H. et al. Experimental test of Hatano and Sasa's nonequilibrium steady-state equality. Proc. Nat. Acad. Sci. **101**, 15038–15041 (2004).

[91] Blickle, V., Speck, T., Helden, L., Seifert, U. & Bechinger, C. Thermodynamics of a colloidal particle in a time-dependent nonharmonic potential. Phys. Rev. Lett. **96**, 070603 (2006).

[92] Franosch, T. et al. Resonances arising from hydrodynamic memory in Brownian motion. Nature **478**, 85–88 (2011).

[93] Blickle, V. & Bechinger, C. Realization of a micrometre-sized stochastic heat engine. Nature Phys. **8**, 143–146 (2012).

[94] Mehl, J., Lander, B., Bechinger, C., Blickle, V. & Seifert, U. Role of hidden slow degrees of freedom in the fluctuation theorem. Phys. Rev. Lett. **108**, 220601 (2012).

[95] Essevaz-Roulet, B., Bockelmann, U. & Heslot, F. Mechanical separation of the complementary strands of DNA. Proc. Natl. Acad. Sci. U.S.A. **94**, 11935–11940 (1997).

[96] Woodside, M. T. et al. Nanomechanical measurements of the sequence-dependent folding landscapes of single nucleic acid hairpins. Proc. Natl. Acad. Sci. U.S.A. **103**, 6190–6195 (2006).

[97] Garriga, A., Pagonabarraga, I. & Ritort, F. Negative fluctuation-dissipation ratios in the backgammon model. Phys. Rev. E **79**, 041122 (2009).

[98] Haenggi, P., Talkner, P. & Borkovec, M. Reaction-rate theory - 50 years after Kramers. Rev. Mod. Phys. **62**, 251–341 (1990).

[99] Cocco, S., Marko, J. & Monasson, R. Slow nucleic acid unzipping kinetics from sequence-defined barriers. Eur. Phys. J. E **10**, 153–161 (2003).

[100] Hayashi, K., de Lorenzo, S., Manosas, M., Huguet, J. M. & Ritort, F. Single-molecule stochastic resonance. Phys. Rev. X **2**, 031012 (2012).

[101] Manosas, M. et al. Force unfolding kinetics of RNA using optical tweezers. II. Modeling experiments. Biophys. Jour. **92**, 3010–3021 (2007).

Acknowledgement

- I want to thank Prof. Udo Seifert and Prof. Felix Ritort for their scientific enthusiasm and curiosity which has allowed me to learn from the day my first project began. Moreover, I would like to thank Prof. Seifert for his caring and inspiring supervision of my doctoral studies.

- It has been a great pleasure to collaborate with Joan Camunas-Soler and Marco Ribezzi-Crivellari who have provided me with extraordinary experimental data and who I have been to lucky to become good friends with. I hope to maintain this friendship.

- Furthermore, I want to thank my master student Jan Reinke for his valuable help on the simulations of the feedback-controlled unfolding dynamics of DNA.

- I am indebted to the members of my institute for the many exciting discussions we have had over the years. I am particularly grateful to Anja Steinhauser for her kind help in all organizational matters.

- Finally, I want to thank my family and my girlfriend Simone for making me happy.

Ehrenwörtliche Erklärung

Ich erkläre, dass ich diese Arbeit selbstständig verfasst und keine anderen als die angegebenen Quellen und Hilfsmittel verwendet habe.

Stuttgart, den 02. Juni 2015 Eckhard Dieterich